

# 博士論文

New precise measurement of the  
hyperfine splitting of positronium

(ポジトロニウムの超微細構造の新しい方法  
による精密測定)

石田 明

---

## Abstract

In this thesis I report a new precision measurement of the ground state hyperfine splitting of positronium  $\Delta_{\text{HFS}}$  which is sensitive to high order corrections of quantum electrodynamics (QED) in a bound state. The theoretical prediction and the averaged experimental value for  $\Delta_{\text{HFS}}$  have a discrepancy of 15 ppm, equivalent to 3.9 standard deviations (s.d.). The new precise measurement, in which the systematic uncertainty from the positronium thermalization effect is reduced, has been performed. The non-thermalization effect was measured to be as large as  $10 \pm 2$  ppm in the used timing window. When this effect is taken into account, obtained new result becomes  $\Delta_{\text{HFS}} = 203.3942 \pm 0.0016$  (stat., 8.0 ppm)  $\pm 0.0013$  (sys., 6.4 ppm) GHz, which favors the QED prediction, on the other hand disfavors the previous experimental average by about 3 s.d.

# Acknowledgements

Firstly, I would like to thank Professor S. Asai (UTokyo) for suggesting this topic and for the guidance in this work.

I also wish to thank Prof. T. Kobayashi and Dr. T. Namba (UTokyo) for very useful suggestions and discussions. Without their supports, this work can not be accomplished.

It is a pleasure to thank Dr. H. Saito (UTokyo) for useful discussions especially about theoretical work on the Zeeman transition.

Sincere gratitude is expressed to Dr. M. Yoshida (KEK) for the great support for construction and operation of microwave system.

Sincere thanks are due to Dr. A. Yamamoto and Dr. K. Tanaka (KEK) for providing excellent and comfortable experimental environment, and especially for maintenance of the MRI superconducting magnet.

Sincere gratitude is expressed to Dr. T. Suehara (Kyushu U.), Dr. Y. Sasaki, Mr. G. Akimoto (UTokyo), Prof. A. P. Mills, Jr. (UC Riverside), Dr. H. A. Torii, Dr. T. Tanabe (UTokyo), and Prof. W. Hardy (TRIUMF) for useful discussions.

Warm thanks are due to facilities and the entire members of the Cryogenics Science Center at KEK without whose excellent support this experiment could not have been successfully performed.

I also would like to thank all staffs and colleagues of Department of Physics and ICEPP (UTokyo) for all their support.

Finally, I thank my parents, grandparents, brother, and all my relatives for their warm and kind support.

# Contents

<b>Acknowledgements</b>	<b>ii</b>
<b>1 Introduction</b>	<b>1</b>
1.1 Positronium . . . . .	1
1.2 Hyperfine Splitting of Positronium . . . . .	2
1.3 Theoretical Calculation of Ps-HFS . . . . .	2
1.4 Measurements of Ps-HFS . . . . .	3
1.4.1 Principle of indirect measurement using the Zeeman effect	3
1.4.2 Theoretical resonance line . . . . .	5
1.4.3 Previous Results of Measurements . . . . .	7
1.5 Discrepancy between Measurements and Theory . . . . .	9
1.5.1 Miscalculation of the theoretical value . . . . .	9
1.5.2 Common systematic uncertainties in the previous experi- ments . . . . .	10
1.5.3 New physics beyond the Standard Model . . . . .	10
<b>2 Principle</b>	<b>11</b>
2.1 Possible systematic uncertainties in the previous experiments . .	11
2.1.1 Possible non-uniformity of the magnetic field . . . . .	11
2.1.2 Non-thermalized o-Ps effect . . . . .	11
2.2 New methods . . . . .	14
2.2.1 Large bore superconducting magnet . . . . .	14
2.2.2 Timing information . . . . .	15
2.2.3 High performance $\gamma$ ray detectors . . . . .	15
<b>3 Experimental Setup</b>	<b>19</b>
3.1 Overview of the apparatus . . . . .	19
3.2 Static magnetic field . . . . .	22
3.3 Positron source and $\beta$ -tagging system . . . . .	23
3.3.1 Source holder . . . . .	27
3.3.2 Plastic scintillator and fused quartz light guide . . . . .	27
3.3.3 Fine mesh PMTs . . . . .	27
3.4 RF system . . . . .	28
3.4.1 RF supply . . . . .	28
3.4.2 Monitor . . . . .	34
3.4.3 Feedback . . . . .	35
3.5 Gas . . . . .	36
3.5.1 Gas-handling system . . . . .	37

3.5.2	Slow positron background . . . . .	37
3.5.3	Pickoff background . . . . .	38
3.6	Gamma ray detectors . . . . .	38
3.6.1	LaBr <sub>3</sub> (Ce) . . . . .	38
3.6.2	UVT light guide . . . . .	41
3.7	Electronics . . . . .	44
3.7.1	Overview of DAQ . . . . .	44
3.7.2	CAMAC . . . . .	50
3.8	Monte Carlo simulation . . . . .	50
3.9	Ps Thermalization Measurement . . . . .	53
3.10	Data acquisition . . . . .	53
<b>4</b>	<b>Analysis</b>	<b>54</b>
4.1	Basic cuts and calibrations . . . . .	54
4.1.1	Cut: Time difference of the two PS signals . . . . .	54
4.1.2	Calibration: Energy of the plastic scintillator . . . . .	55
4.1.3	Calibration: Energy of the LaBr <sub>3</sub> (Ce) scintillators . . . . .	55
4.1.4	Time walk correction . . . . .	56
4.1.5	Cut: Energy difference of the plastic scintillator . . . . .	58
4.1.6	Cut: Time difference of LaBr <sub>3</sub> (Ce) . . . . .	58
4.1.7	Summary of cuts . . . . .	58
4.2	Decay rate of Ps . . . . .	61
4.2.1	Deduction of the true signal timing distribution . . . . .	61
4.2.2	Fitting timing spectra of RF-OFF . . . . .	61
4.3	Timing windows . . . . .	63
4.4	Energy spectra . . . . .	64
4.5	The Zeeman resonance line . . . . .	64
<b>5</b>	<b>Results and Discussion</b>	<b>66</b>
5.1	Fitting of the Zeeman resonance lines . . . . .	66
5.2	Systematic errors . . . . .	81
5.2.1	Material Effect . . . . .	81
5.2.2	Magnetic Field . . . . .	82
5.2.3	RF System . . . . .	83
5.2.4	Others . . . . .	83
5.3	Ps-HFS value . . . . .	85
5.4	Non-thermalized Ps effect . . . . .	86
5.5	Future prospects . . . . .	86
<b>6</b>	<b>Conclusion</b>	<b>88</b>
<b>A</b>	<b>Run Summary</b>	<b>89</b>
A.1	Temperature control . . . . .	89
A.2	Run table . . . . .	90
<b>B</b>	<b>Ps Thermalization Measurement</b>	<b>94</b>
B.1	Experimental setup . . . . .	94
B.1.1	Overview of the apparatus . . . . .	94
B.1.2	Electronics circuit . . . . .	94
B.1.3	Monte Carlo simulation . . . . .	95

---

B.2 Results . . . . .	106
<b>C Final Fitting Parameters</b>	<b>108</b>

# List of Figures

1.1	Energy levels of the ground state Ps . . . . .	4
1.2	History plot of Ps-HFS measurements . . . . .	8
1.3	Positronium HFS . . . . .	9
2.1	Time evolution of Ps mean kinetic energy . . . . .	13
2.2	Time evolution of lifetime-weighted Ps mean velocity . . . . .	13
2.3	Non-thermalized Ps effect . . . . .	14
2.4	Non-thermalized Ps effect on HFS . . . . .	15
2.5	Time evolution of $2\gamma$ annihilation rate ( $S_{2\gamma}$ ) . . . . .	16
2.6	Time evolution of $2\gamma$ transition rate . . . . .	16
2.7	$2\gamma$ decay rate without timing information . . . . .	17
2.8	$2\gamma$ decay rate with a timing window of 35–155 ns . . . . .	17
3.1	Whole system of our experimental setup . . . . .	20
3.2	Top view in the magnet . . . . .	20
3.3	Photographs of the experimental setup around the magnet . . . . .	21
3.4	Static magnetic field distribution without compensation magnets . . . . .	23
3.5	Static magnetic field distribution with compensation magnet (before Ps-HFS measurement) . . . . .	24
3.6	Static magnetic field distribution with compensation magnet (after Ps-HFS measurement) . . . . .	25
3.7	Time fluctuation of the static magnetic field . . . . .	26
3.8	Decay scheme of $^{22}\text{Na}$ . . . . .	26
3.9	$\beta$ -tagging system . . . . .	27
3.10	Polar angle to the magnetic field . . . . .	28
3.11	Polar angle dependence of the gain of fine mesh PMTs in a magnetic field . . . . .	29
3.12	Polar angle dependence of the energy resolution of fine mesh PMTs in a magnetic field . . . . .	29
3.13	Polar angle dependence of the timing resolution of fine mesh PMTs in a magnetic field . . . . .	30
3.14	RF circuit . . . . .	31
3.15	RF power at discharge as a function of gas pressure . . . . .	32
3.16	Photograph of the RF cavity . . . . .	32
3.17	Magnetic field of the $\text{TM}_{110}$ mode . . . . .	33
3.18	Relative power as a function of time . . . . .	35
3.19	Distribution of AMP output power . . . . .	36
3.20	$\text{LaBr}_3(\text{Ce})$ scintillators . . . . .	39

3.21	Background energy spectra of LaBr <sub>3</sub> (Ce) . . . . .	40
3.22	Decay scheme of <sup>138</sup> La . . . . .	41
3.23	UVT light guide . . . . .	42
3.24	Light guide length dependence of light output . . . . .	43
3.25	Light guide bending angle dependence of light output . . . . .	43
3.26	Change of light output and energy resolution with light guide . . . . .	44
3.27	DAQ of $\beta$ -tagging system . . . . .	45
3.28	DAQ of LaBr <sub>3</sub> (Ce) system . . . . .	46
3.29	DAQ of trigger system . . . . .	47
3.30	DAQ of gates generation system . . . . .	48
3.31	DAQ of visual scaler system . . . . .	49
3.32	Timing chart of electronics . . . . .	49
3.33	DAQ system . . . . .	51
3.34	Side view of the geometry in the MC simulation . . . . .	51
3.35	Bird's-eye view of the geometry in the MC simulation . . . . .	52
4.1	Time difference of the PMTs of the plastic scintillator . . . . .	55
4.2	Time walk correction of LaBr <sub>3</sub> (Ce) . . . . .	57
4.3	Time walk correction of the plastic scintillator . . . . .	59
4.4	Energy balance cut of the plastic scintillator . . . . .	60
4.5	Timing spectra ( $n=0.881$ amagat, $B=0.865\ 733\ 6$ T) . . . . .	62
4.6	Fitting of RF-OFF timing spectrum ( $n=0.881$ amagat, $B=0.865\ 733\ 6$ T) . . . . .	63
4.7	Fitted $\Gamma_{\text{pick}}(n, \infty)$ as a function of gas density . . . . .	64
4.8	Energy spectra of the timing window of 50–60 ns ( $n=0.881$ amagat, $B=0.865\ 733\ 6$ T) . . . . .	65
5.1	Resonance lines at a gas density of 0.129 amagat . . . . .	68
5.2	Resonance lines at a gas density of 0.133 amagat . . . . .	69
5.3	Resonance lines at a gas density of 0.167 amagat . . . . .	70
5.4	Resonance lines at a gas density of 0.232 amagat . . . . .	71
5.5	Resonance lines at a gas density of 0.660 amagat . . . . .	72
5.6	Resonance lines at a gas density of 0.881 amagat . . . . .	73
5.7	Resonance lines at a gas density of 0.969 amagat . . . . .	74
5.8	Resonance lines at a gas density of 1.193 amagat . . . . .	75
5.9	Resonance lines at a gas density of 1.353 amagat . . . . .	76
5.10	Resonance lines at a gas density of 1.358 amagat . . . . .	77
5.11	Resonance lines at a gas density of 1.366 amagat . . . . .	78
5.12	Time evolutions of $\rho_{00}$ for various gas density. (Reproduced from Ref. [1]) . . . . .	79
5.13	Time evolutions of mean velocity of Ps for various gas density. (Reproduced from Ref. [1]) . . . . .	79
5.14	Time evolutions of pick-off annihilation rate for various gas density. (Reproduced from Ref. [1]) . . . . .	80
5.15	Time evolutions of $\Delta_{\text{HFS}}$ for various gas density. (Reproduced from Ref. [1]) . . . . .	80
5.16	Spatial distribution of gas temperature in the RF cavity ( $n=0.881$ amagat) . . . . .	82
5.17	Fitting-start-time dependence of $\Delta_{\text{HFS}}$ . . . . .	84
5.18	Fitting-end-time dependence of $\Delta_{\text{HFS}}$ . . . . .	84

5.19	$\Delta_{\text{HFS}}$ at each gas density . . . . .	86
5.20	Summary of $\Delta_{\text{HFS}}$ measurements from pas experiments and this work. . . . .	87
B.1	Side view of the setup of Ps thermalization measurement. . . . .	95
B.2	Front view of the setup of Ps thermalization measurement. . . . .	96
B.3	DAQ of Ps thermalization (Plastic scintillator 1) . . . . .	97
B.4	DAQ of Ps thermalization (Plastic scintillator 2) . . . . .	98
B.5	DAQ of Ps thermalization (Trigger) . . . . .	99
B.6	DAQ of Ps thermalization (Ge detector) . . . . .	100
B.7	DAQ of Ps thermalization (Ge Main Gate) . . . . .	101
B.8	DAQ of Ps thermalization (Ge TRP veto) . . . . .	102
B.9	DAQ of Ps thermalization (Ge ADCs' gates) . . . . .	103
B.10	DAQ of Ps thermalization (Clock system) . . . . .	104
B.11	Side view of the geometry in the MC simulation (thermalization measurement) . . . . .	105
B.12	Bird's-eye view of the geometry in the MC simulation (thermalization measurement) . . . . .	105
B.13	Pick-off ratio as a function of time (with aerogel) . . . . .	106
B.14	Pick-off ratio as a function of time (without aerogel) . . . . .	107
C.1	$D_1(n)$ . . . . .	108
C.2	$D_2(n)$ . . . . .	109
C.3	$\epsilon(n)$ . . . . .	109
C.4	$B_{\text{RF}}(n)$ . . . . .	110

# List of Tables

1.1	Rare decay modes of positronium . . . . .	2
1.2	History of Ps-HFS measurement . . . . .	8
3.1	Decay radiation of $^{22}\text{Na}$ . . . . .	26
3.2	Properties of $\text{LaBr}_3(\text{Ce})$ . . . . .	39
3.3	Decay radiation of $^{138}\text{La}$ . . . . .	40
4.1	Summary of cuts . . . . .	58
5.1	Summary of systematic errors . . . . .	81
A.1	Run table . . . . .	90
A.1	Run table . . . . .	91
A.1	Run table . . . . .	92
A.1	Run table . . . . .	93

# Chapter 1

## Introduction

### 1.1 Positronium

Positronium (Ps) is a bound state of an electron ( $e^-$ ) and a positron ( $e^+$ ). It is the lightest bound state in the hydrogen-like atoms. It is an ideal system for precision tests of bound-state QED since it is a purely leptonic atom and effectively free from the hadronic effects and the weak interactions. It is also suitable for searches of new physics, because it is a bound state of a particle and an anti-particle.

States of Ps is classified according to the principal quantum number  $n$ , the orbital angular momentum  $L$ , the spin angular momentum  $S$ , and the angular momentum projected on a quantization axis  $m$ . The ground state Ps ( $n = 1$ ,  $L = 0$ ) is classified according to the total spin  $S$  into two states; the spin singlet ( $S = 0$ ) state called parapositronium (p-Ps,  $1^1S_0$ ) and the spin triplet ( $S = 1$ ) state called orthopositronium (o-Ps,  $1^3S_1$ ). Positronium is sensitive to the structure of vacuum and searches for new particles. Parapositronium has the same quantum number as vacuum and o-Ps has the same quantum number as a photon.

Positronium has a parity under a charge-conjugation  $C$  of

$$C = (-1)^{L+S}. \quad (1.1)$$

Positronium is a fermion-antifermion system and decays into photons. Because a photon has intrinsically odd-parity under the  $C$ -transformation, p-Ps can decay only into even  $\gamma$ 's, on the other hand, o-Ps into odd  $\gamma$ 's.

$$\text{p-Ps} \rightarrow n\gamma, \quad n = 2, 4, 6, 8, \dots, \quad (1.2)$$

$$\text{o-Ps} \rightarrow n\gamma, \quad n = 3, 5, 7, 9, \dots \quad (1.3)$$

p-Ps decays mostly into  $2\gamma$ , whereas o-Ps into  $3\gamma$ . Other decay modes are summarized in Table 1.1. There are many experiments on other decay modes, but they are extremely suppressed. The decay rates of p-Ps ( $\Gamma_{\text{p-Ps}}$ ), and of o-Ps ( $\Gamma_{\text{o-Ps}}$ ) are

$$\Gamma_{\text{p-Ps}} = 7.9909(17) \text{ ns}^{-1} [2], \quad (1.4)$$

$$\Gamma_{\text{o-Ps}} = 7.0401(7) \mu\text{s}^{-1} [3]. \quad (1.5)$$

Table 1.1: Rare decay modes of positronium.

Decay mode	Branching ratio	Reference
p-Ps $\rightarrow 4\gamma$		$= 1.30(30) \times 10^{-6}$ [4]
	$\frac{\Gamma_{\text{p-Ps} \rightarrow 4\gamma}}{\Gamma_{\text{p-Ps} \rightarrow 2\gamma}}$	$= 1.50(11) \times 10^{-6}$ [5]
		$= 1.48(17) \times 10^{-6}$ [6]
		$= 1.19(26) \times 10^{-6}$ [7]
		$= 1.14(39) \times 10^{-6}$ [8]
o-Ps $\rightarrow 5\gamma$	$\frac{\Gamma_{\text{o-Ps} \rightarrow 5\gamma}}{\Gamma_{\text{o-Ps} \rightarrow 3\gamma}}$	$(= 2.2^{+2.6}_{-1.8}) \times 10^{-6}$ [9]
		$= 1.7(11) \times 10^{-6}$ [8]
o-Ps $\rightarrow \nu\bar{\nu}$	$\frac{\Gamma_{\text{o-Ps} \rightarrow \nu\bar{\nu}}}{\Gamma_{\text{o-Ps} \rightarrow 3\gamma}}$	$< 5.8 \times 10^{-4}$ (90% CL) [10]
		$< 2.8 \times 10^{-6}$ (90% CL) [11]
		$< 4.2 \times 10^{-7}$ (90% CL) [12]

## 1.2 Hyperfine Splitting of Positronium

Precise tests of positronium and other hydrogen-like atoms are summarized in Ref. [13]. Many values such as decay rates and differences of energy levels have been measured and most of them are consistent with QED predictions. The  $1S$  hyperfine splitting (HFS) of Ps (Ps-HFS,  $\Delta_{\text{HFS}}$ ) is the difference of energy levels between p-Ps and o-Ps. The energy of o-Ps is higher than p-Ps by  $\Delta_{\text{HFS}} \approx 203$  GHz (0.84 meV). It is one of the most precisely tested values. Ps-HFS is caused by the spin-spin interaction and the quantum oscillation of o-Ps  $\rightarrow \gamma^* \rightarrow$  o-Ps. The spin-spin interaction becomes large because of the light mass of Ps. The contribution of the quantum oscillation is about 30%.

## 1.3 Theoretical Calculation of Ps-HFS

The bound-state QED has difficulty in higher-order calculations because of their non-perturbative nature, which is different from the situation of free particles. Recently a technique to calculate higher-order corrections using a theory of non-relativistic effective field has been developed. It is called non-relativistic quantum electrodynamics (NRQED), which is advancing studies of bound-state QED. The Ps-HFS value is calculated up to  $O(\alpha^3)$  correction as follows [14]:

$$\begin{aligned} \Delta_{\text{HFS}}^{\text{th}} &= \Delta_{\text{HFS}0}^{\text{th}} \left\{ 1 - \frac{\alpha}{\pi} \left( \frac{32}{21} + \frac{6}{7} \ln 2 \right) + \frac{5}{14} \alpha^2 \ln \frac{1}{\alpha} \right. \\ &\quad + \left( \frac{\alpha}{\pi} \right)^2 \left[ \frac{1367}{378} - \frac{5197}{2016} \pi^2 + \left( \frac{6}{7} + \frac{221}{84} \pi^2 \right) \ln 2 - \frac{159}{56} \zeta(3) \right] \\ &\quad \left. - \frac{3}{2} \frac{\alpha^3}{\pi} \ln^2 \frac{1}{\alpha} + \left( \frac{62}{15} - \frac{68}{7} \ln 2 \right) \frac{\alpha^3}{\pi} \ln \frac{1}{\alpha} + D \left( \frac{\alpha}{\pi} \right)^3 + \dots \right\}, \end{aligned} \quad (1.6)$$

$$\Delta_{\text{HFS}0}^{\text{th}} = \frac{7}{12} m_e \alpha^4, \quad (1.7)$$

where  $m_e$  is the electron mass,  $\alpha$  is the fine-structure constant, and  $D$  is an unknown constant. The leading order  $\Delta_{\text{HFS}0}^{\text{th}}$  was calculated firstly by J. Pirenne in 1947 [15], and confirmed later [16, 17]. The  $O(\alpha)$  correction is calculated by Karplus and Klein in 1952 [18]. Many effects are calculated in the  $O(\alpha^2)$

correction until 2000 [19, 20, 21, 22, 23, 24, 25, 26, 27, 28, 29, 30, 31, 32]. The  $O(\alpha^3 \ln^2 \alpha^{-1})$  term is calculated by Karshenboim in 1993 [33]. It was not until 2000s that the  $O(\alpha^3 \ln \alpha^{-1})$  correction is calculated firstly by Kniehl and Penin[14] and confirmed later [34, 35]. Recently, some contributions of the  $O(\alpha^3)$  term have been calculated [36, 37] to be  $\approx +1$  ppm, although not all contributions have been obtained yet. Including all the corrections calculated up to  $O(\alpha^3 \ln \alpha^{-1})$ , the theoretical value results in

$$\Delta_{\text{HFS}}^{\text{th}} = 203.391\,69(41) \text{ GHz (2.0 ppm) [14, 34, 35]}, \quad (1.8)$$

where the error estimation of Ref. [14] is used.

## 1.4 Measurements of Ps-HFS

Ps-HFS was firstly measured by Deutsch and Brown in 1952 [38]. After that measurement, precise measurements were performed by independent two groups. All the previous precise measurements obtained Ps-HFS indirectly by stimulating the Zeeman transition under a static magnetic field in order to avoid a difficulty in precisely measuring Ps-HFS by stimulating  $\Delta_{\text{HFS}}$  directly.

### 1.4.1 Principle of indirect measurement using the Zeeman effect

The four spin eigenstates of Ps is described as

$$|0, 0\rangle = \frac{1}{\sqrt{2}} (|\uparrow\downarrow\rangle - |\downarrow\uparrow\rangle), \quad (1.9)$$

$$|1, 0\rangle = \frac{1}{\sqrt{2}} (|\uparrow\downarrow\rangle + |\downarrow\uparrow\rangle), \quad (1.10)$$

$$|1, 1\rangle = |\uparrow\uparrow\rangle, \quad (1.11)$$

$$|1, -1\rangle = |\downarrow\downarrow\rangle, \quad (1.12)$$

where the Ps spin eigenstates with the total spin  $S$  and the magnetic quantum number  $m_z$  is described as  $|S, m_z\rangle$ ,  $\uparrow$  and  $\downarrow$  indicate the spin of the electron, and  $\uparrow$  and  $\downarrow$  indicate that of the positron. In this thesis, the quantization axis is chosen to be the  $z$  axis.

Figure 1.1 shows the energy levels of the ground state Ps as a function of a static magnetic field strength. In a static magnetic field, the  $|1, 0\rangle$  and the  $|0, 0\rangle$  states mix and energy eigenstates of Ps become  $|+\rangle$  and  $|-\rangle$  states. This is the Zeeman effect, and the energy splitting  $\Delta_{\text{Zeeman}}$  is the Zeeman splitting.

The relationship between  $\Delta_{\text{HFS}}$  and  $\Delta_{\text{Zeeman}}$  at a static magnetic field  $B$  is approximately given by the Breit-Rabi expression <sup>1</sup>

$$\Delta_{\text{Zeeman}} \approx \frac{1}{2} \Delta_{\text{HFS}} \left( \sqrt{1 + 4q^2} - 1 \right), \quad (1.13)$$

<sup>1</sup>This equation is approximation without an effect of Ps decay, so that the exact solution is smaller than this by about 10 ppm. This fact does not matter the final results of the previous experiments since the two most precise experiments applied a correction of a difference between the Breit-Wigner function and a theoretical resonance line calculated from the Hamiltonian.

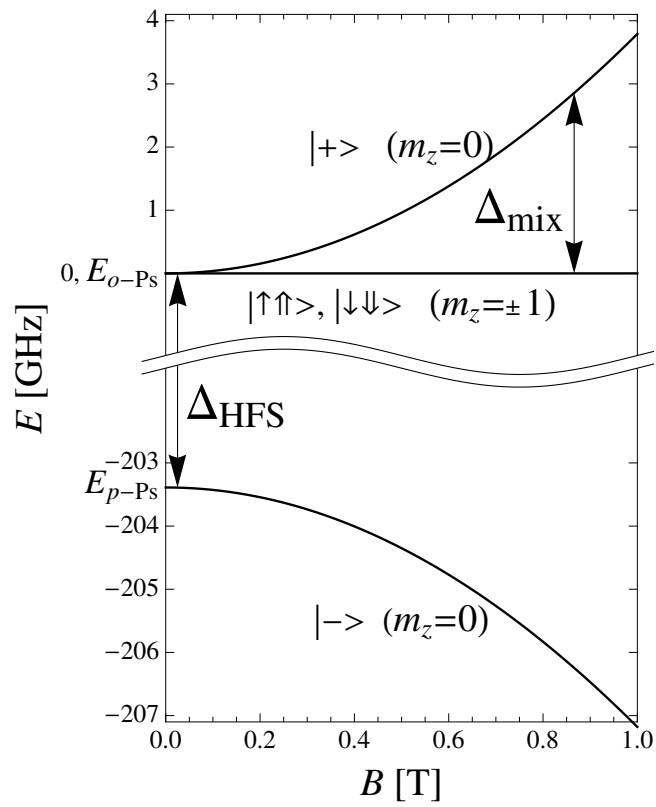


Figure 1.1: Energy levels of the ground state Ps. The horizontal axis shows strength of static magnetic field.

where  $q$  is given as  $g'\mu_B B / (h\Delta_{\text{HFS}})$ ,  $g' = g(1 - \frac{5}{24}\alpha^2)$  is the  $g$  factor of the positron (electron) in Ps [39, 40, 41, 42],  $\mu_B$  is the Bohr magneton, and  $h$  is the Planck constant.

When microwave with a frequency of  $\Delta_{\text{Zeeman}}$  is applied, a transition between the  $m_z = \pm 1$  states and the  $|+\rangle$  state occurs. This transition makes  $2\gamma$  decay rate higher and  $3\gamma$  decay rate lower since the  $|1, \pm 1\rangle$  states decay into  $3\gamma$  whereas the  $|+\rangle$  state, which is a mixed state of  $|0, 0\rangle$  and  $|1, 0\rangle$  states, decays mostly into  $2\gamma$ . The experimental signature is this change in the annihilation rates caused by the Zeeman transition.

### 1.4.2 Theoretical resonance line

In our experiment,  $\Delta_{\text{HFS}}$  is directly determined using the theoretical resonance shape of  $\Delta_{\text{Zeeman}}$  obtained using the density matrix of Ps spin states because the Breit-Rabi equation is not precise enough at ppm level. The line shape is slightly different from the Breit-Wigner function (Lorentzian) because of the non-linear dependence on the static magnetic field strength. The following calculation is based on Refs. [43, 44]. The basis for the four spin eigenstates of Ps is defined as

$$\begin{pmatrix} \psi_0 \\ \psi_1 \\ \psi_2 \\ \psi_3 \end{pmatrix} = \begin{pmatrix} |0, 0\rangle \\ |1, 0\rangle \\ |1, 1\rangle \\ |1, -1\rangle \end{pmatrix}. \quad (1.14)$$

The Hamiltonian  $H_0$  including the Ps decay without any external fields or interactions becomes

$$H_0 = \begin{pmatrix} -\frac{h\Delta_{\text{HFS}}}{2} - \frac{i\hbar\Gamma_{\text{p-Ps}}}{2} & 0 & 0 & 0 \\ 0 & \frac{h\Delta_{\text{HFS}}}{2} - \frac{i\hbar\Gamma_{\text{o-Ps}}}{2} & 0 & 0 \\ 0 & 0 & \frac{h\Delta_{\text{HFS}}}{2} - \frac{i\hbar\Gamma_{\text{o-Ps}}}{2} & 0 \\ 0 & 0 & 0 & \frac{h\Delta_{\text{HFS}}}{2} - \frac{i\hbar\Gamma_{\text{o-Ps}}}{2} \end{pmatrix}, \quad (1.15)$$

where the zero of energy is chosen midway between p-Ps and o-Ps levels. An external magnetic field  $\mathbf{B}(t)$  is applied as follows:

$$\mathbf{B}(t) = B\hat{\mathbf{z}} + B_{\text{RF}}\hat{\mathbf{x}}\cos(\omega t), \quad (1.16)$$

where  $\hat{\mathbf{z}}$  and  $\hat{\mathbf{x}}$  are the unit vectors for the z and x directions respectively,  $B_{\text{RF}}$  is the magnetic field strength induced by the microwaves,  $\omega$  is the frequency of the microwaves, and  $t$  is the time after the Ps is formed. The phase of the microwaves is randomly distributed for each Ps in this experiment, but the effect on the determination of  $\Delta_{\text{HFS}}$  is less than 0.1 ppm so that an arbitrary phase can be taken in the calculation.

The interaction Hamiltonian  $V$  in the magnetic field is

$$V = -\boldsymbol{\mu} \cdot \mathbf{B} \quad (1.17)$$

$$= g'\mu_B \mathbf{B} \cdot (\mathbf{S}_- - \mathbf{S}_+) \quad (1.18)$$

$$= \frac{g'\mu_B}{2} \mathbf{B} \cdot (\boldsymbol{\sigma}_- - \boldsymbol{\sigma}_+) \quad (1.19)$$

$$= \frac{g'\mu_B}{2} [B(\sigma_{z-} - \sigma_{z+}) + B_{\text{RF}}\cos(\omega t)(\sigma_{x-} - \sigma_{x+})], \quad (1.20)$$

where  $\boldsymbol{\mu}$  is the magnetic moment of Ps,  $\mathbf{S}$  is the spin operator of the electron and the positron respectively, and  $\boldsymbol{\sigma}$  indicates the Pauli matrices which are described as

$$\sigma_x = \begin{pmatrix} 0 & 1 \\ 1 & 0 \end{pmatrix}, \sigma_y = \begin{pmatrix} 0 & -i \\ i & 0 \end{pmatrix}, \sigma_z = \begin{pmatrix} 1 & 0 \\ 0 & -1 \end{pmatrix}, \quad (1.21)$$

with the quantization axis of z, and subscripts + and - indicate the positron and the electron, respectively. Substituting Eq. (1.21) in Eq. (1.20),  $V$  is calculated as

$$V = \begin{pmatrix} 0 & q & -r & r \\ q & 0 & 0 & 0 \\ -r & 0 & 0 & 0 \\ r & 0 & 0 & 0 \end{pmatrix} h\Delta_{\text{HFS}}, \quad (1.22)$$

where  $r = g'\mu_B B_{\text{RF}} \cos(\omega t) / (\sqrt{2}h\Delta_{\text{HFS}}(t))$ . The total Hamiltonian  $H = H_0 + V$  becomes

$$H = h\Delta_{\text{HFS}}(t) \times \begin{pmatrix} -\frac{1}{2} - \frac{i}{2}\gamma_s & -q & r & -r \\ -q & \frac{1}{2} - \frac{i}{2}\gamma_t & 0 & 0 \\ r & 0 & \frac{1}{2} - \frac{i}{2}\gamma_t & 0 \\ -r & 0 & 0 & \frac{1}{2} - \frac{i}{2}\gamma_t \end{pmatrix}, \quad (1.23)$$

where  $\gamma_s = \Gamma'_{\text{p-Ps}}(t) / (2\pi\Delta_{\text{HFS}}(t))$ ,  $\gamma_t = \Gamma'_{\text{o-Ps}}(t) / (2\pi\Delta_{\text{HFS}}(t))$ ,  $\Gamma'_{\text{p-Ps}}(t) = \Gamma_{\text{p-Ps}} + \Gamma_{\text{pick}}(t)$ ,  $\Gamma'_{\text{o-Ps}}(t) = \Gamma_{\text{o-Ps}} + \Gamma_{\text{pick}}(t)$ , and  $\Gamma_{\text{pick}}(t)$  is the pick-off ( $\text{Ps} + e^- \rightarrow 2\gamma + e^-$ ) annihilation rate. The time-dependence of  $\Delta_{\text{HFS}}$  and  $\Gamma_{\text{pick}}$  are caused by Ps thermalization, which is described later.

The  $4 \times 4$  density matrix  $\rho(t)$  evolves with the time-dependent Schrödinger equation,

$$i\hbar\dot{\rho} = H\rho - \rho H^\dagger, \quad (1.24)$$

where the  $i, j$  elements of  $\rho(t)$  are defined as  $\rho_{ij}(t) \equiv \langle \psi_i | \psi(t) \rangle \langle \psi(t) | \psi_j \rangle$  and the initial state  $\rho(0)$  with an assumption of electron unpolarized is given as [45]

$$\rho(0) = \begin{pmatrix} \frac{1}{4} & -\frac{P \cos \theta}{4} & \frac{P \sin \theta e^{i\phi}}{4\sqrt{2}} & -\frac{P \sin \theta e^{-i\phi}}{4\sqrt{2}} \\ -\frac{P \cos \theta}{4} & \frac{1}{4} & \frac{P \sin \theta e^{i\phi}}{4\sqrt{2}} & \frac{P \sin \theta e^{-i\phi}}{4\sqrt{2}} \\ \frac{P \sin \theta e^{-i\phi}}{4\sqrt{2}} & \frac{P \sin \theta e^{-i\phi}}{4\sqrt{2}} & \frac{(1+P \cos \theta)}{4} & 0 \\ -\frac{P \sin \theta e^{i\phi}}{4\sqrt{2}} & \frac{P \sin \theta e^{i\phi}}{4\sqrt{2}} & 0 & \frac{(1-P \cos \theta)}{4} \end{pmatrix}, \quad (1.25)$$

where  $P$  is the polarization of the positron,  $\theta$  is the polar angle of the positron polarization vector, and  $\phi$  is the azimuthal angle of that.

The  $2\gamma$  annihilation probability ( $S_{2\gamma}$ ), and the  $3\gamma$  annihilation probability ( $S_{3\gamma}$ ) are calculated between  $t = t_0$  and  $t = t_1$  as

$$S_{2\gamma} = \int_{t_0}^{t_1} \left( \Gamma'_{\text{p-Ps}}(t) \rho_{00}(t) + \Gamma_{\text{pick}}(t) \sum_{i=1}^3 \rho_{ii}(t) \right) dt, \quad (1.26)$$

$$S_{3\gamma} = \int_{t_0}^{t_1} \Gamma_{\text{o-Ps}} \sum_{i=1}^3 \rho_{ii}(t) dt. \quad (1.27)$$

Furthermore,  $S_{3\gamma}$  is divided into two components to obtain the experimental resonance line shape because of the different angular distributions of decay  $\gamma$

rays from Ps between  $|1, \pm 1\rangle$  and  $|1, 0\rangle$  states [46]. The annihilation probability of the  $|1, \pm 1\rangle$  state,  $S_{|1, \pm 1\rangle} \equiv S_{|1, 1\rangle} + S_{|1, -1\rangle}$ , and the annihilation probability of the  $|1, 0\rangle$  state,  $S_{|1, 0\rangle}$ , are obtained by

$$S_{|1, \pm 1\rangle} = \int_{t_0}^{t_1} \Gamma_{\text{o-Ps}} (\rho_{22}(t) + \rho_{33}(t)) dt, \quad (1.28)$$

$$S_{|1, 0\rangle} = \int_{t_0}^{t_1} \Gamma_{\text{o-Ps}} \rho_{11}(t) dt. \quad (1.29)$$

These calculations are used later in Eqs. (5.1) and (5.2) for fitting experimental data.

### 1.4.3 Previous Results of Measurements

The history of the measurements is summarized in Table 1.2 and Fig. 1.2.

Table 1.2: History of Ps-HFS measurement.

Year	$\Delta_{\text{HFS}}$ (GHz)	Error (ppm)	References
1952	203.2(3)	1500	[38]
1954	203.38(4)	200	[47]
1955	203.35(5)	250	[47]
1957	203.33(4)	200	[48]
1970	203.403(12)	58	[49]
1972	203.396(5)	24	[50]
1975	203.3870(16)	8	[51]
1977	203.384(4)	20	[52]
1977	203.3849(12)	6	[53]
1983	203.3875(16)	8	[43]
1984	203.38910(74)	3.6	[44]

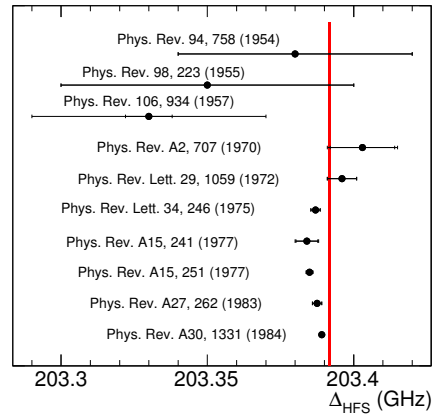


Figure 1.2: History plot of Ps-HFS measurements. The red band indicates the theoretical calculation described in Eq. (1.8). The first measurement [38] is not plotted since the error is large.

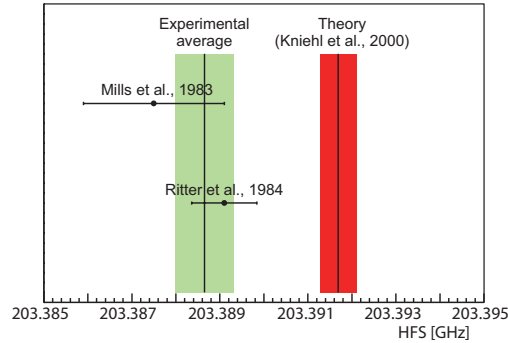


Figure 1.3: Positronium HFS. The points with error bars are the experimental values [43, 44], the green band is their average Eq. (1.32), and the red band is the QED calculation of Eq. (1.8).

Two most precise results are

$$\Delta_{\text{HFS}} = 203.3875(16) \text{ GHz (8 ppm) [43],} \quad (1.30)$$

$$\Delta_{\text{HFS}} = 203.38910(74) \text{ GHz (3.6 ppm) [44].} \quad (1.31)$$

These values include results of their own past measurements [51, 53], and averaging these two values results in

$$\Delta_{\text{HFS}}^{\text{exp}} = 203.38865(67) \text{ GHz (3.3 ppm) [51, 43, 44].} \quad (1.32)$$

## 1.5 Discrepancy between Measurements and Theory

Figure 1.3 shows the comparison of the measured values of Eq. (1.30), (1.31), their average Eq. (1.32), and the QED calculation of Eq. (1.8). There is a discrepancy of 3.04(79) MHz (15 ppm) between the previous measurements and the theoretical calculation. The discrepancy is 3.9 standard deviations (s.d.) level, so it is not likely a statistical fluctuation. The following three reasons are possible to explain this discrepancy.

### 1.5.1 Miscalculation of the theoretical value

NRQED might not be applied at higher orders. Although NRQED is validated up to  $O(\alpha^2)$  corrections in the o-Ps lifetime measurement [3], no precise test of  $O(\alpha^3)$  corrections has been performed. The other probability is a simple miscalculation, but this probability is quite small since the different three calculations show the same result.

### **1.5.2 Common systematic uncertainties in the previous experiments**

The discrepancy occurs if there are any common systematic uncertainties which are not properly treated in the previous experiments. Possible common systematic uncertainties are described in Sec. 2.1.

### **1.5.3 New physics beyond the Standard Model**

If the discrepancy is real, it indicates the existence of an unknown particle. For example, a new pseudo-scalar with a mass of  $O(\text{MeV})$  and weak coupling of ( $\alpha \approx 10^{-8}$ ) can cause this discrepancy.

# Chapter 2

## Principle

In this chapter, possible systematic uncertainties of all previous experiments are discussed. I propose the new method to reduce these uncertainties.

### 2.1 Possible systematic uncertainties in the previous experiments

There are the following two possible common systematic uncertainties in the previous experiments.

#### 2.1.1 Possible non-uniformity of the magnetic field

The precise measurements using Zeeman splitting acquires an uniformity and an accuracy of the static magnetic field to be ppm level, since an uncertainty and a non-uniformity of the static magnetic field directly affect  $\Delta_{\text{HFS}}$ . An inhomogeneity of the static magnetic field was mentioned as the most significant systematic uncertainty in the previous experiments. In the previous experiments, the static magnetic field is provided using normal conducting magnets and the field is carefully shimmed to obtain ppm-level uniformity over the relevant volume of  $\approx 10 \text{ cm}^3$  where Ps  $2\gamma$  annihilations are observed. However, the Ps formation region is in fact a volume of  $\approx 100 \text{ cm}^3$ , and there is still a possibility of more uncertainty from the inhomogeneity of the static magnetic field.

#### 2.1.2 Non-thermalized o-Ps effect

Gas molecules are necessary to form Ps in all experiments, but they produce electric fields around the Ps which in turn affects  $\Delta_{\text{HFS}}$ . This material effect (Stark effect) must be properly accounted for to obtain  $\Delta_{\text{HFS}}$  in vacuum. In all previous experiments, Ps-HFS is measured at various gas densities and linearly extrapolated to vacuum in order to estimate this effect. This method is valid only when Ps is well-thermalized and the shift of energy levels is proportional to the gas density. However, a calculation of the Stark effect on atomic collisions under the Lennard-Jones potential [54] shows that this effect is proportional to  $n[v(t)]^{3/5}$ , where  $n$  is the number density of gas molecules and  $v(t)$  is the Ps

mean velocity. The time dependence of  $v(t)$  is caused by the Ps thermalization process. o-Ps has a kinetic energy of  $O(\text{eV})$  just after the formation, and slows down by collision toward the ultimate thermal energy of about  $0.03 \text{ eV}$  at room temperature. This process is called thermalization. It takes much time for Ps to be well thermalized in materials with low density. Because of this fact, non-thermalized Ps has to be taken into account carefully. The effect due to non-thermalized Ps has already been shown to be significant in the so-called o-Ps lifetime puzzle [55, 56, 57], which was a history of a disagreement between experimental o-Ps values and theoretical calculations which was finally solved by taking into account the effect. This effect is a possible serious systematic uncertainty in the Ps-HFS case. The non-thermalized Ps effect is estimated hereinafter based on Refs. [58, 59].

The differential equation of time evolution of Ps thermalization in gas is

$$\frac{dE_{\text{av}}(t)}{dt} = -\sqrt{2m_{\text{Ps}}E_{\text{av}}(t)} \left( E_{\text{av}}(t) - \frac{3}{2}k_B T \right) \frac{8}{3} \sqrt{\frac{2}{3\pi}} \frac{2\sigma_m n}{M}, \quad (2.1)$$

where  $t$  is the time since Ps is formed,  $E_{\text{av}}(t)$  is the mean Ps kinetic energy at time  $t$ ,  $\sigma_m$  is the momentum-transfer cross section of Ps collision with gas molecules,  $n$  is the number density of gas molecules,  $M$  is the mass of the gas molecule,  $m_{\text{Ps}}$  is the Ps mass,  $k_B$  is the Boltzmann constant, and  $T$  is the temperature of the gas. The solution of this equation is

$$E_{\text{av}}(t) = \left( \frac{1 + Ae^{-bt}}{1 - Ae^{-bt}} \right)^2 \frac{3}{2} k_B T, \quad (2.2)$$

where

$$b = \frac{8}{3} \sqrt{\frac{2}{3\pi}} \frac{2\sigma_m n}{M} \sqrt{3m_{\text{Ps}}k_B T}, \quad (2.3)$$

$A$  is defined by the initial condition described as

$$A = \frac{\sqrt{E_0} - \sqrt{\frac{3}{2}k_B T}}{\sqrt{E_0} + \sqrt{\frac{3}{2}k_B T}}, \quad (2.4)$$

where  $E_0 = E_{\text{av}}(0)$  is the initial kinetic energy of Ps.

Let's discuss thermalization process in nitrogen gas with a typical  $E_0 = 2 \text{ eV}$  [60],  $T = 273.15 \text{ K}$  for example. Nitrogen gas is used in Ref. [44], and  $\sigma_m$  of nitrogen is  $\sigma_m(\text{N}_2) = (25 \pm 14) \times 10^{-16} \text{ cm}^2$  [61, 60, 59]. Figure 2.1 shows the time evolution of the Ps mean kinetic energy calculated by Eq. (2.2) at 0.1, 1, and 2 atm. The term  $n[v(t)]^{3/5}$  has to be considered. The Ps mean velocity is calculated from kinetic energy as  $v(t) \approx \sqrt{\frac{2}{m_{\text{Ps}}} E_{\text{av}}(t)}$ . The effect of non-thermalized Ps without any timing information is approximately estimated by  $\int_0^\infty n[v(t)]^{3/5} \exp(-\Gamma_{\text{o-Ps}} t) dt$ , where only the weight of decrease of the number of Ps of  $\exp(-\Gamma_{\text{o-Ps}} t)$  is taken into account. The time evolution of  $\Delta_{\text{HFS}}$  is ignored here, although it has not so small effect. Figure 2.2 shows the lifetime-weighted Ps velocity<sup>3/5</sup>  $[v(t)]^{3/5} \exp(-\Gamma_{\text{o-Ps}} t)$ . Each area of this figure shows the material effect at each gas density. Figure 2.3 shows the non-thermalized Ps effect as a function of gas density. It is estimated by integrating Fig. 2.2 in the timing  $t = 0 - 1000 \text{ ns}$ . A Non-linear structure is clearly seen at low pressure region. Figure 2.4

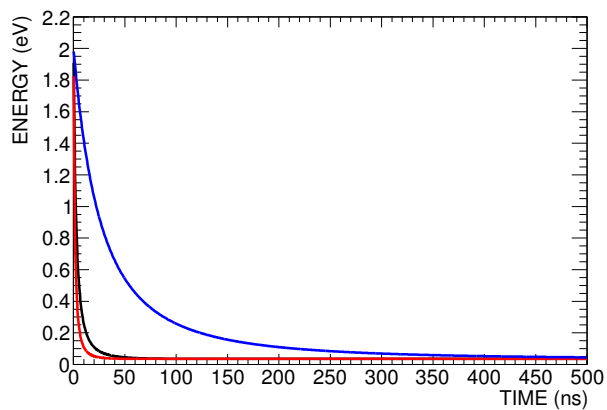


Figure 2.1: Time evolution of Ps mean kinetic energy in nitrogen gas with an initial kinetic energy of 2 eV and temperature of 273.15 K. The blue line is at 0.1 atm, the black line is at 1 atm, and the red line is at 2 atm.

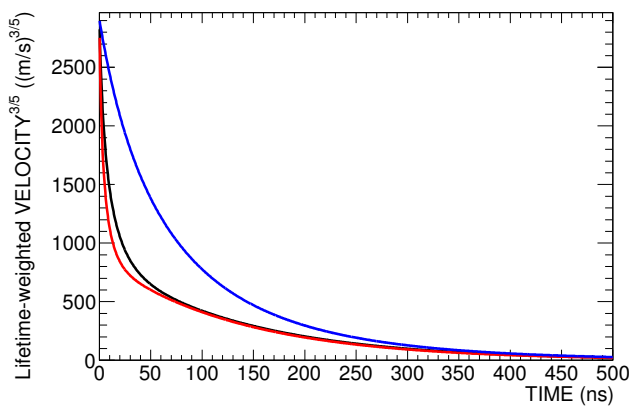


Figure 2.2: Time evolution of lifetime-weighted Ps mean velocity in nitrogen gas; An initial kinetic energy is 2 eV, and temperature is 273.15 K. The blue line is at 0.1 atm, the black line is at 1 atm, and the red line is at 2 atm.

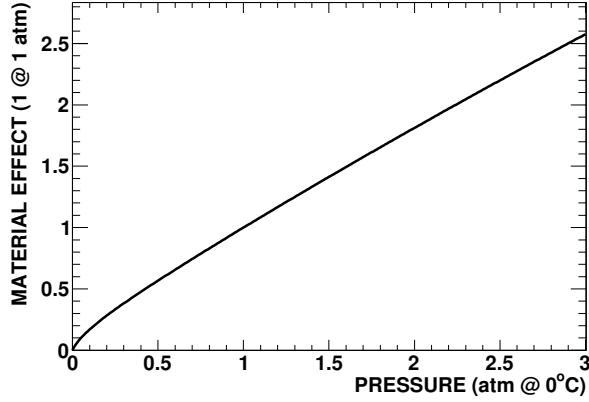


Figure 2.3: Non-thermalized Ps effect in nitrogen gas; An initial kinetic energy is 2 eV, and temperature is 273.15 K. The vertical axis is normalized to unity at 1 atm.

shows a linear-fit of toy data based on Fig. 2.3. The toy data are plotted on the line of Fig. 2.3 at the gas densities of the data of Ref. [44], and the error bars are taken from the same data normalized by the amount of the material effect. The linear-fit results in a slope of  $0.83(10)$  /atm, and y-intercept of  $0.140(72)$ . The gas density dependence of Ps-HFS in nitrogen is  $-33(4)$  ppm/atm according to Ref. [44], which corresponds to the slope of  $0.83(10)$  of Fig. 2.4. Using this relation,  $0.83$  corresponds to  $33$  ppm on Ps-HFS, the y-intercept of  $0.140(72)$  corresponds to  $5.6 \pm 2.9$  ppm on Ps-HFS. This causes underestimation of the material effect and Ps-HFS is estimated to be  $5.6 \pm 2.9$  ppm larger than the previous experimental value. The uncertainty of  $\sigma_m$  in nitrogen gas is large, which results in 2–10 ppm underestimation of Ps-HFS. Although this estimation of the material effect is rough, the underestimation is large enough and suitable to solve the  $15 \pm 4$  ppm discrepancy between the previous experimental average and the theoretical calculation.

## 2.2 New methods

In order to reduce these possible systematic uncertainties in all previous measurements, the following three totally new methods are used in this experiment.

### 2.2.1 Large bore superconducting magnet

1. A large bore superconducting magnet is used to apply a static magnetic field of  $B \approx 0.866$  T. A bore diameter of the magnet is 800 mm, and its length is 2 m. With compensation coils surrounding the RF cavity, the apparatus achieves 1.5 ppm RMS in uniformity of the magnetic field in the large volume of cylinder 40 mm in diameter and 100 mm long, where Ps are formed.
2. The superconducting magnet is operated in persistent current mode and

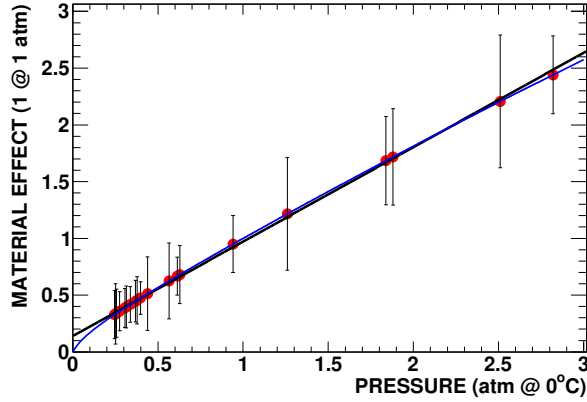


Figure 2.4: Estimation of the non-thermalized Ps effect on Ps-HFS in nitrogen gas with an initial kinetic energy of 2 eV and temperature of 273.15 K. The vertical axis is normalized to unity at 1 atm. The red points with error bars are the toy data, the blue line is the same calculation as Fig. 2.3, and the black line is a linear-fit of the toy data.

a stability of the magnetic field is obtained to be better than  $\pm 1$  ppm.

### 2.2.2 Timing information

1. The timing information between Ps formation and decay is newly obtained in this experiment to investigate the non-thermalized Ps effect.
2. The signal-to-noise ratio of the measurement is significantly improved by a factor of 20, since prompt annihilations and p-Ps can be removed using time information. Figure 2.5 shows the time evolution of  $S_{2\gamma}$  calculated by Eq. (1.26).  $2\gamma$  annihilation probabilities are compared with and without RF. Figure 2.6 shows the difference of  $2\gamma$  annihilation rate between RF-ON and RF-OFF of Fig. 2.5, which corresponds to the  $2\gamma$  transition rate. It is clearly shown that application of a timing window using timing information is a very effective event selection. Figure 2.7 shows the  $S_{2\gamma}$  integrated between  $t = 0$  and  $\infty$  as a function of a static magnetic field strength. It corresponds to measurements without timing information. It is shown that a very large background exists under the transition curve at 0.83 T. On the other hand, Fig. 2.8 shows the  $S_{2\gamma}$  integrated between  $t = 35$  and 155 nsec as a function of a static magnetic field strength. The background is shown to become much smaller with the timing window. The timing information enables an effective selection of the Zeeman transition signal, which much enhances the signal-to-noise ratio of the measurement.

### 2.2.3 High performance $\gamma$ ray detectors

1. LaBr<sub>3</sub>(Ce) scintillators are used to detect  $\gamma$  rays. The energy resolution is 8% FWHM at 511 keV and the decay constant is as short as 16 ns. The

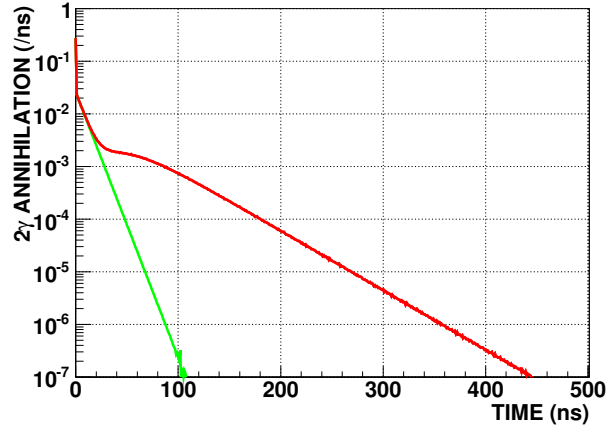


Figure 2.5: Time evolution of the  $2\gamma$  annihilation rate ( $S_{2\gamma}$ ). The red line is a calculation at  $B_{\text{RF}} = 14.2$  G (RF-ON) and the green line is a calculation at  $B_{\text{RF}} = 0$  (RF-OFF).

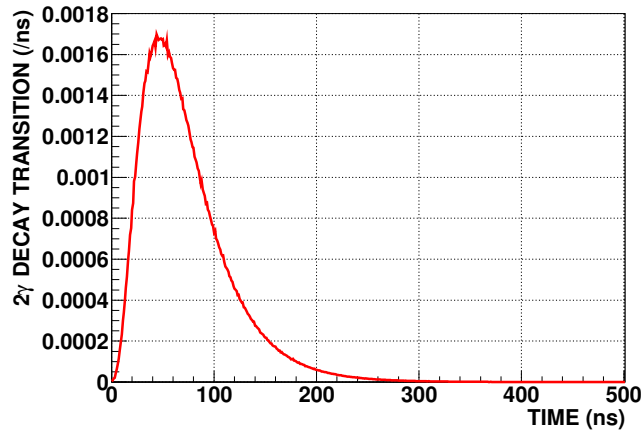


Figure 2.6: Time evolution of the  $2\gamma$  transition rate.

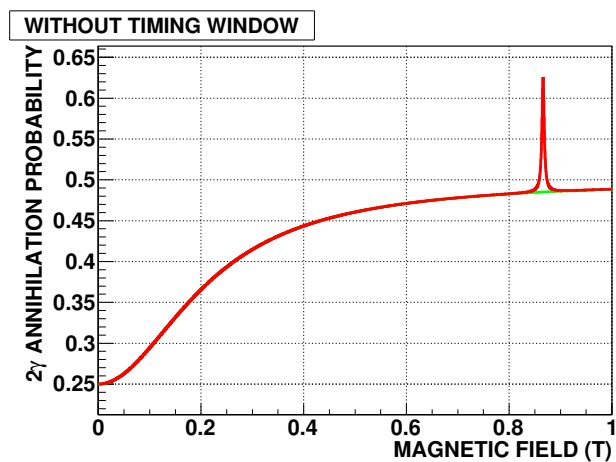


Figure 2.7:  $2\gamma$  decay rate without timing information. The red line is a calculation at  $B_{\text{RF}} = 14.2$  G (RF-ON) and the green line is a calculation at  $B_{\text{RF}} = 0$  (RF-OFF).

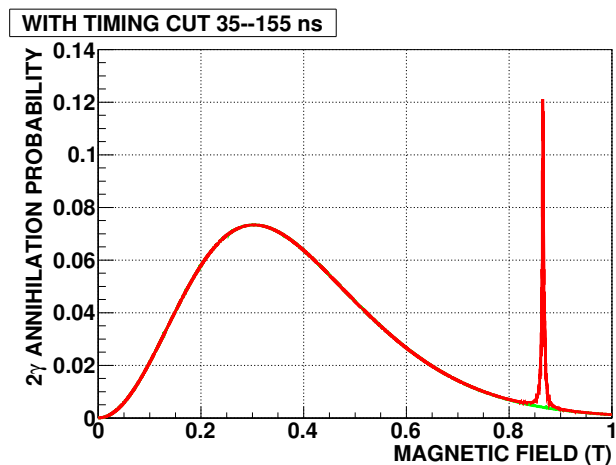


Figure 2.8:  $2\gamma$  decay rate with a timing window of 35–155 ns. The red line is a calculation at  $B_{\text{RF}} = 14.2$  G (RF-ON) and the green line is a calculation at  $B_{\text{RF}} = 0$  (RF-OFF).

acceptance of the setup is greatly increased by the good energy resolution, since  $2\gamma$  events are efficiently separated from  $3\gamma$  events by energy information alone, instead of a back-to-back geometry selection.

2. The fast response of  $\text{LaBr}_3(\text{Ce})$  enables measurement with a strong radioactive source. A  $^{22}\text{Na}$  source of 1 MBq is used for this experiment since individual events from individual positrons have to be distinguished.

## Chapter 3

# Experimental Setup

In this chapter, details of our experimental apparatus are described. An overview of the whole setup is explained at first, and then details of individual components are described.

### 3.1 Overview of the apparatus

Figure 3.1 shows the whole system of our experimental setup. An RF cavity is located at the center of the magnet, and  $\gamma$  ray detectors are surrounding it. High power RF is guided through the waveguide into the cavity. Figure 3.2 shows the enlarged top view in the large bore superconducting magnet. All of these measurement systems are located in the static magnetic field. Figure 3.3 is photographs of the apparatus around and inside the magnet. The static magnetic field is little disturbed by the apparatus because all systems except for PMTs located in the magnet are nonmagnetic. The basic setup is not changed over the whole period of the measurement. Basic procedure is as follows:

1. A positron emits from the positron source.
2. Timing information of the positron emission is obtained by the  $\beta$ -tagging system.
3. The positron enters the RF cavity spiraling around the static magnetic field.
4. The cavity is filled with pure ( $> 99.9\%$ )  $i$ -C<sub>4</sub>H<sub>10</sub> gas. The positron loses its energy colliding with the gas molecules.
5. The slowed positron picks an electron from a gas molecule, and forms positronium with a probability of about 40%.
6. The  $|-\rangle$  state of Ps promptly decays into  $2\gamma$  with a lifetime of about 120 ps. The  $|+\rangle$  state of Ps mostly decays into  $2\gamma$  with a short lifetime of about 8 ns. These two states annihilate soon. On the other hand, the  $|1, \pm 1\rangle$  states of Ps thermalize well in the gas because of its long lifetime.
7. RF makes transitions occur from the  $|1, \pm 1\rangle$  to the  $|0, 0\rangle$  state of Ps when a microwave field is applied in the RF cavity to observe the Zeeman transition.

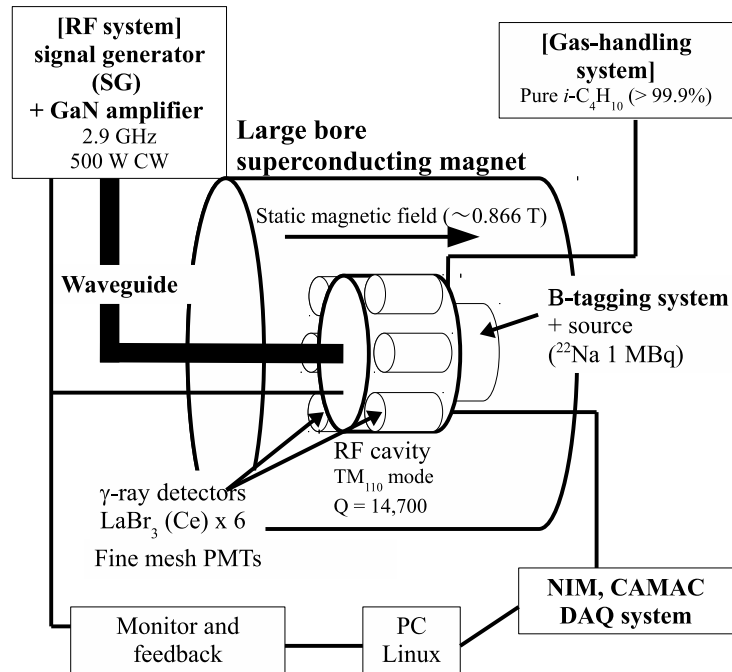


Figure 3.1: Whole system of our experimental setup.

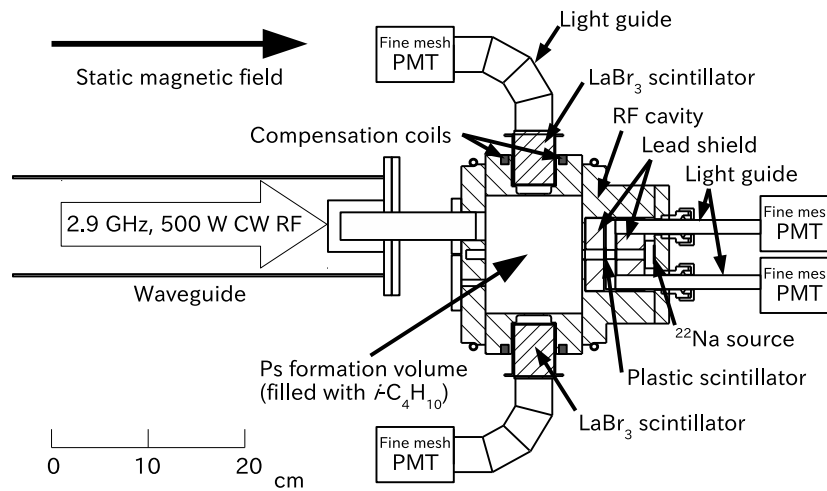
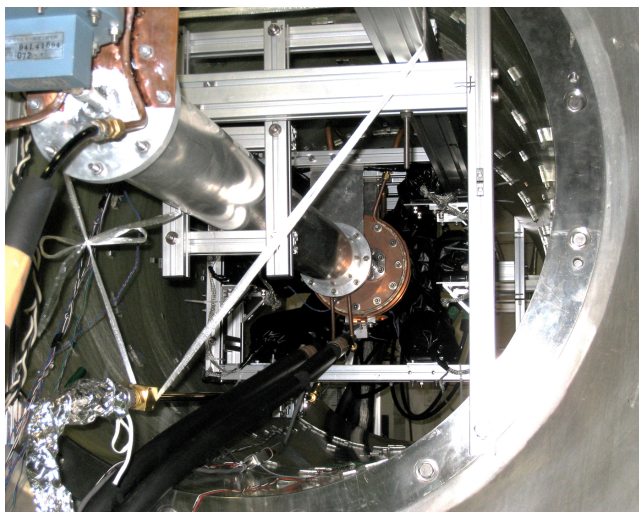


Figure 3.2: Top view in the magnet. (Reproduced from Ref. [1])



(a) Large bore superconducting magnet.



(b) Setup inside the magnet. A  $\beta$ -tagging system is located off-side of the cavity, although it cannot be seen in the photograph. Microwaves are guided from this side to the cavity through the waveguide.

Figure 3.3: Photographs of the experimental setup around the magnet.

8. A transited Ps decays into  $2\gamma$  immediately and a not transited Ps decays into  $3\gamma$ .
9.  $\gamma$ -rays from a Ps decay are detected by  $\gamma$  ray detectors. The Zeeman transition is measured by the change of  $2\gamma$ - and  $3\gamma$ - decay rates at various magnetic field strengths with fixed RF frequency and power.  $\Delta_{\text{HFS}}$  is obtained by fitting data points with theoretical resonance lines.

Each part of the experimental apparatus is explained in the following sections.

### 3.2 Static magnetic field

A static magnetic field to cause the Zeeman splitting is produced by a large bore superconducting magnet (Fig. 3.3(a)). There are two benefits from using it.

- The magnet is developed for MRI and located at KEK Cryogenics Science Center. A bore diameter of the magnet is 800 mm, and its length is 2,000 mm. With compensation coils surrounding the RF cavity, a static magnetic field with a uniformity of 1.5 ppm RMS is successfully applied to a large Ps formation volume of  $O(100 \text{ cm}^3)$  (cylindrical region  $\sqrt{x^2 + y^2} < 20 \text{ mm}$  where Ps are formed). This suppresses a possible systematic uncertainty from the inhomogeneity of the static magnetic field. Figure 3.4 shows the magnetic field distribution in the RF cavity without compensation coils. We found the difference larger than 20 ppm without compensation coils. Figures 3.5 and 3.6 show the magnetic field distribution with compensation coils before and after the Ps-HFS measurement, respectively. The distribution is stable within ppm. The distribution is measured using a proton NMR magnetometer (ECHO Electronics EFM-150HM-AX) with a clock synthesizer (NF Corporation CK1615 PA-001-0312) at 310 points at 10-mm intervals in the region ( $\sqrt{x^2 + y^2} \leq 50 \text{ mm}$ ,  $-35 \text{ mm} \leq z \leq 50 \text{ mm}$ ). Measured magnetic fields are well fitted by the following empirical function  $B(x, y, z)$ :

$$\begin{aligned}
 B(x, y, z) &= \frac{w_x B_x + w_y B_y + w_{zx} B_{zx} + w_{zy} B_{zy}}{w_x + w_y + w_{zx} + w_{zy}}, & (3.1) \\
 B_x &= f_x(z) + g_x(z)r_0^2, \\
 B_y &= f_y(z) + g_y(z)r_0^2, \\
 B_{zx} &= f_{zx}(x') + h_{zx}(x')(z - z_{x0}) + g_{zx}(x')(z - z_{x0})^3, \\
 B_{zy} &= f_{zy}(y') + h_{zy}(y')(z - z_{y0}) + g_{zy}(y')(z - z_{y0})^3, \\
 w_x &= 0.5 \cos^2 \theta, \\
 w_y &= 0.5a \sin^2 \theta, \\
 w_{zx} &= 0.5b \cos^2 \theta, \\
 w_{zy} &= 0.5c \sin^2 \theta, \\
 x' &= x_0 + |r_0 / \cos \theta| \cos \theta, \\
 y' &= y_0 + |r_0 / \sin \theta| \sin \theta, \\
 x_0 &= f_{Cx}(z), \\
 y_0 &= f_{Cy}(z),
 \end{aligned}$$

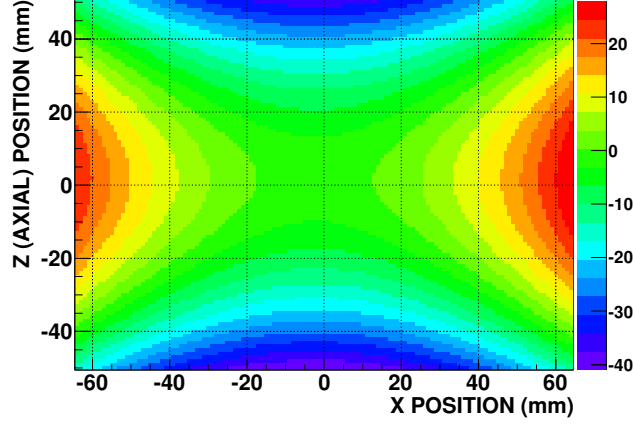


Figure 3.4: Static magnetic field distribution without compensation magnet at  $y = 0$  plane (a horizontal plane at the center of the cavity). The colors indicate differences from the average value in ppm.

$$\begin{aligned}
 z_{x0} &= f_{Czx}(x'), \\
 z_{y0} &= f_{Czy}(y'), \\
 r_0 &= \sqrt{(x - x_0)^2 + (y - y_0)^2}, \\
 \theta &= \tan^{-1}((y - y_0)/(x - x_0)),
 \end{aligned}$$

where  $f_{Cx}(z)$ ,  $f_{Cy}(z)$ ,  $f_{Czx}(x')$ ,  $f_{Czy}(y')$ ,  $f_x(z)$ ,  $f_y(z)$ ,  $f_{zx}(x')$ ,  $f_{zy}(y')$ ,  $g_x(z)$ ,  $g_y(z)$ ,  $g_{zx}(x')$ ,  $g_{zy}(y')$ ,  $h_{zx}(x')$ , and  $h_{zy}(y')$  are 5th-, 3rd-, 3rd-, 2nd-, 5th-, 3rd-, 3rd-, 2nd-, 5th-, 3rd-, 3rd-, 2nd-, 3rd-, and 2nd-order polynomial functions respectively,  $a$ ,  $b$ , and  $c$  are constants. Figures 3.5 and 3.6 show extra- or inter-polated map with this function.

- The magnet is operated in persistent current mode. Fig. 3.7 shows that the stability of the magnetic field is better than  $\pm 1$  ppm. The resonance curve of the NMR probe is monitored during the run. The magnetic field strength is obtained by a probing output from which the difference of the current input clock frequency from the resonant frequency of NMR is provided as a voltage.

Static magnetic fields in the range of 0.85–0.88 T are applied with this magnet and the Zeeman transition lines are measured.

### 3.3 Positron source and $\beta$ -tagging system

The positron source is 1 MBq of  $^{22}\text{Na}$  (Eckert & Ziegler POSN-22). Figure 3.8 shows the decay scheme of  $^{22}\text{Na}$ , and decay radiation are summarized in Table 3.1.

Figure 3.9 shows a photograph of the  $\beta$ -tagging system around the  $^{22}\text{Na}$  source. The system is located at the lid of the RF cavity. The  $^{22}\text{Na}$  source is located at the center, and the emitted positrons are tagged by a thin (0.2 mm

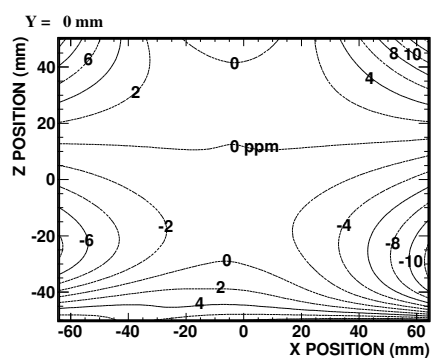
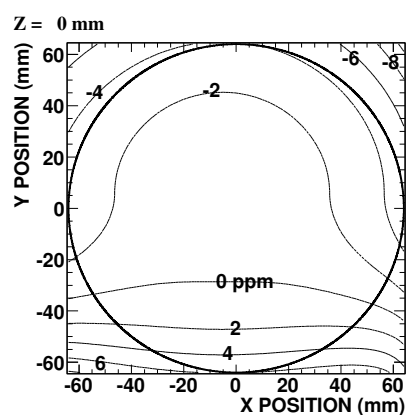
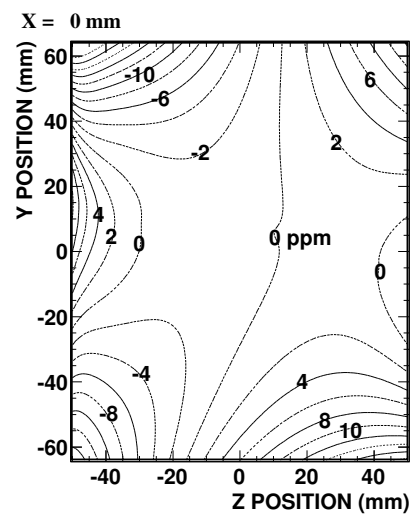
(a)  $y = 0$  plane.(b)  $z = 0$  plane.(c)  $x = 0$  plane.

Figure 3.5: Static magnetic field distribution with compensation magnet (before Ps-HFS measurement). The contours indicate differences from the average value.

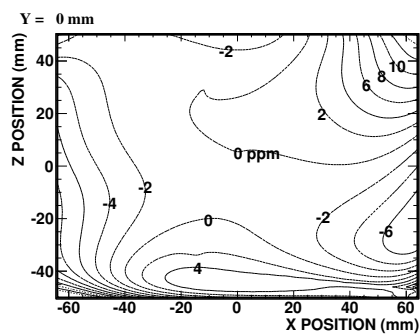
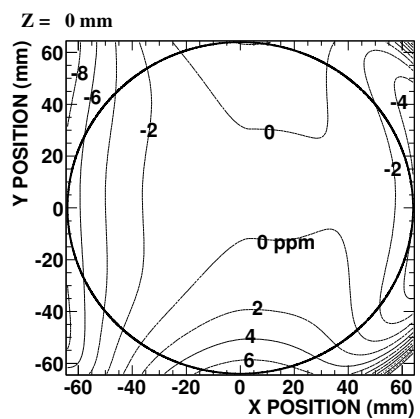
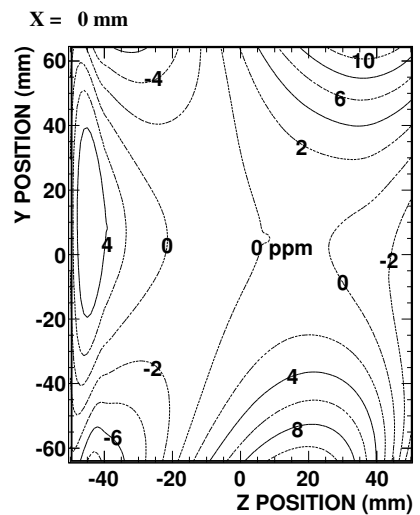
(a)  $y = 0$  plane.(b)  $z = 0$  plane.(c)  $x = 0$  plane.

Figure 3.6: Static magnetic field distribution with compensation magnet (after Ps-HFS measurement). The contours indicate differences from the average value.

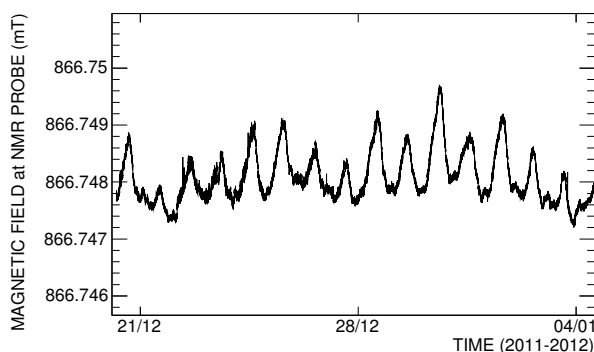


Figure 3.7: Time fluctuation of the static magnetic field. The magnetic field strength on 2011/12/20–2012/01/04 (for more than 2 weeks) is shown.

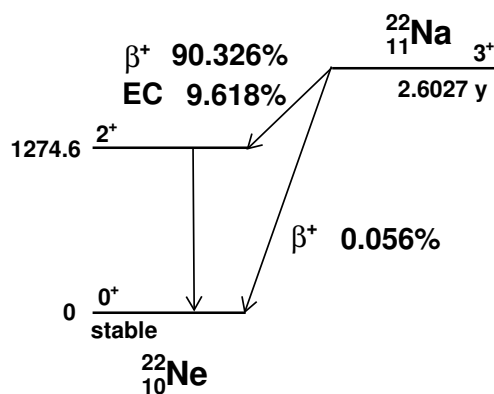


Figure 3.8: Decay scheme of  $^{22}\text{Na}$  [62]

Table 3.1: Decay radiation of  $^{22}\text{Na}$  [62]

Decay mode	Particle	Energy (keV)	Intensity (%)	
$\beta^+$	$e^+$	endpoint 545.7(4)	215.54(21)	90.326(15)
	$e^+$	endpoint 1820.3(4)	835.00(23)	0.056(14)
	$e^-$	Auger (K)	0.82	8.74(3)
	$e^-$	X ray ( $K_{\alpha 2}$ )	0.848	0.053(5)
	$e^-$	X ray ( $K_{\alpha 1}$ )	0.849	0.107(11)
	$\gamma$	1274.537(7)	99.941(14)	

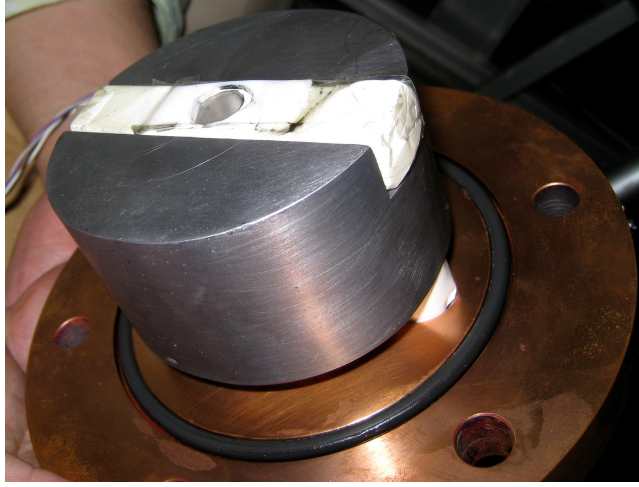


Figure 3.9:  $\beta$ -tagging system.

thick) plastic scintillator (PS). Scintillation light is guided through fused quartz light guides to fine mesh PMTs. Details of each component are described in the following subsections.

### 3.3.1 Source holder

A source holder is fabricated with Copper and it is nonmagnetic. It holds the source and the light guides. The holder itself is screwed to the lid of the RF cavity.

### 3.3.2 Plastic scintillator and fused quartz light guide

A fused quartz light guide (10 mm thick, 15 mm wide and 75 mm long) with a hole 10 mm in diameter at the center is locked by a groove of the source holder. The source is sandwiched by two Ti foils 0.0127 mm thick in order to be suitable for using in vacuum. The active diameter is 9.53 mm, and the outside of the active region is sandwiched by two Ti plates 0.254 mm thick and 19.1 mm in outer diameter. The hole of light guide is covered by a plastic scintillator (NE102A) 12 mm in diameter and 0.1 mm thick. Positrons emitted from the source spiraling pass through the hole of the Teflon plate, the hole of light guide, and the plastic scintillator. The plastic scintillator emits scintillation light when a positron passes. The scintillation light is guided through light guide and two cylinder quartz light guides 200 mm long and 15 mm in diameter glued to the both side of light guide, and then reaches two fine mesh PMTs.

### 3.3.3 Fine mesh PMTs

Two fine mesh PMTs (HAMAMATSU H6614-70MOD) are used to detect scintillation light from the plastic scintillator. Fine mesh PMTs are used because they are located in a static magnetic field. The measured resolutions and gain of fine mesh PMTs gets worse in a static magnetic field depending on the polar

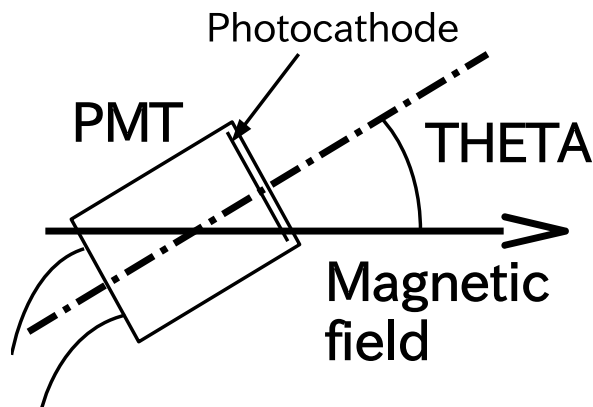


Figure 3.10: Polar angle ‘THETA’ to the magnetic field.

angle to the field shown in Figs. 3.11, 3.12, 3.13. The polar angle “THETA” is defined in Fig. 3.10. The gain is the highest at  $30^\circ$ , but resolutions are the highest at  $0^\circ$ . These data are obtained using the same magnet used in the Ps-HFS measurement with a static magnetic field of 0.866 T. 511 keV back-to-back  $\gamma$  rays are detected with two of fine mesh PMTs (HAMAMATSU H8409-70 (1.5",  $\times 2$ ), HAMAMATSU H6614-70 (2.0",  $\times 1$ )) located back-to-back and  $\text{LaBr}_3(\text{Ce})$  scintillators (Saint-Gobain BrillanCe<sup>TM</sup> 380 of cylinder 25.4 mm in diameter and 25.4 mm long) attached. Details of  $\text{LaBr}_3(\text{Ce})$  scintillators are described in Sec. 3.6.1. Gains of all PMTs became the highest at  $30^\circ$ , because the effective area of the dynodes is the highest at  $30^\circ$  for electrons gained and spiraling go to the anode. On the other hand, the best resolutions of energy and timing are obtained at  $0^\circ$ , because the probability of photoelectrons reaching the first dynode is the highest when PMTs are parallel to the field.

Fine mesh PMTs are located parallel to the magnetic field in the Ps-HFS measurement to obtain the highest energy and timing resolutions. PMTs affect the static magnetic field by 10 ppm with a distance of 10 cm, and 100 ppm with a distance of a few cm, because magnetic material of Kovar, which is an alloy mainly of Fe, Ni, and Co, is used in fine mesh PMTs. This effect is about +3 ppm and effect on the uniformity is negligible in the Ps-HFS measurement since the PMTs are located 15 cm away from the RF cavity.

### 3.4 RF system

Figure 3.14 shows the RF circuit of the apparatus. RF circuit consists of RF supply, a monitor, feedback, and an interlock.

#### 3.4.1 RF supply

RF supply system consists of a signal generator (SG), an amplifier (AMP), waveguides, feedthroughs, and the RF cavity.

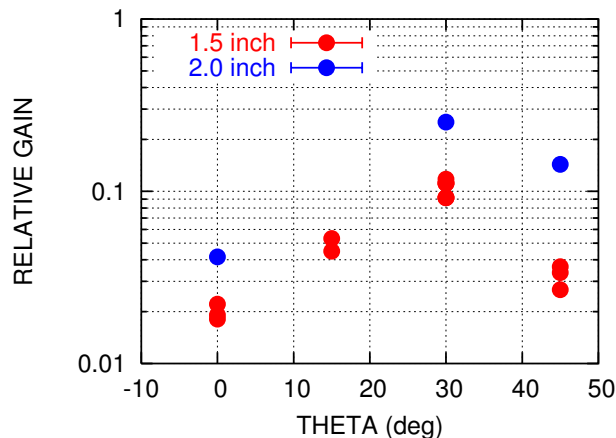


Figure 3.11: Polar angle dependence of the gain of fine mesh PMTs in a magnetic field. The definition of the angle is shown in Fig. 3.10. The gain is shown by the ratio compared to the gain without any magnetic field. The red points are values of a 1.5" PMT, and the blue points are that of a 2" PMT. Error bars are smaller than markers.

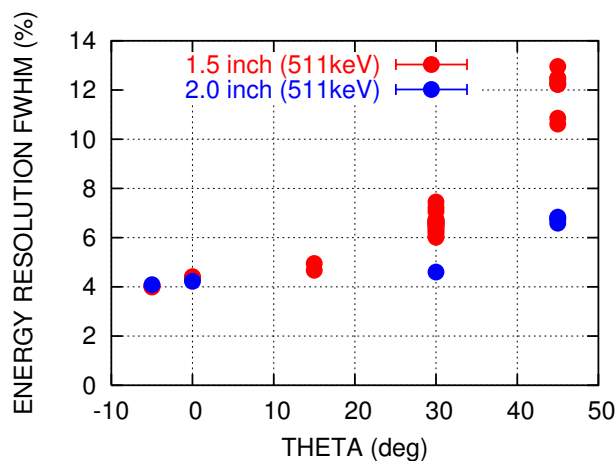


Figure 3.12: Polar angle dependence of the energy resolution of fine mesh PMTs in a magnetic field. The definition of the angle is shown in Fig. 3.10. The resolution is shown by FWHM at 511 keV. The red points are values of a 1.5" PMT, and the blue points are that of a 2" PMT. The resolution without any magnetic field is shown at  $-5^\circ$ .

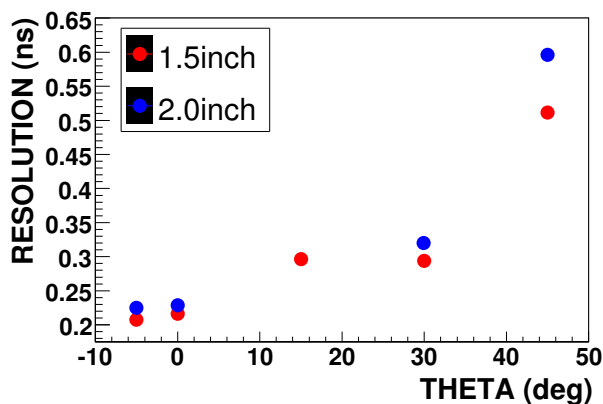


Figure 3.13: Polar angle dependence of the timing resolution of fine mesh PMTs in a magnetic field. The definition of the angle is shown in Fig. 3.10. The resolution is shown by FWHM at 511 keV. The red points are values of a 1.5" PMT, and the blue points are that of a 2" PMT. The resolution without any magnetic field is shown at  $-5^\circ$ .

### Signal generator and amplifier

Continuous microwaves of about 6.6 dBm are generated by a SG (ROHDE & SCHWARZ SMV 03). SG is controlled via GPIB interface. The frequency of microwaves is monitored with a precision of better than 0.1 ppm. An AMP (R&K A2856BW200-5057-R) amplifies the microwaves from SG by 50 dB, and outputs continuous microwaves of about 500 W. Interlock system is installed for the safety. New GaN semiconductors are used in AMP. GaN semiconductors have an energy gap of 3.3 eV, which is about 3 times larger than conventional Si semiconductors then the low background level is expected. It has also higher insulation resistance, lower ON resistance, lower energy loss, even it is used at high voltage and high current, and extremely higher switching speed than those of conventional semiconductors. GaN semiconductors are expected to be a high-power devices of new generation because of these good properties.

### Waveguides, feedthroughs, and the RF cavity

High power microwaves generated by the RF supply system are guided through waveguides fabricated with Al. An input feedthrough is an alumina ceramic cylinder 30 mm in diameter and 140 mm long, in which high power microwaves pass through into the RF cavity. The input feedthrough is specially designed to avoid gas discharges at low gas density. Fig. 3.15 shows the RF power at discharge as a function of gas pressure (measured at  $\approx 25^\circ\text{C}$ ). Even at 0.25 atm, we could apply 500 W RF. RF power of the runs was chosen slightly below the limit line (see Appendix A). The coupling of the input feedthrough is carefully tuned to  $\sim 1$ . On the other hand, an output feedthrough used for monitoring power is a spherical antenna whose coupling is very low.

Figure 3.16 is a photograph of the RF cavity. The RF cavity is made with oxygen-free copper; the inside of the cavity is a cylinder 128 mm in diameter

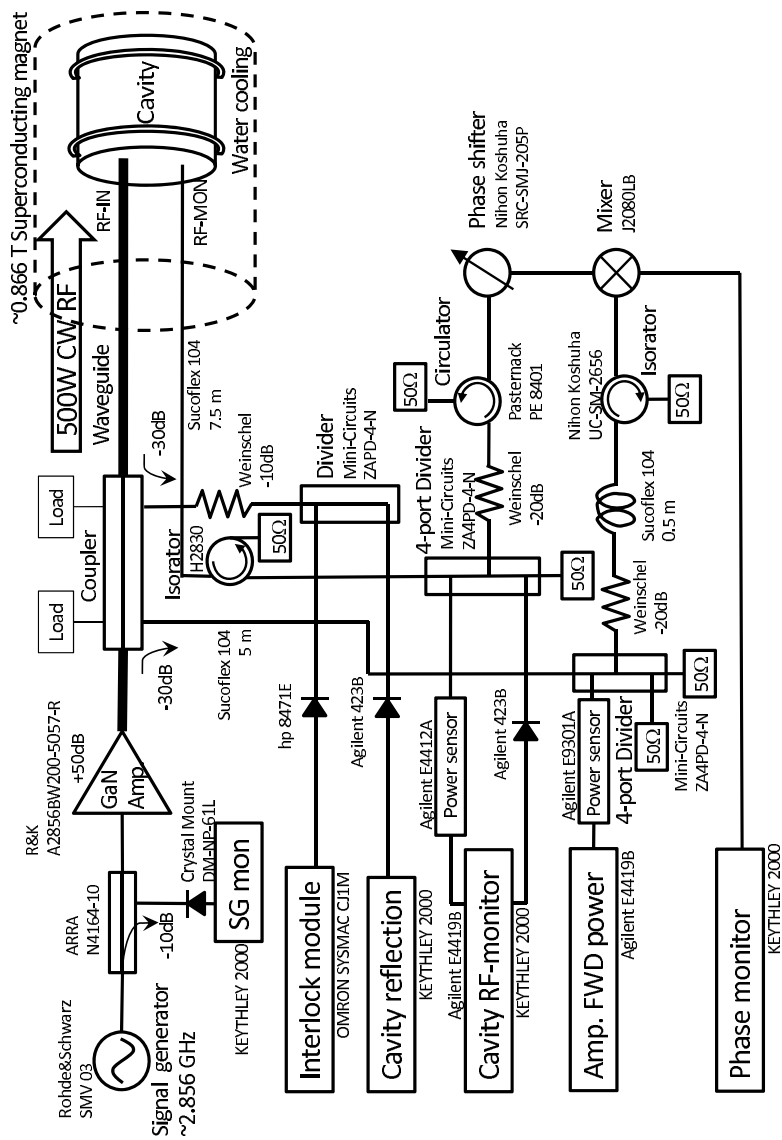


Figure 3.14: RF circuit.

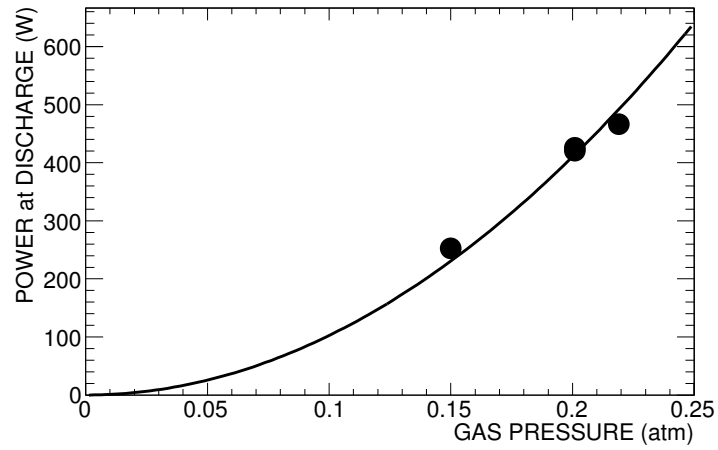


Figure 3.15: RF power at discharge as a function of gas pressure. The line indicates a fit with a simple assumption that the power is proportional to square of the gas pressure.

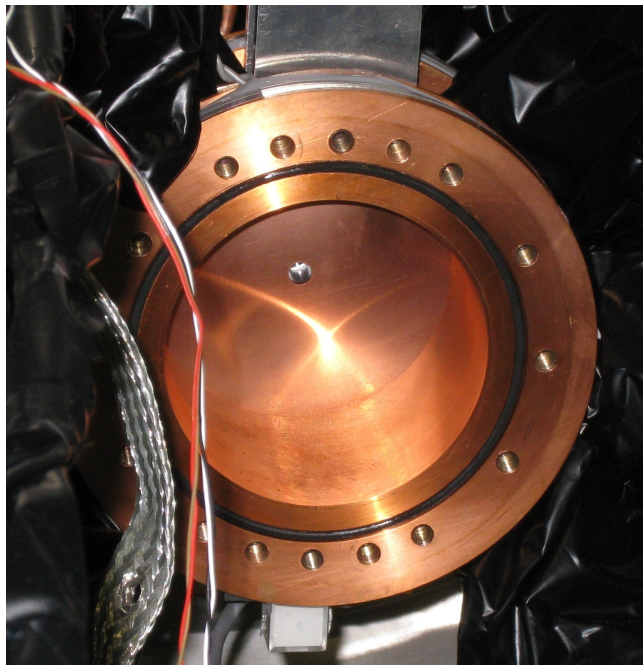


Figure 3.16: Photograph of the RF cavity.

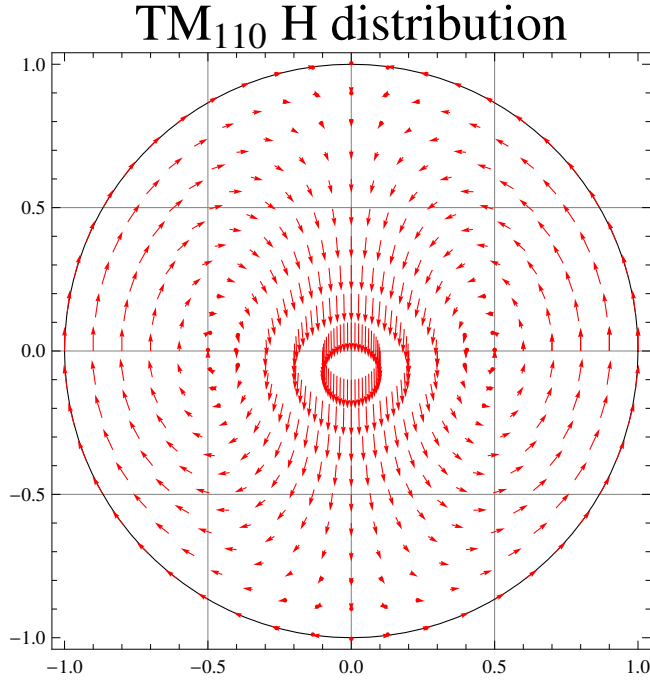


Figure 3.17: Magnetic field of the  $\text{TM}_{110}$  mode. The length of the arrows show the strength of the field, and the direction of the field is shown by the direction of the arrows.

and 100 mm long. The  $\gamma$  rays pass through the side wall of the cavity efficiently, because its thickness is only 1.5 mm. The cavity is operated in the  $\text{TM}_{110}$  mode with a resonant frequency of 2.856 6 GHz and a loaded quality factor  $Q_L$  of 14,700. Figure 3.17 shows the cross sectional view of the RF magnetic field of the  $\text{TM}_{110}$  mode. The RF magnetic field is the two counter-rotating swirls and the maximum at the center. The  $\text{TM}_{110}$  mode is selected since the Zeeman transition is caused by the oscillating magnetic field perpendicular to the static magnetic field, which is longitudinal to the axis of the RF cavity. The diameter is determined by the wavelength of microwaves, and the length is determined to avoid interferences with other modes. The intrinsic resonant frequency  $f_0$  of  $\text{TM}_{110}$  mode cavity is described as

$$f_0 = \frac{cJ_{11}}{2\pi a}, \quad (3.2)$$

where  $c$  is the speed of light,  $J_{11}$  is the first zero of Bessel function of order 1, and  $a$  is the radius of the cavity. Ohmic loss at the cavity produces heat when microwaves are supplied. The heat is removed by constant temperature (typically 25 °C is used) water in order to avoid changes of the properties of the cavity. The water passes through cooling pipes silver brazed to the cavity and the temperature is controlled by a chiller.

### 3.4.2 Monitor

The RF system are RF frequency, SG output power, cavity input power, cavity transmitted power, cavity reflection power, and the phase shift between input and transmitted RF of the cavity are monitored as follows.

#### RF frequency

RF frequency is monitored by the setting value itself of the SG. The monitoring precision is better than 0.1 ppm. The absolute accuracy is 0.6 ppm, which is calculated using an aging of 0.1 ppm/year.

#### SG output power

The output RF from the SG is picked using a directional coupler (ARRA N4164-10) for monitoring. This power is measured by a crystal detector (Nihon Koshuha DM-NP-61L). A crystal detector is a device which converts an RF input to a voltage output using a commutator. The characteristic of the output voltage depends on the input power. The output voltage is nearly linearly proportional to the input power in the range of  $-40$ – $0$  dBm input power. The output voltage non-linearity is calibrated by fitting the output-input curve by a 5th order polynomial. The output of the crystal detector is digitised by a digital multimeter (DMM, KEITHLEY 2000), and recorded through a GPIB interface.

#### Cavity input power

The cavity input power is picked (by an amount of  $-30$  dB) using a directional coupler located between GaN AMP and the cavity. The picked power is measured by a power sensor (Agilent E9301A) read by a power meter (Agilent E4419B). The output of the directional coupler is carried by a 5 m SUCOFLEX (SF) 104 cable and divided to 4 outputs by a divider. One of the output is used for measuring power, another output is used for measuring the phase shift, and the other outputs are terminated by  $50\ \Omega$  resistor. The measured value is displayed at the power meter, and recorded via a GPIB interface.

#### Cavity transmitted power

The transmitted RF from the antenna attached to the cavity is carried via 7.5 m SF 104 cable, let through an isolator (TMT H2830), and divided by 4 with a divider. One of the outputs is  $-6$  dB attenuated (Lucas Weinschel) and used to measure the power using a crystal detector (Agilent 423B), another output is also used to measure the power but using a power sensor (Agilent E4412A) read by the same power meter as used for the input power, another output is used to measure the phase shift, and the other output is  $50\ \Omega$  terminated. The voltage of the crystal detector is read by the DMM and recorded via the GPIB interface, and the measured power of power meter is also recorded via the GPIB interface.

#### Cavity reflected power

The power of the RF reflected at the cavity is picked by an amount of  $-30$  dB using the same directional coupler as that used for picking the cavity input

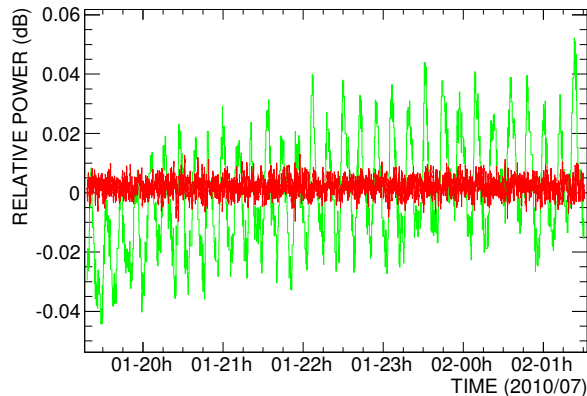


Figure 3.18: Relative power as a function of time. The red line indicates the AMP output power, and the green line indicates the SG output power using feedback.

power. It is  $-10$  dB attenuated (Lucas Weinschel) and divided by 2 with a divider. One of the outputs is measured by a crystal detector (Hewlett-Packard 8471E) used for the interlock system, and the other output is measured by another crystal detector (Agilent 423B) for monitoring. The measured power by 423B is recorded as the same way as for the SG output power.

#### Phase shift between input and transmitted RF of the cavity

One of the outputs of the divided cavity input power and one of the outputs of the divided cavity transmitted power are used to measure the phase shift for feedback. The output of the divider of the cavity input RF is  $-20$  dB attenuated (Lucas Weinschel), delayed by 0.5 m SF 104 cable, isolated by an isolator (Nihon Koshuha), and let into a mixer (J2080LB). On the other hand, the output of the divider of the cavity transmitted RF is  $-20$  dB attenuated (Lucas Weinschel), isolated by a circulator (PASTERNAK PE8401), let through a phase shifter (Nihon Koshuha SRC-SMJ-205P), and let into the mixer. The output of the mixer is measured by the DMM.

#### 3.4.3 Feedback

The feedback system consists of power feedback and frequency feedback.

##### Power feedback

The RF power has to be stabilized within 0.3% to measure Ps-HFS with an accuracy of  $O(\text{ppm})$ . The AMP output RF power is stabilized by changing SG output power. Feedback is performed using the measured power of the cavity input RF. Figure 3.18 shows that the AMP output power is stabilized by the power feedback system which tunes the SG output power. As shown in this figure, power is stabilized. Figure 3.19 shows the measured distribution of relative RF power of typical run. It is clear that the power is well stabilized

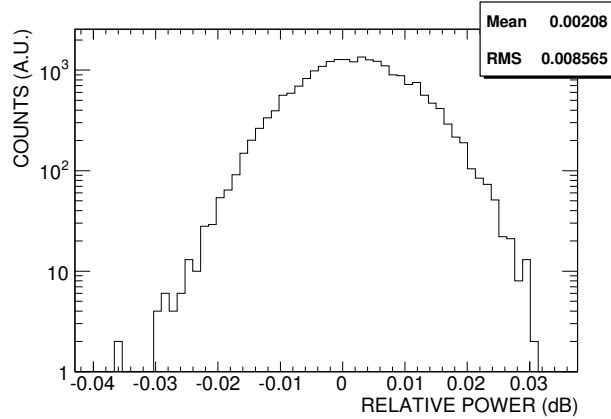


Figure 3.19: Distribution of AMP output power. The horizontal axis shows the relative value (dB) to a standard power.

within 0.2% fluctuation. Although it is well stabilized, the power can change by changing the RF setup or change of an air temperature. This can be corrected in analysis process if the cavity input power is measured at enough relative precision. Detail of analysis is described in Chap. 4.

### Frequency feedback

The RF frequency ideally should be constant the same as the RF power, but the resonant frequency of the RF cavity always changes by the reason such as temperature. The change of the resonant frequency makes impedance mismatch, which decrease the input power to the cavity and increase the reflection power. The increase of the reflection power is very dangerous for the RF circuit and AMP. The impedance mismatching is avoided by matching the RF frequency of SG output with the cavity resonant frequency. Ps-HFS still can be measured at the required precision without making it constant when the RF frequency is monitored at a suitable, correcting this effect in analysis. The phase shift described in Sec. 3.4.2 corresponds to the difference between SG output RF frequency and the cavity resonant frequency. The frequency matching is performed by changing RF output frequency to make the phase shift zero.

## 3.5 Gas

The RF cavity is filled with pure  $i\text{-C}_4\text{H}_{10}$  gas (Takachiho chemical industrial, > 99.9%). Isobutane gas has the following 4 important roles: 1. stopping positrons in the RF supplied region of the cavity, 2. providing electrons to form Ps, 3. quenching slow positrons which are the positrons with very low energy not enough for forming Ps, 4. thermalizing Ps to the room temperature. Especially the third role is quite important because the remaining slow positrons become a huge experimental background. For example, in the nitrogen gas, which was used in the previous Ps-HFS measurements, at 30 °C and 1 atm, a slow positron decay into  $2\gamma$  with a lifetime of 186 ns, which is similar to that of o-Ps. This

topology is the same as the Zeeman transition signal of “delayed  $2\gamma$  decay”, so that the backgrounds from slow positrons’ decay cannot be removed by analysis. Typical Ps formation fraction of stopped positrons is 20–40% in gases, and all the remaining positrons become slow positrons. The amount of this background is 15–40 times larger than the Zeeman transition signal since the Zeeman transition probability is typically 10%, which results in a few percent of all the stopped positrons, whereas the slow positrons are 60–80% of all the stopped positrons. Details of gas-handling system, the slow positron background, and the pickoff background are described in this section.

### 3.5.1 Gas-handling system

Gas-handling system is constructed by VCRs, KFs, and Swageloks. The diameter of most pipes are 1/2” from the RF cavity to the pumps. A valve is located at the flange of the magnet in order to shut the heat-pumping with experimental hall, but not inside the magnet because valves are magnetic. The pumps are the set of a rotary pump and a turbo molecular pump, which can evacuate the cavity to a vacuum of  $10^{-4}$  Pa. At the beginning of every run, the cavity is evacuated to that vacuum and then filled to 0.129–1.366 amagat<sup>1</sup> of *i*-C<sub>4</sub>H<sub>10</sub>. The whole gas-handling system is baked with 60 °C water for two weeks after every exposure to air. The absolute pressure of the gas is measured by a pressure transmitter (setra MODEL 225) with a 0.1 kPa precision, which is recorded with a portable, high-speed data logger (HIOKI MEMORY HiLOGGER Model 8420-50). The logger is connected to the Linux PC via RS-232C interface and the data are recorded to HDDs. The gauge pressure is also measured by a pressure transmitter (NAGANO KEIKI KM31-574) and a digital display (NAGANO KEIKI GC95-911).

### 3.5.2 Slow positron background

The annihilation rate of slow positron  $\Gamma_{\text{slowpos}}$  is described using a parameter  $Z_{\text{eff}}$  as

$$\Gamma_{\text{slowpos}} \equiv \pi r_0^2 c n Z_{\text{eff}}, \quad (3.3)$$

where  $r_0$  is the classical electron radius,  $c$  is the speed of light in vacuum, and  $n$  is a number density of gas molecules. Letting (N<sub>2</sub>) indicate the amount about nitrogen,  $Z_{\text{eff}}(\text{N}_2) = 29.75 \pm 0.85$  [63] and

$$\Gamma_{\text{slowpos}}(\text{N}_2) = 5.98(17) \times 10^{-3} n(\text{amagat}) \text{ ns}^{-1}, \quad (3.4)$$

where amagat is a unit of number density normalized by that of ideal gas at 0 °C, 1 atm. The lifetime of a slow positron in 1 amagat nitrogen is  $167.3 \pm 4.8$  ns which is similar to that of o-Ps ( $142.04(1)$  ns [3] in vacuum). On the other hand, letting (iso) indicate the amount about isobutane,  $\Gamma_{\text{slowpos}}/n(\text{iso}) = (107.9 \pm 2.1) \times 10^{-12} \text{ cm}^3/\text{s}$  [64] and

$$\Gamma_{\text{slowpos}}(\text{iso}) = 2.899(56) n(\text{amagat}) \text{ ns}^{-1}. \quad (3.5)$$

The lifetime of a slow positron in 1 amagat *i*-C<sub>4</sub>H<sub>10</sub> is  $0.3449 \pm 0.0067$  ns, which is much shorter than that of o-Ps. Even if in 0.1 amagat *i*-C<sub>4</sub>H<sub>10</sub>, it has still short enough lifetime of 3.4 ns.

<sup>1</sup>the amagat unit is the number density normalized to that of an ideal gas at 0 °C , 1 atm.

### 3.5.3 Pickoff background

The pickoff annihilation is another source of backgrounds because the pickoff also has the same topology as the Zeeman transition. The annihilation rate of pickoff  $\Gamma_{\text{pickoff}}$  is described using a parameter  ${}_1Z_{\text{eff}}$  as

$$\Gamma_{\text{pickoff}} \equiv 4\pi r_0^2 c n {}_1Z_{\text{eff}}. \quad (3.6)$$

For nitrogen,  ${}_1Z_{\text{eff}}(\text{N}_2) = 0.260 \pm 0.005$  [65] and

$$\Gamma_{\text{pickoff}}(\text{N}_2) = 2.090(40) \times 10^{-4} n(\text{amagat}) \text{ ns}^{-1}. \quad (3.7)$$

The pickoff annihilation rate in 1 amagat nitrogen is 2.968(57)% of that of o-Ps in vacuum. On the other hand, about *i*-C<sub>4</sub>H<sub>10</sub>,  ${}_1Z_{\text{eff}}(\text{iso}) = 0.729 \pm 0.002$  [65] and

$$\Gamma_{\text{pickoff}}(\text{iso}) = 5.859(16) \times 10^{-4} n(\text{amagat}) \text{ ns}^{-1}. \quad (3.8)$$

The pickoff annihilation rate in 1 amagat *i*-C<sub>4</sub>H<sub>10</sub> is 8.323(23)% of that of o-Ps in vacuum.

## 3.6 Gamma ray detectors

In this section, details of  $\gamma$  ray detectors are described. Six  $\gamma$  ray detectors consist of LaBr<sub>3</sub>(Ce) scintillators, UVT (ultraviolet transmitting) light guides, and fine mesh PMTs are used. Details of LaBr<sub>3</sub>(Ce) scintillators and UVT light guides are described in the following sections. The fine mesh PMT is described in Sec. 3.3.3.

### 3.6.1 LaBr<sub>3</sub>(Ce)

Six cylinder LaBr<sub>3</sub>(Ce) inorganic crystal scintillators (Saint-Gobain BrillanCe™ 380) 38.1 mm in diameter and 50.8 mm long are used. A photograph of scintillators is shown in Fig. 3.20.

#### Properties of LaBr<sub>3</sub>(Ce) scintillator

The properties of LaBr<sub>3</sub>(Ce) are summarized in Table 3.2 [66]. LaBr<sub>3</sub>(Ce) is used because of the following three reasons.

- It has excellent energy resolution (4% FWHM at 511 keV). The acceptance of the setup is greatly increased by the good energy resolution, because  $2\gamma$  events are efficiently separated from  $3\gamma$  events with only energy information instead of a back-to-back geometry selection.
- It has good timing resolution (200 ps FWHM at 511 keV). It is important to timing information at high precision for this experiment. LaBr<sub>3</sub>(Ce) has high enough timing resolution.
- It has a decay constant as short as 16 ns, and no long component. It reduces pileup events, enabling measurements with a high rate.

Figure 3.20:  $\text{LaBr}_3(\text{Ce})$  scintillators.Table 3.2: Properties of  $\text{LaBr}_3(\text{Ce})$  [66]. The properties of  $\text{NaI}(\text{Tl})$  are also listed for comparisons.

	$\text{LaBr}_3(\text{Ce})$	$\text{NaI}(\text{Tl})$
Light yield (photons/keV)	63	38
$1/e$ decay time $\tau$ (ns)	16	250
F. O. M. $\left(\sqrt{\tau/\text{lightyield}}\right)$	0.5	2.6
Wavelength of maximum emission $\lambda_{\text{max}}$ (nm)	380	415
Refractive index at $\lambda_{\text{max}}$	$\sim 1.9$	1.85
Density ( $\text{g}/\text{cm}^3$ )	5.08	3.67
Thickness for 50% attenuation at 662 keV (cm)	1.8	2.5

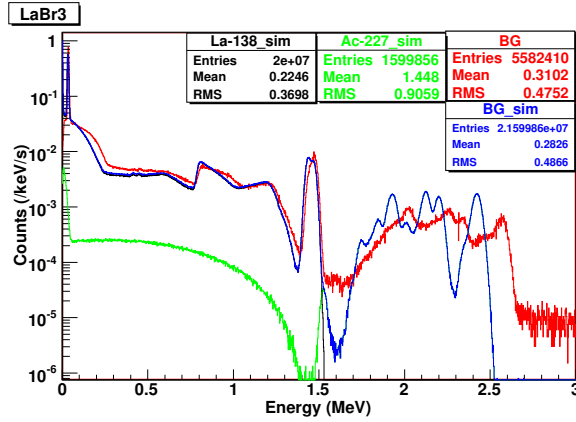


Figure 3.21: Background energy spectra of  $\text{LaBr}_3(\text{Ce})$ . The red line indicates the data, black line is simulated with an isotope  $^{138}\text{La}$ , the green line is a MC simulation of  $^{227}\text{Ac}$ , and the blue line is sum of the black line and the green line.

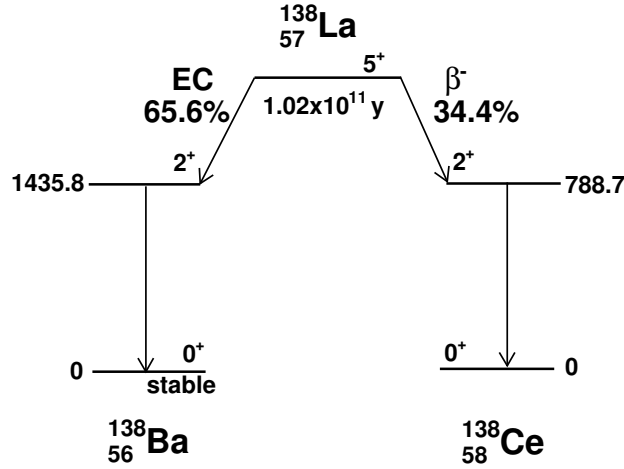
Table 3.3: Decay radiation of  $^{138}\text{La}$  [69].

Decay mode	Particle	Energy (keV)	Intensity (%)
EC	$e^-$	Auger (L)	3.67 49.0(5)
		Auger (K)	26.4 4.16(18)
		Internal Conversion (K)	1398.354(10) 0.0485
	$\gamma$	X ray (L)	4.47 6.1(3)
		X ray ( $K_{\alpha 2}$ )	31.817 10.6(3)
		X ray ( $K_{\alpha 1}$ )	32.194 19.4(5)
		X ray ( $K_{\beta 3}$ )	36.304 1.86(5)
		X ray ( $K_{\beta 1}$ )	36.378 3.59(9)
65.6(5)%		X ray ( $K_{\beta 2}$ )	37.255 1.14(3)
			1435.795(10) 65.6
$\beta^-$	$e^-$	endpoint 255(11)	95.7(41) 34.4(7)
34.4(5)%	$\gamma$		788.742(8) 34.4

### Background of $\text{LaBr}_3(\text{Ce})$

$\text{LaBr}_3(\text{Ce})$  has intrinsic backgrounds because it contains radioisotopes. It contains a natural radioisotope of  $^{138}\text{La}$  (natural abundance of 0.09%) and a contaminant of  $^{227}\text{Ac}$ . Figure 3.21 shows a self-counting energy spectrum of  $\text{LaBr}_3(\text{Ce})$  shielded by 5 cm thick Pb compared with Monte Carlo (MC) simulations of  $^{138}\text{La}$  and  $^{227}\text{Ac}$ . It can be explained by sum of  $^{138}\text{La}$  and  $^{227}\text{Ac}$ . The MC simulations are performed with Geant4 [67, 68] release 4.9.0.p01.

$^{138}\text{La}$  Figure 3.22 shows the decay scheme of  $^{138}\text{La}$ . The radiations and intensity are summarized in Table 3.3. The MC simulation in Fig. 3.21 is

Figure 3.22: Decay scheme of  $^{138}\text{La}$  [69].

normalized by the natural abundance of 0.09%. The background of low energy region can be explained by  $^{138}\text{La}$ .

$^{227}\text{Ac}$  A decay cascade of  $^{227}\text{Ac}$  is the actinium series. The rate of MC simulation in Fig. 3.21 is normalized by the rate of measurement because  $^{227}\text{Ac}$  does not exist naturally but it is just a contamination. The energy deposit of  $\alpha$  particle is multiplied by 0.3 because  $\alpha$  particle deposits its large energy in very short distance and the light yield is not proportional to the energy deposit any more. The factor 0.3 is arbitrary defined. The high energy region of  $\text{LaBr}_3(\text{Ce})$  background can be explained by  $^{227}\text{Ac}$ .

The total background rate is about 100 Hz and the rate is very low in energy range of 350–550 keV which is used for analysis. Furthermore, this background can be subtracted as described in Chap. 4 since these events are accidental.

### 3.6.2 UVT light guide

Six UVT light guides of the same size and shape are used to guide scintillation light of  $\text{LaBr}_3(\text{Ce})$  to fine mesh PMTs. As shown in Fig. 3.23, each light guide consists of 4 parts of cylinder 38.1 mm in diameter and 35 mm long and edges obliquely cut at an angle of  $15^\circ$ , totally 140 mm and bent by  $90^\circ$ . There are tapped holes for light guide holders which ensure pressure joining of a  $\text{LaBr}_3(\text{Ce})$  and a PMT. The UVT light guides are surrounded by a reflector of 0.5 mm thick Gore-tex.

The long,  $90^\circ$  bent, and UVT light guides are used because of the following reasons.

1. The fine mesh PMT disturbs the static magnetic field since it contain magnetic materials as described in Sec. 3.3.3. It must be located as far as possible from the Ps formation volume of the RF cavity.



Figure 3.23: UVT light guide.

2. The light guides must be UVT since the wavelength of maximum emission of  $\text{LaBr}_3(\text{Ce})$  is 380 nm.

Detail reasons to choose the design as shown in Fig. 3.23 are the following properties of light guides. The properties are investigated using a  $\text{LaBr}_3(\text{Ce})$  of cylinder 25.4 mm in diameter and 25.4 mm long and UVT light guides of 38.1 mm in diameter, and a 2" fine mesh PMT. As  $\gamma$  sources,  $^{22}\text{Na}$  (511 keV, 1275 keV),  $^{137}\text{Cs}$  (662 keV), and  $^{60}\text{Co}$  (1173 keV, 1333 keV) are used.

#### Length and angle dependence

Figure 3.24 shows attenuation of light yield as a function of the length of light guides. Firstly, up to 5 cm, the light output rapidly decreases with the length of the light guide. This is because the lights which do not satisfy a total reflection condition are lost. Secondly, in the region of 5–10 cm, the loss related to the total reflection condition becomes smaller and the absorption loss appears to be visible. Finally, at 20 cm, the light output is about a half, but it is not so smaller than that at 10 cm. This indicates that the absorption loss is quite small and the length can be determined arbitrary if the light guide is longer than 10 cm, which is the shortest possible length to avoid PMTs disturbing the static magnetic field. This property does not depend on the absolute light outputs, because it is the same at all  $\gamma$  ray energies.

Figure 3.25 shows the relative light outputs as a function of the bending angle of light guides. Values are normalized with the output of  $\text{LaBr}_3(\text{Ce})$  directly glued to the PMT. The light output is as large as 50% when the light guide is bended by  $90^\circ$ . The bending angle dependence is small so that bending by  $90^\circ$  is reasonable.

#### Light Output of the Final Design

Figure 3.26 shows energy spectra of  $^{22}\text{Na}$  with the UVT light guide and without light guide. A  $\text{LaBr}_3(\text{Ce})$  of a cylinder 38.1 mm in diameter and 50.8 mm long

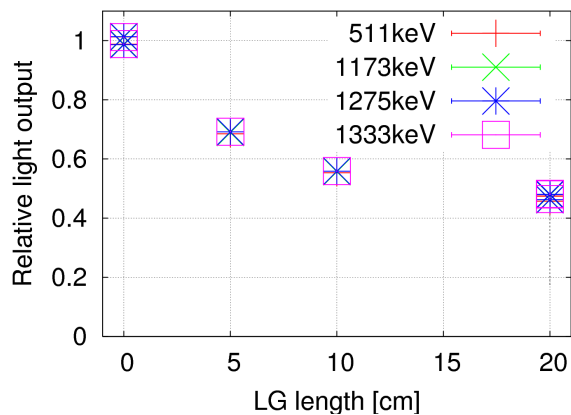


Figure 3.24: Light guide length dependence of light output. 0 cm is the data of  $\text{LaBr}_3(\text{Ce})$  directly glued to the PMT.

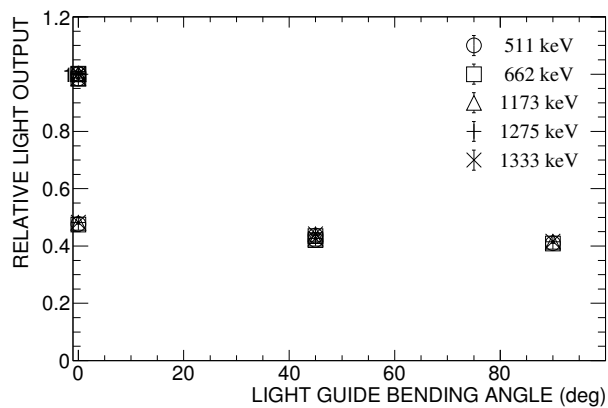


Figure 3.25: Light guide bending angle dependence of light output. The data around (0 deg, 1) are measured with  $\text{LaBr}_3(\text{Ce})$  directly glued to the PMT, and the other data are measured with light guides of 20 cm long.

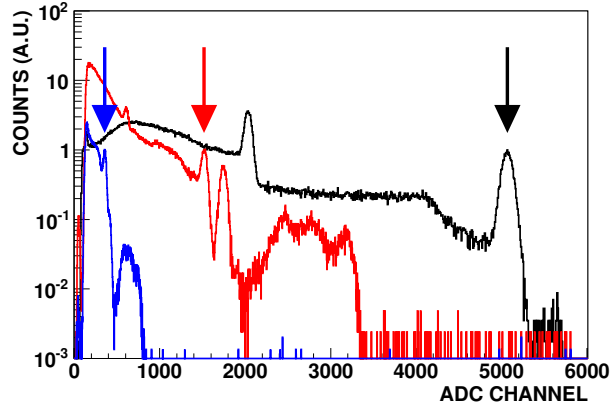


Figure 3.26: Change of light output and energy resolution with light guide. The black line is the data without any light guides, the red line is the data with a UVT light guide, and the blue line is the data with a non-UVT light guide. The gains of the fine mesh PMT are the same and the arrows indicate 1,275 keV.

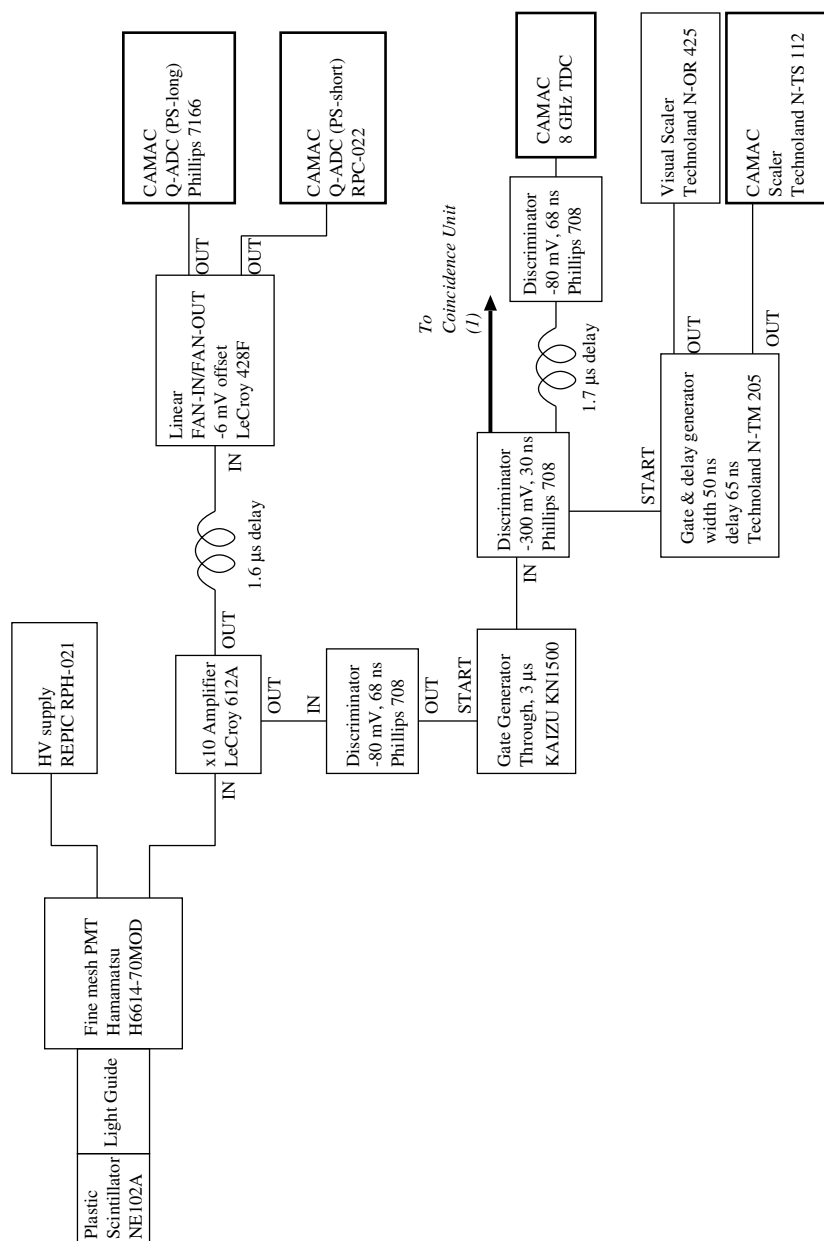
is used. For comparison, energy spectrum with non-UVT light guide is also superimposed (blue line). The light output with UVT light guide is 0.3 of that without any light guides. The energy resolution only depends on photon statistics, and is  $1/\sqrt{0.3}$  with UVT light guide compared to that without any light guides.

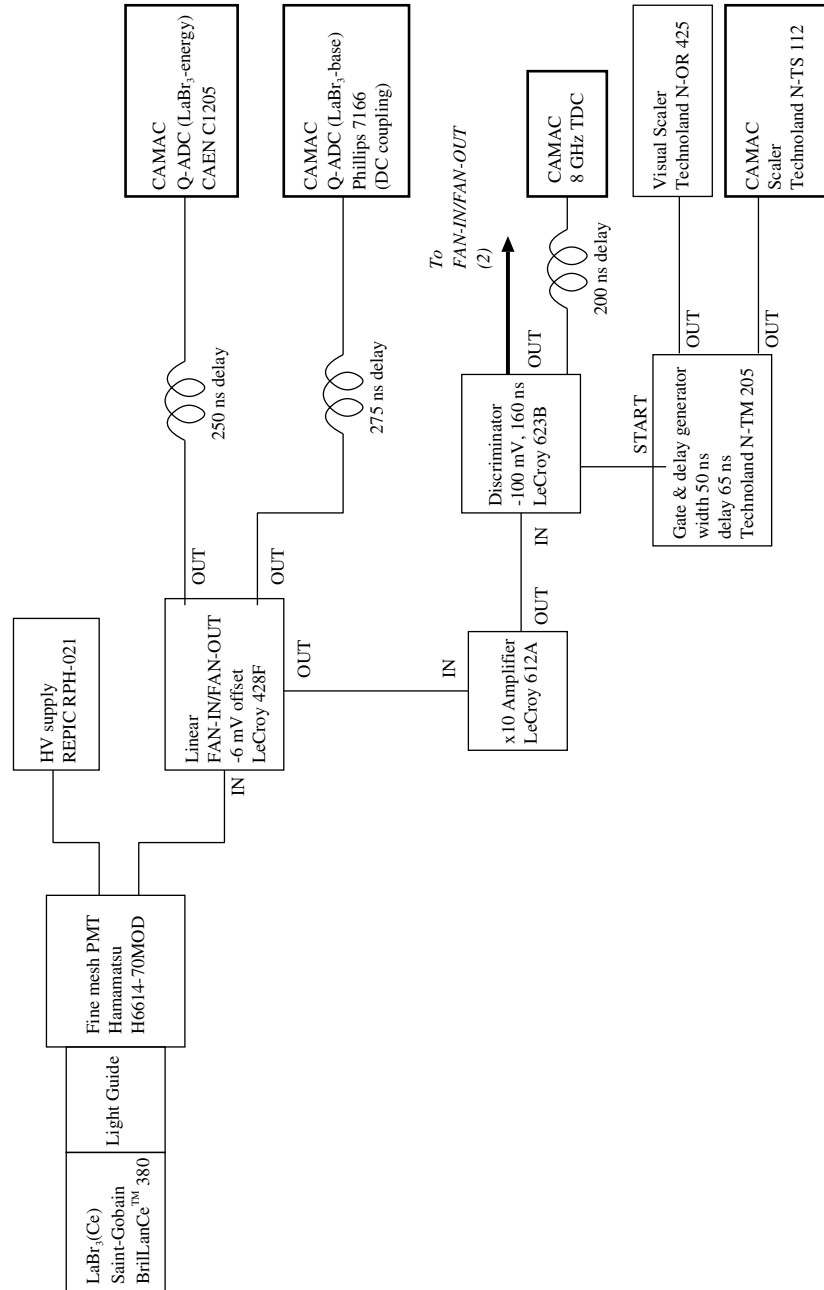
## 3.7 Electronics

In this section, the NIM and CAMAC system used for data acquisition (DAQ) is described. A CLEAR-PULSE 607 NIM crate is used for High Voltage supply, and three REPIC RPN-011-053 NIM crate is used for others. CAMAC is controlled via Linux PC. Noise-cut transformers (DENKENSEIKI NCT-G) are used to reduce noises. Coaxial cables of FUJIKURA RG-174/U are used to connect between modules. Firstly, the overview is shown. Secondly, a  $\beta$ -tagging system and a  $\text{LaBr}_3(\text{Ce})$  system are described and then a trigger and gates generation system is explained. Finally, a CAMAC system to read all data is described.

### 3.7.1 Overview of DAQ

Figures 3.27–3.31 show our DAQ system. Figure 3.32 shows the timing chart of main signals. The DAQ system consists of 4 parts. The first one is a  $\beta$ -tagging system, which receives signals from plastic scintillators and generates the timing signal of Ps formation. The second one is a  $\text{LaBr}_3(\text{Ce})$  system, which receives signals from  $\text{LaBr}_3(\text{Ce})$ , and generates the timing signal of Ps decay. The third one is a trigger and gates generation system, which generates a trigger through NIM logical circuit from the Ps formation signal of the  $\beta$ -tagging system and the Ps decay signal of the  $\text{LaBr}_3(\text{Ce})$  system. The fourth one is a CAMAC system, which reads the charge and timing information from analog-to-digital

Figure 3.27: DAQ of  $\beta$ -tagging system.

Figure 3.28: DAQ of  $\text{LaBr}_3(\text{Ce})$  system.



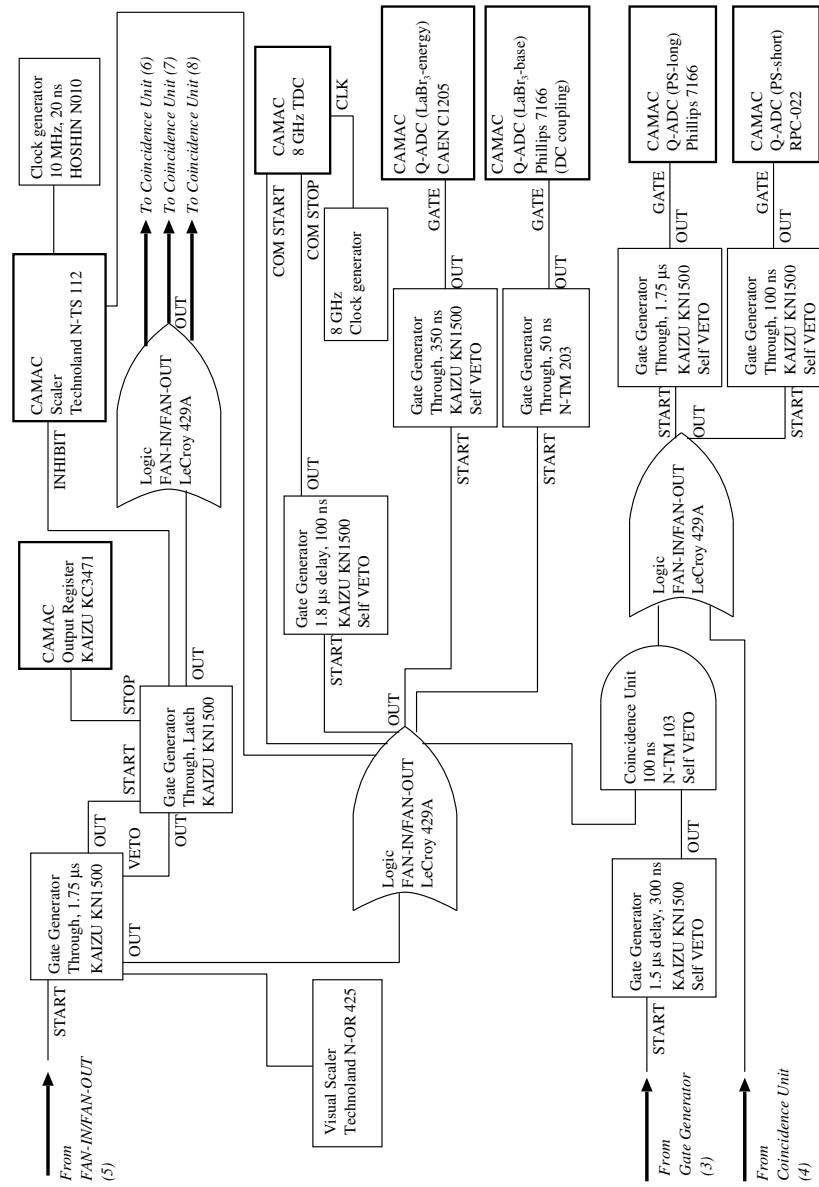


Figure 3.30: DAQ of gates generation system.

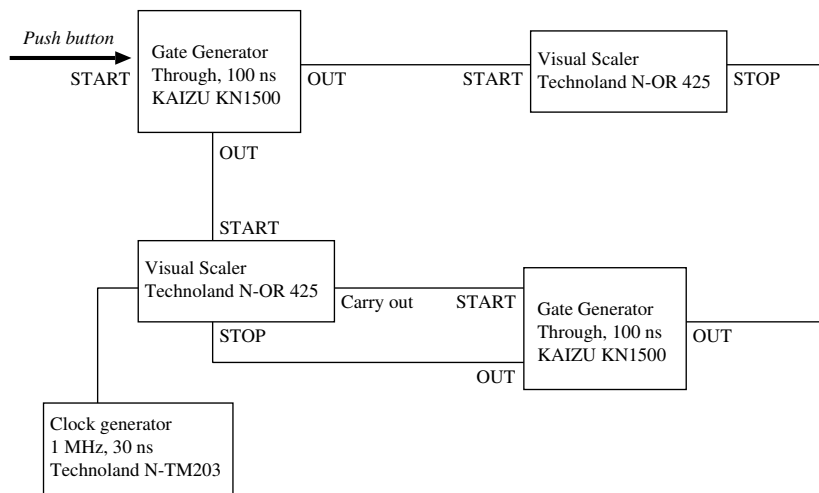


Figure 3.31: DAQ of visual scaler system.

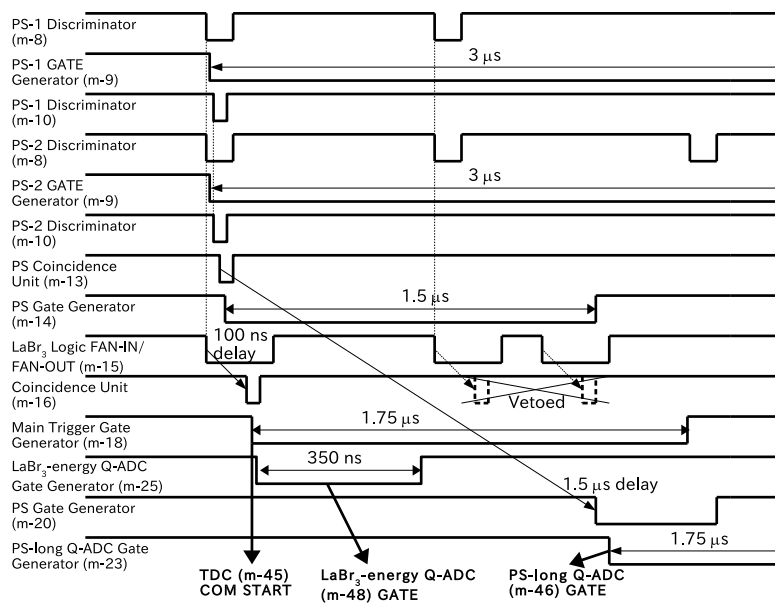


Figure 3.32: Timing chart of electronics.

converters (ADCs) and time-to-digital converters (TDCs), and records them to HDD of a Linux PC. During the data reading of CAMAC, veto signals are generated by NIM latch system to avoid further DAQ. The system are released for the next event when the data reading finishes.

Figure 3.27 shows the DAQ of  $\beta$ -tagging system. The  $\beta$ -tagging system is used to make a signal of a positron emitted from the source and going to the Ps formation volume in the RF cavity. This signal is a start signal, and it gives the timing of Ps formation ( $t = 0$ ). The energy deposit in the plastic scintillator by the positron is also measured. The signals of the two fine mesh PMTs (let PS-1 and PS-2 denote them) are processed individually.

Figure 3.28 shows the DAQ system for  $\text{LaBr}_3(\text{Ce})$  signal. The  $\text{LaBr}_3(\text{Ce})$  system is used to make a signal of a detection of  $\gamma$  rays from a Ps decay. This signal generates a trigger by coincidence with a signal of the  $\beta$ -tagging system, and it gives the timing of Ps decay. The energy of  $\gamma$  rays are also measured. This energy information is quite important to enhance the signal-to-noise ratio and obtain resonance lines of the Zeeman transition. The signals of the six fine mesh PMTs (let  $\text{LaBr}_3(\text{Ce})$  -1– $\text{LaBr}_3(\text{Ce})$  -6 denote them) are processed individually.

Figure 3.29 shows the DAQ trigger system, and Fig. 3.30 shows the DAQ gate generation system. The trigger signal for DAQ starting is generated by coincidence of the  $\beta$ -tagging system and the  $\text{LaBr}_3(\text{Ce})$  system. The gate and start signals of the CAMAC modules are generated by this trigger signal.

### 3.7.2 CAMAC

The CAMAC system is used for DAQ. A CAMAC crate of TOYO PS-7500 is used. Information obtained via CAMAC is timing and energy of the  $\beta$ -tagging system, timing and energy of the  $\text{LaBr}_3(\text{Ce})$  system, and rates of signals of NIM modules. Figure 3.33 shows the overview of the DAQ system.

## 3.8 Monte Carlo simulation

Monte Carlo simulations are used in fitting of the Zeeman resonance lines to estimate the ratio of detection efficiency of  $|1, 0\rangle$  decay normalized by that of the  $|1, \pm 1\rangle$  decay and polarization of positrons. This section describes details of the MC simulations.

Geant4 [67, 68] (release 4.9.6.p02) is used. Geant4 is a package which simulates the passage of particles and used in a wide areas including high energy physics such as the LHC experiment, nuclear and accelerator physics, as well as medical and space science. Validations of this package is widely performed. The low energy physics package of “option 4”, which is cited as the most precise in low energy region by the Geant4 collaboration team, is used. All of the experimental setup (materials, geometry, and the static magnetic field) are carefully input. Figures 3.34 and 3.35 show the geometry input in the simulation. The leading order of the energy spectrum of  $3\gamma$  decay was calculated firstly by Öre and Powell [70], which was confirmed later [71, 72]. The  $O(\alpha)$  correction was analytically calculated by Adkins [73]. In the MC simulation, the energy spectrum including this  $O(\alpha)$  correction is used, and the angular distribution of

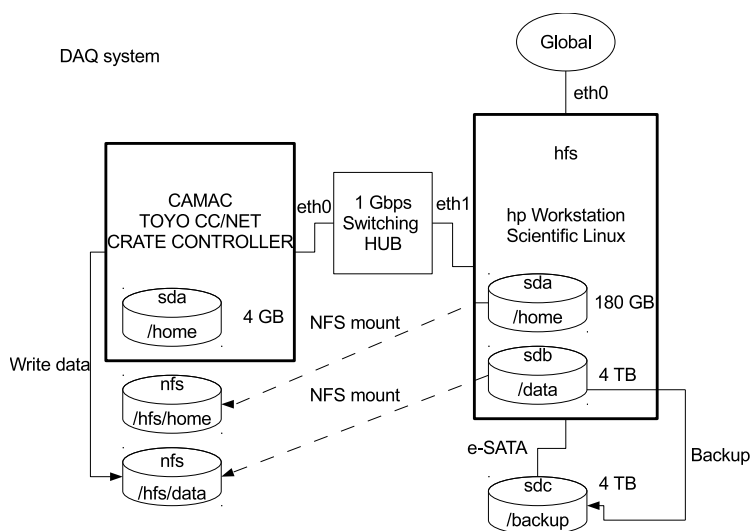


Figure 3.33: DAQ system.

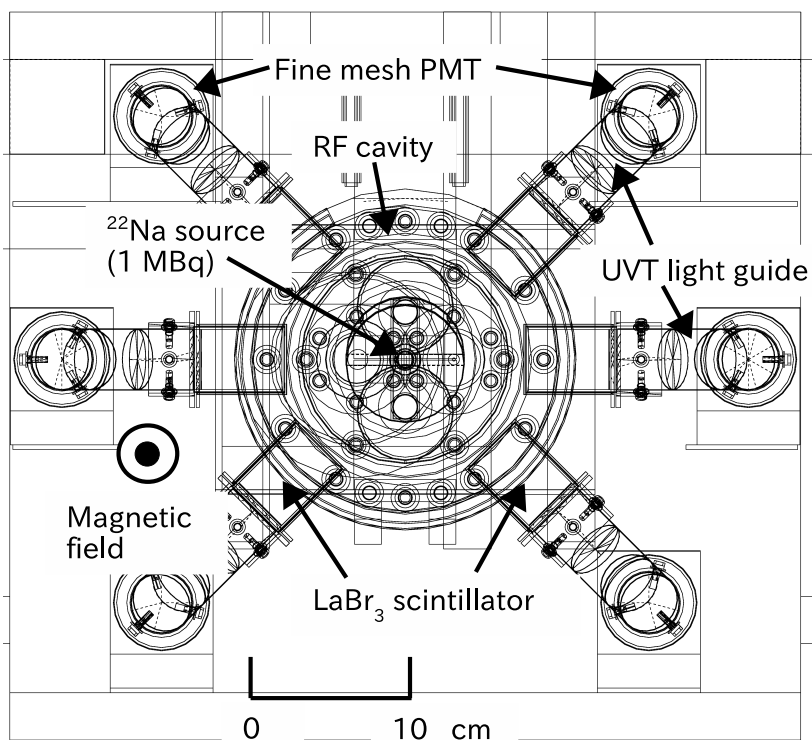


Figure 3.34: Side view of the geometry in the MC simulation.

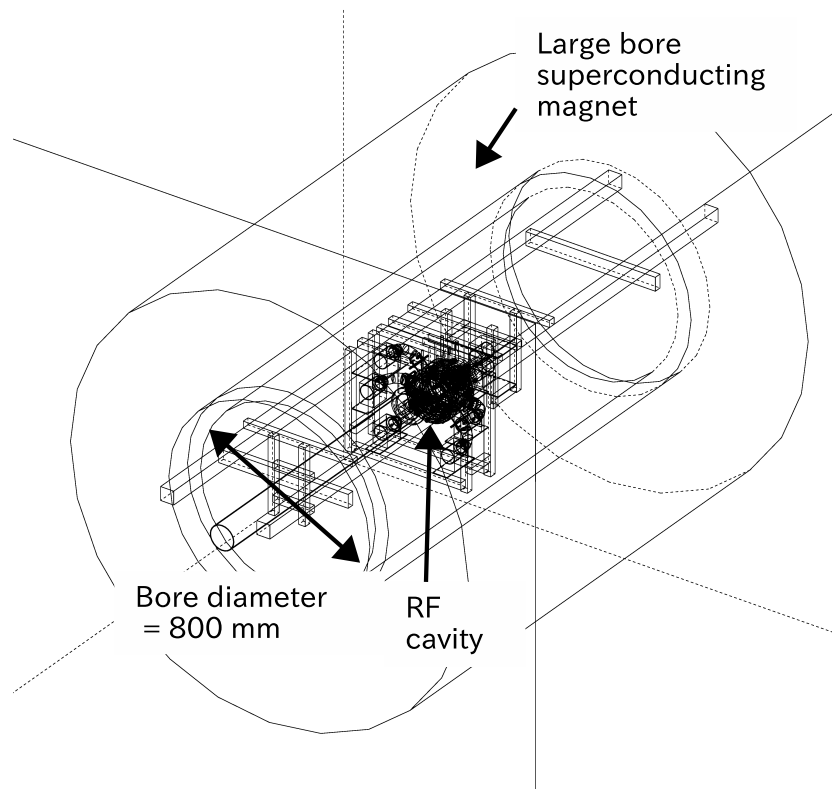


Figure 3.35: Bird's-eye view of the geometry in the MC simulation

decay  $\gamma$  rays are calculated using [46]. MC simulations are performed at every gas density and every static magnetic field strength of experimental data point.

### 3.9 Ps Thermalization Measurement

The thermalization parameters in  $i\text{-C}_4\text{H}_{10}$  gas are measured to be ( $E_0 = 3.1_{-0.7}^{+1.0}$  eV,  $\sigma_m = 146 \pm 11 \text{ \AA}^2$ ) by DBS (Doppler Broadening Spectroscopy) technique [60] in the range of 0.15–1.52 eV Ps kinetic energy. However, the DBS result cannot be applied for o-Ps whose kinetic energy is less than 0.17 eV since  $\sigma_m$  depends on the kinetic energy of Ps. As mentioned in Ref. [60], rovibrational excitations of the  $i\text{-C}_4\text{H}_{10}$  molecule increase  $\sigma_m$  of Ps with kinetic energy above 0.17 eV because  $i\text{-C}_4\text{H}_{10}$  has a vibrational level at 0.17 eV. The ‘pick-off technique’ [55, 56, 3], which can access o-Ps with lower energy than 0.17 eV, is a complementary method. This technique measures  $\Gamma_{\text{pick}}(t)/\Gamma_{\text{o-Ps}} = (2\gamma \text{ annihilation rate})/(3\gamma \text{ annihilation rate})$  as a function of time using  $\gamma$ -ray energy spectra. The thermalization can be measured by this method because  $\Gamma_{\text{pick}}(t)$  depends on the Ps velocity.

An experimental apparatus and results of our Ps thermalization measurement are described in Appendix B. The result of  $\sigma_m = 47.2 \pm 6.7 \text{ \AA}^2$  for o-Ps below 0.17 eV has been obtained by our independent thermalization measurement using the ‘pick-off technique’. In our analysis, the thermalization parameters from DBS measurement are used from  $t = 0$  to the time at which the kinetic energy of o-Ps reaches 0.17 eV, and then the  $\sigma_m$  is changed to our value.

### 3.10 Data acquisition

Duration of the measurement was from July 2010 to March 2013. The measurement was performed at the Cryogenic Science Center at KEK. In the overall period, the signal rate for each  $\text{LaBr}_3(\text{Ce})$  was around 800 Hz, the ‘OR’ rate of  $\text{LaBr}_3(\text{Ce})$  was around 4.5 kHz, the signal rate for each plastic scintillator was around 100 kHz, the coincidence rate of plastic scintillators was around 40 kHz, the trigger rate was around 1.7 kHz, and the data acquisition rate was around 910 Hz. The pedestal-taking and the event-taking were performed alternately. The mode was changed at about every 30 minutes. A typical length of pedestal-taking was 1 minute, and that of event-taking was 30 minutes.

The Zeeman transition was measured at various magnetic field strengths with fixed RF frequency and power. The transition resonance lines were obtained at 11 gas densities (0.129, 0.133, 0.167, 0.232, 0.660, 0.881, 0.969, 1.193, 1.353, 1.358, and 1.366 amagat). Data were taken at two different conditions, RF-ON and RF-OFF, at every gas density and magnetic field strength. RF-ON data were taken with microwaves supplied. RF-OFF data were taken without microwave by switching off the signal generator and the amplifier.

# Chapter 4

## Analysis

This chapter describes the analysis of the experimental data. All the analysis is performed using ROOT [74], and MINUIT [75] implemented in ROOT is used for fitting. Data are carefully analyzed to obtain time-evolutions of resonance lines, which will be used to see non-thermalized Ps effect.

### 4.1 Basic cuts and calibrations

This section describes basic cuts and calibrations of the data. As a sample, the figures and the numbers shown in this section is the data at the gas density of 0.881 amagat and the static magnetic field strength of 0.865 733 6 T. The same analysis are applied to all of the data.

#### 4.1.1 Cut: Time difference of the two PS signals

Events within a time difference between two PMT signals of the  $\beta$ -tagging system are selected in order to reject accidental noise. Details are as follows:

1. A spectrum of the time difference between the two PMTs (PS-2 – PS-1) is made at every 10 s.
2. The spectra is fitted by a Gaussian with a fitting range of the center  $\pm$ HWTM (Half Width at Tenth Maximum). Figure 4.1 shows a typical fitting of the time difference. Although the spectrum is not in a Gaussian shape because the timing resolution of plastic scintillator depends on the energy deposit, it does not affect the result since this Gaussian-fitting process is only for the determination of the center, the width, and their fluctuation.
3. The following condition is imposed using the s.d. of the fitted Gaussian:

$$|t_{\text{PS-1}} - t_{\text{PS-2}}| < 5\text{s.d.}, \quad (4.1)$$

where  $t_{\text{PS-1}}$  is the timing of PS-1, and  $t_{\text{PS-2}}$  is the timing of PS-2.

Events remains after this cut is  $\approx 98\%$  of the total events.

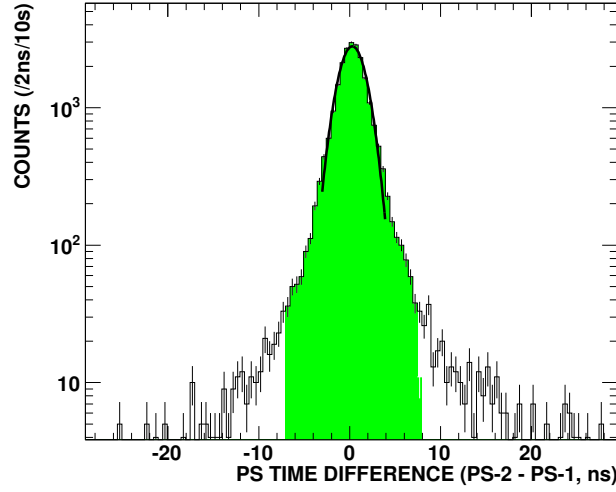


Figure 4.1: Time difference of the PMTs of the plastic scintillator. The histogram shows the observed data, and the curved line is the best-fit by a Gaussian. The green area remains after the cut.

#### 4.1.2 Calibration: Energy of the plastic scintillator

The energy of the plastic scintillator is calibrated using the mean value of the Q-ADC as follows:

1. Simply 0 ch of Q-ADC is regarded as the pedestal because Phillips 7166 automatically corrects the pedestal to 0 ch.
2. The mean value of Q-ADC is regarded as 12.7 photoelectrons (p.e.). This value is determined by a measurement of photoelectrons without any static magnetic fields, in which situation the PMTs are well calibrated using an LED. Uncertainty of this calibration does not affect the Ps-HFS value because the absolute counts of photoelectrons is not used any more in the analysis.

#### 4.1.3 Calibration: Energy of the $\text{LaBr}_3(\text{Ce})$ scintillators

Pedestals of  $\text{LaBr}_3(\text{Ce})$  energy are calibrated every 10 s. Pedestal information is taken even in the event-taking mode because energy information of all the  $\text{LaBr}_3(\text{Ce})$  is recorded when at least one of the all  $\text{LaBr}_3(\text{Ce})$  outputs signal, which means that pedestals of the PMTs which do not output signal are recorded simultaneously. A histogram of energy of every  $\text{LaBr}_3(\text{Ce})$  is made every 10 s livetime, and the pedestal peak is fitted by a Gaussian with a range of mean  $\pm$  FWHM. The center of the Gaussian is treated as a pedestal. The gains of  $\text{LaBr}_3(\text{Ce})$  energy are calibrated using 511 keV peak every 100 s.

#### 4.1.4 Time walk correction

The time walk is corrected for  $\text{LaBr}_3(\text{Ce})$  energy and  $\beta$  energy subsequently. Each timing spectrum of 12 different combination of  $\text{LaBr}_3(\text{Ce})$  and  $\beta$  is corrected independently.

##### Time walk correction of $\text{LaBr}_3(\text{Ce})$

The higher the energy of  $\text{LaBr}_3(\text{Ce})$ , the earlier the timing becomes, since the timing of  $\text{LaBr}_3(\text{Ce})$  is a minuend when the timing spectrum is made. The detail procedure is as follows:

1. A timing histogram is made every 200 s of livetime for every 50 keV energy window with the energy range of 250–450 keV.
2. Prompt peak of the histogram is fitted by a Gaussian where the fitting range is from mean–5 s.d. to mean+HWHM (half width at half maximum).
3. Fitted prompt peak is fitted by the following function  $f(E)$ :

$$f(E) = t - \sigma \sqrt{2 \ln \left( \frac{E}{E_0} \right)}, \quad (4.2)$$

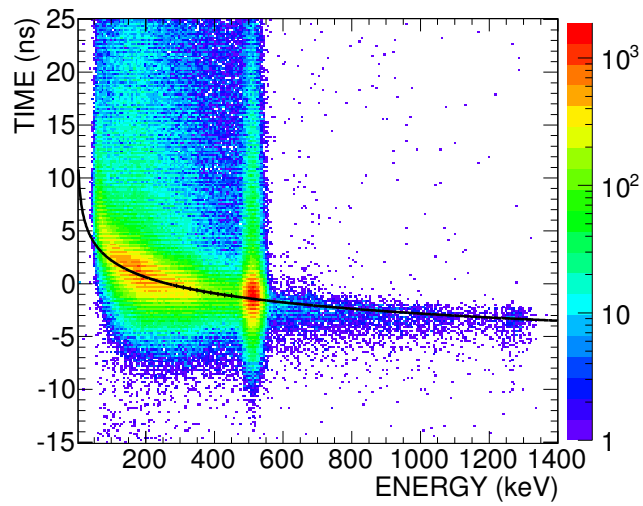
where the shape of the PMT signal is approximated to be a Gaussian with the center timing of  $t$  and s.d. of  $\sigma$ , and  $E_0$  corresponds to the threshold of the discriminator under this approximation.

Figure 4.2(a) shows the time-energy 2D plots, and black line show the fitted curve. Figure. 4.2(b) shows walk is corrected.

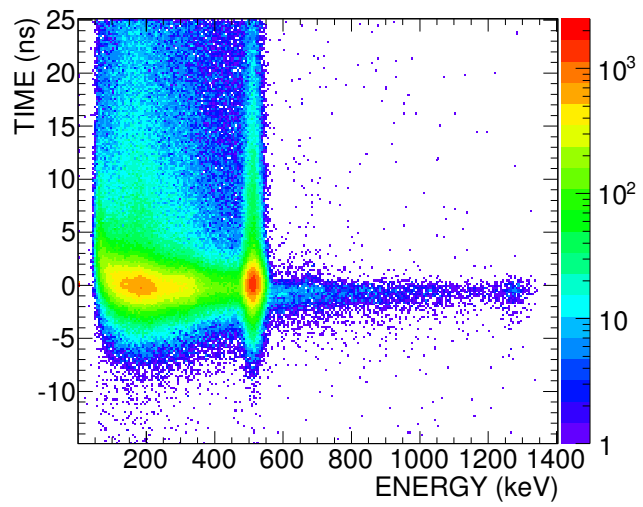
##### Time walk correction of the plastic scintillator

In the similar way, the walk of plastic scintillator is corrected as follows:

1. An energy histogram of each PMT (PS-1 or PS-2) is made for the total events with a bin width of 0.125 p.e. to determine the energy regions for making timing histograms.
2. Counting rate of the three bins, the maximum bin and the bins of both sides of that bin, is calculated. It is denoted as  $N_{\max}$  hereafter.
3. The energy histogram is divided into several windows with the same counting rate as  $N_{\max}$ .
4. A timing histogram is made every 200 s of livetime for every energy window.
5. The prompt peak of the histogram is fitted by a Gaussian by the same way as the time walk correction of  $\text{LaBr}_3(\text{Ce})$ .
6. The prompt timing is plotted as a function of energy.



(a)



(b)

Figure 4.2: Time walk correction of  $\text{LaBr}_3(\text{Ce})$ . (a) Before the time walk correction. The black solid line shows the result of the fitting. (b) After the time walk correction.

Table 4.1: Summary of cuts.

Cut on	Condition	Remaining events (%)
Time difference of plastic scintillator	$\pm 5$ s.d.	98
Time walk correction	Energy above “Threshold”	73
Energy balance of plastic scintillator	sqrt-difference in $\pm 5$ s.d.	73
Time difference of LaBr <sub>3</sub> (Ce)	All combination of LaBr <sub>3</sub> (Ce) $\pm 5$ s.d.	72

7. The plot is fitted by the following function  $g(E)$ :

$$g(E) = t_0 + \sigma \tanh(\tau(E - E_0)) + C\sqrt{E}, \quad (4.3)$$

where  $t_0$ ,  $\sigma$ ,  $\tau$ ,  $E_0$ ,  $C$  are constants. It fits to the data very well rather than using a function as Eq. (4.2), although Eq. (4.3) is not derived by any theoretical assumptions, *i.e.* it is only an empirical expression.

8. The timing is corrected by simply subtracting the value of the function  $g(E)$  from the original timing.

Figure 4.3(a) shows the time-energy 2D plots and black line show the fitted curve. Fig. 4.3(b) shows walk is corrected.

#### 4.1.5 Cut: Energy difference of the plastic scintillator

To reduce noise event, energy-balance deposited on both plastic scintillators is required. Figure 4.4(a) shows the 2D plot of two plastic scintillators. Both energies have good correlation. Figure 4.4(b) shows the difference ( $\sqrt{\text{energy of PS-1}} - \sqrt{\text{energy of PS-2}}$ ). It is required to be within 5 s.d. of this Gaussian.

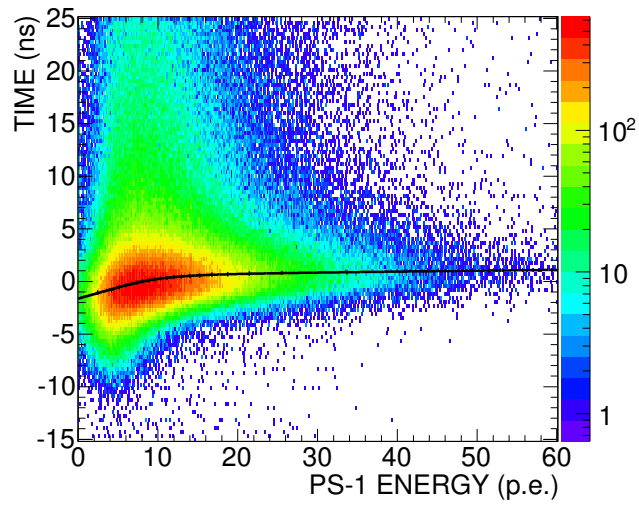
Almost all of the events pass this cut, but a little fraction of  $\approx 10^{-6}$  of the data are rejected.

#### 4.1.6 Cut: Time difference of LaBr<sub>3</sub>(Ce)

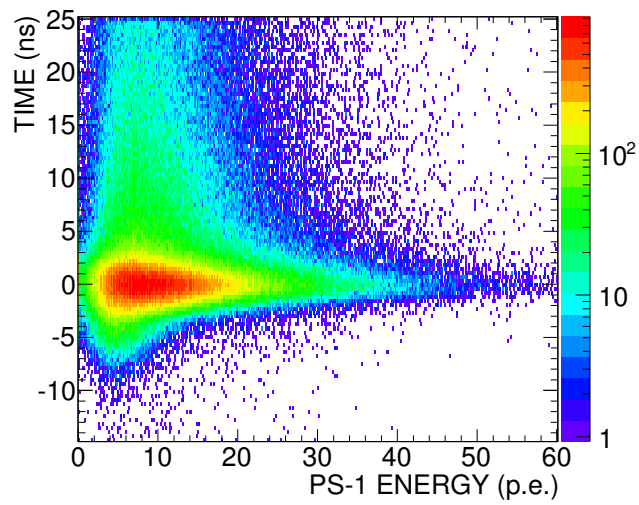
If more than one LaBr<sub>3</sub>(Ce) TDC stop signals are recorded, it is required that timing of every combination of two LaBr<sub>3</sub>(Ce) signals falls within 5 s.d. of the time resolution. 99.7% of the remained events passes this cut.

#### 4.1.7 Summary of cuts

Table 4.1 shows a summary of cuts and their acceptance fractions. About 70% of the total events remain after all the cut. These events are used for further analysis.

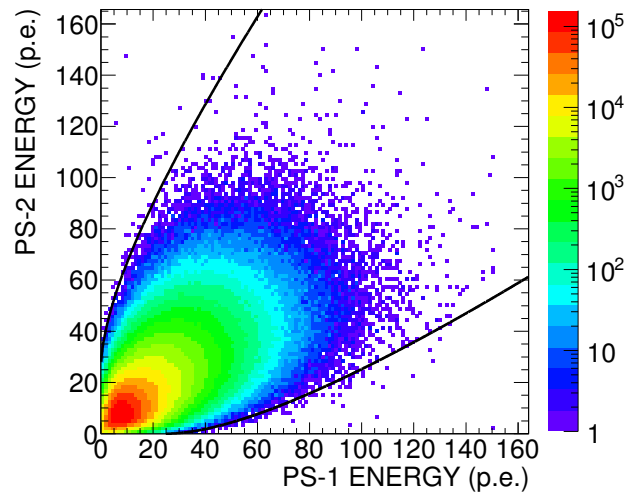


(a)

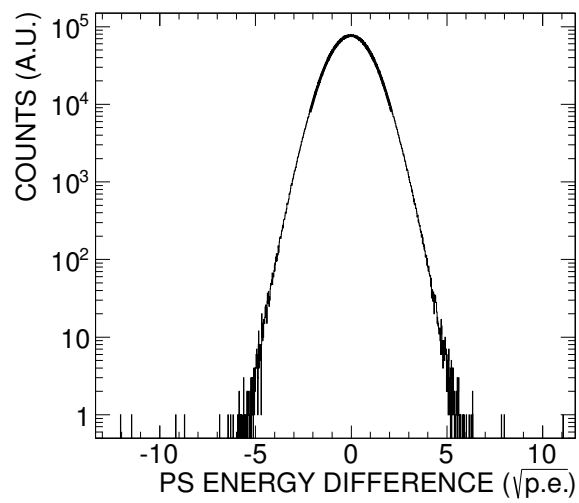


(b)

Figure 4.3: Time walk correction of the plastic scintillator. (a) Before the time walk correction. The black solid line shows the result of the fitting. (b) After the time walk correction.



(a) Distribution of charge of plastic scintillator PMTs. The black solid line shows the selection.



(b) Energy-sqrt-difference between two plastic scintillator PMTs. The heavy black line shows a fitting with a Gaussian.

Figure 4.4: Energy balance cut of the plastic scintillator.

## 4.2 Decay rate of Ps

In order to check quality of the data, decay rate and formation fraction of Ps are evaluated. All analysis in this section is performed with RF-OFF data. Analysis is performed at every gas density and every static magnetic field strength. The decay rate and formation fraction of Ps are determined by fitting the timing spectrum. The timing spectrum consists of four components; slow positrons,  $|+\rangle$  state,  $m_z = \pm 1$  states, and accidentals.

### 4.2.1 Deduction of the true signal timing distribution

The true signal timing distribution is deduced using Ref. [76]. Figure 4.5 shows a typical timing spectra between the  $\beta$ -tag and the  $\gamma$ -signal. The timing spectra without accidental contributions are obtained by subtracting the accidental spectra from the raw timing spectra. The difference from a simple exponential shape arises because of a change in efficiency of accidental events, which depends on the true signal shape. There are two origins of the accidental spectra. One is totally random stop pulses which are not correlated to the start pulses. It makes a simple exponential, almost flat, structure. Another is random stop pulses but correlated to the start pulses, which occurs as follows. Firstly, a positron makes a start pulse. Then, another positron makes a  $\beta$ -tagging signal and a stop signal earlier than a possible stop signal from the first start pulse. This is different from the totally random pulses, and the shape depends on the true signal timing spectrum. The true timing spectrum with true rate is obtained by correcting the suppression caused by the dead time of the electronics. The difference of the slope between RF-ON and RF-OFF is caused by the Zeeman transition. A timing window of 50–440 ns is applied to select o-Ps events. The window is divided into 11 sub-windows in the analysis, and the time evolution of the Zeeman transition is confirmed.

### 4.2.2 Fitting timing spectra of RF-OFF

Each signal timing spectrum is fitted with the following equation for  $N(t)$  which includes Ps thermalization effect [55, 56]:

$$N(t) = N_0 \exp \left[ -\Gamma_{\text{o-Ps}} \int_0^t \left( 1 + \frac{\Gamma_{\text{pick}}(t')}{\Gamma_{\text{o-Ps}}} \right) dt' \right] + N_1 \exp \left[ -\Gamma_{|+\rangle} \int_0^t \left( 1 + \frac{\Gamma_{\text{pick}}(t')}{\Gamma_{|+\rangle}} \right) dt' \right], \quad (4.4)$$

where  $N_0$  and  $N_1$  are normalization constants,  $\Gamma_{|+\rangle}$  is the decay rate of the  $|+\rangle$  state of Ps. The component of  $|-\rangle$  state is ignored because of its short lifetime. The time dependence of  $\Gamma_{\text{pick}}(t)$  is estimated using the following thermalization effect as

$$\Gamma_{\text{pick}}(n, t) = \Gamma_{\text{pick}}(n, \infty) \times \left[ \frac{v(t)}{v(\infty)} \right]^{0.6}, \quad (4.5)$$

in  $i\text{-C}_4\text{H}_{10}$  gas. The  $[v(t)]^{0.6}$  dependence is obtained by reading thermalization data from Fig. 2(c) of Ref. [77] and fitting them by a power-law function of velocity, which results in an exponent of  $\approx 0.6$ . The power-law dependence is

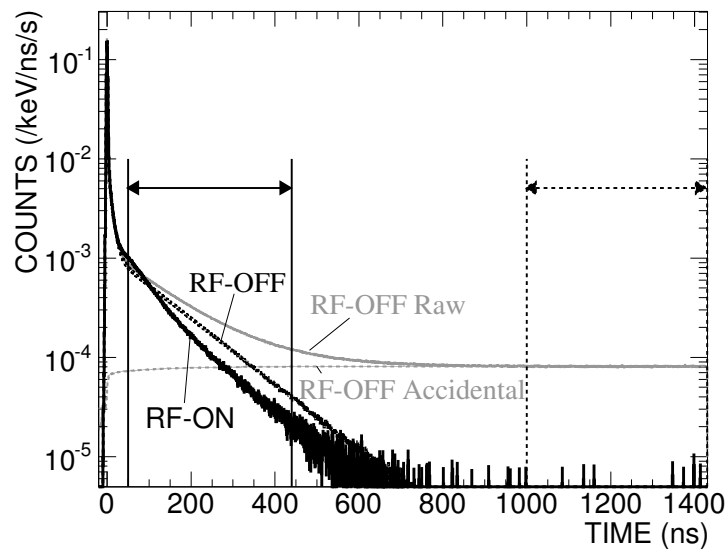


Figure 4.5: Timing spectra ( $n = 0.881$  amagat,  $B = 0.8657336$  T). The solid arrow shows the timing window used for transition lines, and the dashed arrow shows the accidental timing window used for subtraction of energy spectra. The accidental contribution has been already subtracted in the black 'RF-OFF' and 'RF-ON' lines. The data in the  $\gamma$ -ray energy range of 285–575 keV are shown. (Reproduced from Ref. [1])

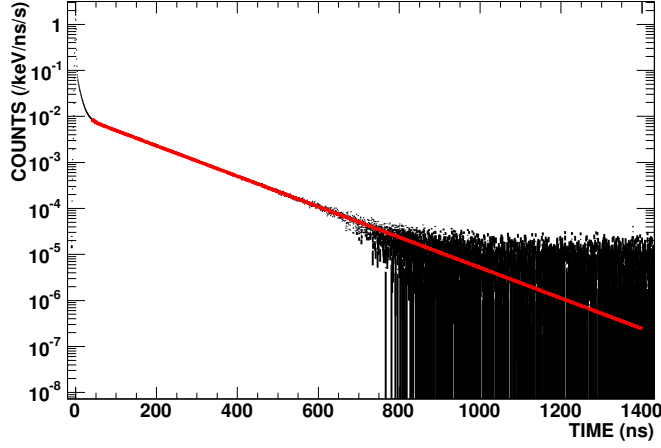


Figure 4.6: Fitting of RF-OFF timing spectrum ( $n = 0.881$  amagat,  $B = 0.865\,733\,6$  T). The black histogram is the data, and the red line is the fitting result. The data in the  $\gamma$ -ray energy range of 285–575 keV are shown.

indicated in Fig. 5 of Ref. [78]. Uncertainty in the power 0.6 is not large enough to affect  $\Delta_{\text{HFS}}$ .  $\Gamma_{|+\rangle}$  is calculated as a function of the static magnetic field strength as

$$\Gamma_{|+\rangle} = \frac{\Gamma_{\text{p-Ps}} + \Gamma_{\text{o-Ps}}}{2} - 2\pi\Delta_{\text{HFS}}\sqrt{\frac{\sqrt{I^2 + J^2} - I}{2}}, \quad (4.6)$$

$$I = 4x^2 + 1 - \frac{J^2}{4}, \quad (4.7)$$

$$J = \frac{\Gamma_{\text{p-Ps}} - \Gamma_{\text{o-Ps}}}{2\pi\Delta_{\text{HFS}}}, \quad (4.8)$$

where  $x$  is given as  $g'\mu_B B / (h\Delta_{\text{HFS}})$ , the same as in Chap. 2. Equations (4.6)–(4.8) are used in the fitting.

Figure 4.6 shows an example of the fitting, and Fig. 4.7 shows fitted  $\Gamma_{\text{pick}}(n, \infty)$  as a function of gas density.  $\Gamma_{\text{pick}}(n, \infty)$  at 0.167, 0.232, 0.660, and 0.881 amagat are apparently larger than others because vacuum level obtained before these runs were poorer. It is assumed to be the effect of residual gas, mainly water, in the cavity. This assumption is consistent with the fact that the residuals from the straight line are similar among these gas densities.

### 4.3 Timing windows

The difference of the slope of Fig 4.5 between RF-ON and RF-OFF is caused by the Zeeman transition. A timing window of 50–440 ns is used to select o-Ps events. This window is divided into 11 sub-windows: 50–60 ns, 60–70 ns, 70–80 ns, 80–90 ns, 90–105 ns, 105–120 ns, 120–140 ns, 140–165 ns, 165–200 ns, 200–260 ns, and 260–440 ns for the study of time-evolution. These sub-windows

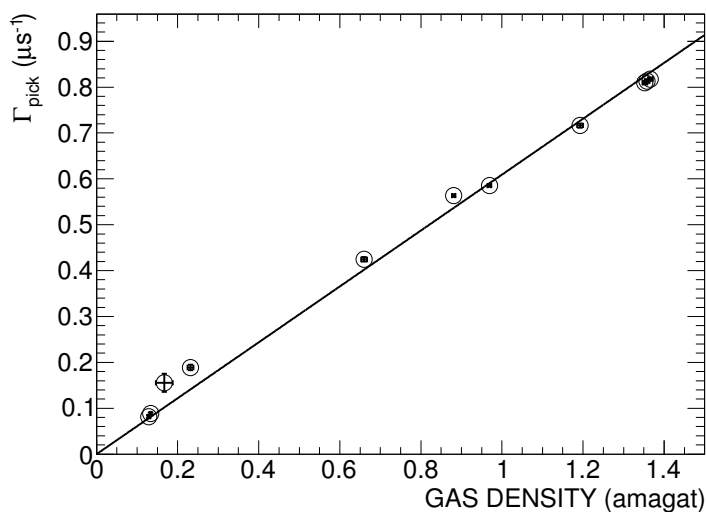


Figure 4.7: Fitted  $\Gamma_{\text{pick}}(n, \infty)$  as a function of gas density. The straight line is the linear best-fit result.

are determined so that each sub-window has roughly the same number of events. They are introduced to get better precision and confirm the time evolution of the Zeeman transition.

#### 4.4 Energy spectra

The energy spectra are obtained by subtracting the accidental contribution from the raw spectra as shown in Fig. 4.8. The accidental spectra are estimated using the energy spectra in a timing window of  $t = 1,000\text{--}1,430$  ns. RF-OFF spectra are also superimposed. It is clear that  $2\gamma$  decay events (observed as a peak at 511 keV) are enhanced by the Zeeman transition.

#### 4.5 The Zeeman resonance line

The resonance lines are obtained by  $(N_{\text{RF-ON}} - N_{\text{RF-OFF}})/N_{\text{RF-OFF}}$  as a function of the static magnetic field strength, where  $N_{\text{RF-ON}}$  is the counting rate of the events in the energy window of  $511 \text{ keV} \pm 1 \text{ s.d.} (\approx 17 \text{ keV})$  of RF-ON, and  $N_{\text{RF-OFF}}$  is that of RF-OFF. Obtained resonance lines with a best-fit function are discussed in the next chapter.

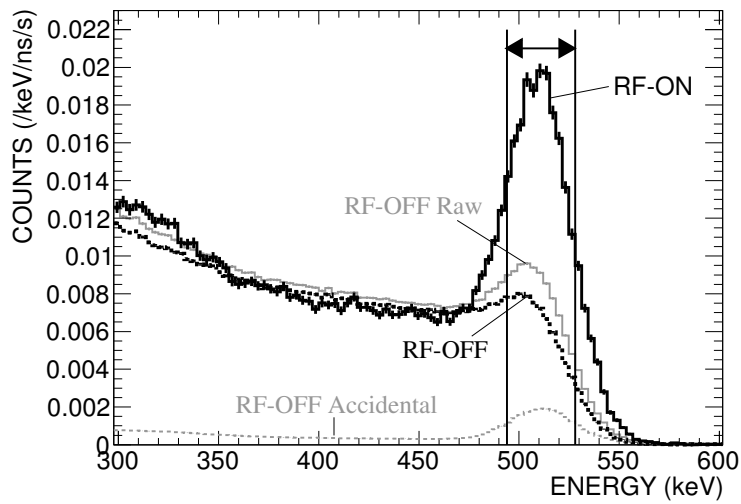


Figure 4.8: Energy spectra of the timing window of 50–60 ns ( $n = 0.881$  amagat,  $B = 0.8657336$  T). The accidental contribution has already been subtracted in the black ‘RF-OFF’ and ‘RF-ON’ lines. The transition lines are obtained by comparing the areas of RF-ON and RF-OFF spectra, inside the energy window indicated by the arrow. (Reproduced from Ref. [1])

# Chapter 5

## Results and Discussion

The Zeeman resonance lines are fitted for each gas density in this chapter. Ps thermalization effect is carefully treated in our fitting. It is shown that the non-thermalized Ps effect is crucial for measurement of  $\Delta_{\text{HFS}}$  and our result is consistent with QED prediction, disfavoring the previous experimental results by about 3 s.d.

### 5.1 Fitting of the Zeeman resonance lines

Figures 5.1–5.11 show the transition rate  $(N_{\text{RF-ON}} - N_{\text{RF-OFF}})/N_{\text{RF-OFF}}$  as a function of the static magnetic field strength. Following the calculations in Sec. 1.4.2, resonance lines are fitted by the following function  $F(t, n, B)$ :

$$F(t, n, B) = D_1(n) \frac{R_{\text{RF-ON}}(t, n, B) - R_{\text{RF-OFF}}(t, n, B)}{R_{\text{RF-OFF}}(t, n, B)} + D_2(n), \quad (5.1)$$

$$R(t, n, B) \equiv \epsilon(n) S_{2\gamma}(t, n, B) + S_{|1, \pm 1\rangle}(t, n, B) + \epsilon'(n) S_{|1, 0\rangle}(t, n, B), \quad (5.2)$$

$$(5.3)$$

where  $n$  is the number density of gas molecules,  $D_1(n)$  is a normalization factor,  $D_2(n)$  is an offset,  $\epsilon(n)$  and  $\epsilon'(n)$  are the relative detection efficiencies of  $2\gamma$  and  $|1, 0\rangle$  decay, respectively, normalized by that of the  $|1, \pm 1\rangle$  decay. Anihilation probabilities,  $S_{2\gamma}$ ,  $S_{|1, \pm 1\rangle}$ , and  $S_{|1, 0\rangle}$  are calculated numerically from Eqs. (1.26), (1.28), and (1.29), respectively. In the fitting process,  $D_1(n)$  and  $D_2(n)$  are treated as free parameters for each gas density because of the following reason. The normalization of the counting rate using RF-ON and that of RF-OFF is sensitive to gas density, since  $i\text{-C}_4\text{H}_{10}$  slightly absorbs microwaves which makes the gas temperature high (the density low).  $\epsilon(n)$  and  $B_{\text{RF}}(n)$  (Eq. (1.16)) are also treated as free parameters since the distribution of Ps formation position in the cavity depends on the gas density and this dependency makes the detection efficiency and the effective  $B_{\text{RF}}$  depend on the gas density. A typical value of  $\epsilon$  is 6.5. The effective  $B_{\text{RF}}$  is typically decreased by about 10% from maximum value (typically 15 G) because of this distribution.  $\epsilon'$  is estimated by simulations in which all the materials are reproduced and

Ps formation position are also carried out. A typical value of  $\epsilon'$  is 1.139. The polarization of the positrons is also estimated by simulation. Estimated values are within the range between 0.23 (low gas density) and 0.42 (high gas density). The Doppler broadening effect is taken into account by a convolution with a Gaussian distribution of  $\omega$  with a s.d. of  $\omega\sqrt{kT/(m_{\text{Ps}}c^2)}$ , where  $c$  is the speed of light in vacuum.

The time dependence of  $\Delta_{\text{HFS}}(t)$  and  $\Gamma_{\text{pick}}(t)$  are estimated using the following thermalization effect and they are taken into account in the evolution of  $S_{2\gamma}$ ,  $S_{|1,\pm 1\rangle}$ , and  $S_{|1,0\rangle}$  as

$$\Delta_{\text{HFS}}(n, t) = \Delta_{\text{HFS}}^0 - Cn [v(t)]^{3/5}, \quad (5.4)$$

$$\Gamma_{\text{pick}}(n, t) = \Gamma_{\text{pick}}(n, \infty) \times \left( \frac{v(t)}{v(\infty)} \right)^{0.6}, \quad (5.5)$$

where  $\Delta_{\text{HFS}}^0$  is the Ps-HFS in vacuum and  $C$  is a constant.  $\Delta_{\text{HFS}}^0$  and  $C$  are common free parameters for the fitting of all data points. The obtained values of  $\Gamma_{\text{pick}}(n, \infty)$  in Sec. 4.2.2 are used in the fitting process. As shown in Figs. 5.1–5.11, the data points are well fitted by Eq. (5.1).

By fitting all of the data points (11 gas densities  $\times$  11 timing windows  $\times$  4–7 magnetic field strengths) simultaneously, the best-fit value of

$$\Delta_{\text{HFS}}^0 = 203.3942(16) \text{ GHz} \quad (5.6)$$

is obtained with  $\chi^2/\text{ndf} = 633.3/592$  and a  $p$ -value of 0.12. The fitting free parameters are  $D_1(n)$ ,  $D_2(n)$ ,  $\epsilon(n)$ ,  $B_{\text{RF}}(n)$  (11 parameters for each),  $\Delta_{\text{HFS}}^0$ , and  $C$ , totally 46 parameters. Fitted values of  $D_1(n)$ ,  $D_2(n)$ ,  $\epsilon(n)$ , and  $B_{\text{RF}}(n)$  are shown in Appendix C. Time evolution of some parameters:  $\rho_{00}(t)$ ,  $v(t)/c$ ,  $\Gamma_{\text{pick}}(t)$ , and  $\Delta_{\text{HFS}}(t)$ , at several gas density using our final fitting results are shown in Figs. 5.12–5.15. The graphs are drawn at the static magnetic field strengths of the nearest data points to the centers of the resonances at 0.129, 0.881, and 1.358 amagat gas density. Fig. 5.12 shows the time evolutions of a component  $\rho_{00}(t)$  of the density matrix  $\rho$ . The  $2\gamma$  annihilation rate is mainly proportional to this function (see Eq 1.26). The graphs are drawn for the RF-ON condition, and the shape depends on the microwave power. The prompt  $|-\rangle$  decay, the short components of  $|+\rangle$  decay, and then the long components of the Zeeman transition are reproduced well. At low gas densities, the measurements were performed with low microwave power to avoid gas discharges, which makes the slope of the long component gradual.

Figure 5.13 shows the time evolution of the normalized Ps velocity  $v(t)/c$ . It shows that thermalization takes a long time at low gas density. Small kinks where  $\sigma_{\text{m}}$  changes because the Ps energy crosses the 0.17 eV threshold can be seen but not affect the final results. Fig. 5.14 shows the time evolution of the pick-off annihilation rate  $\Gamma_{\text{pick}}(t)$ . The  $n [v(t)]^{0.6}$  dependence is caused by the Ps thermalization. The ‘pick-off technique’ measures this function to obtain the thermalization parameters. Fig. 5.15 shows the time evolution of  $\Delta_{\text{HFS}}(t)$ . A dramatic change of  $O(100)$  ppm is shown in the timing range earlier than 50 ns which we do not use for the analysis. A slow change of  $O(10)$  ppm is also evident at low gas density: this clearly shows the effect of non-thermalized o-Ps on the value of  $\Delta_{\text{HFS}}$ .

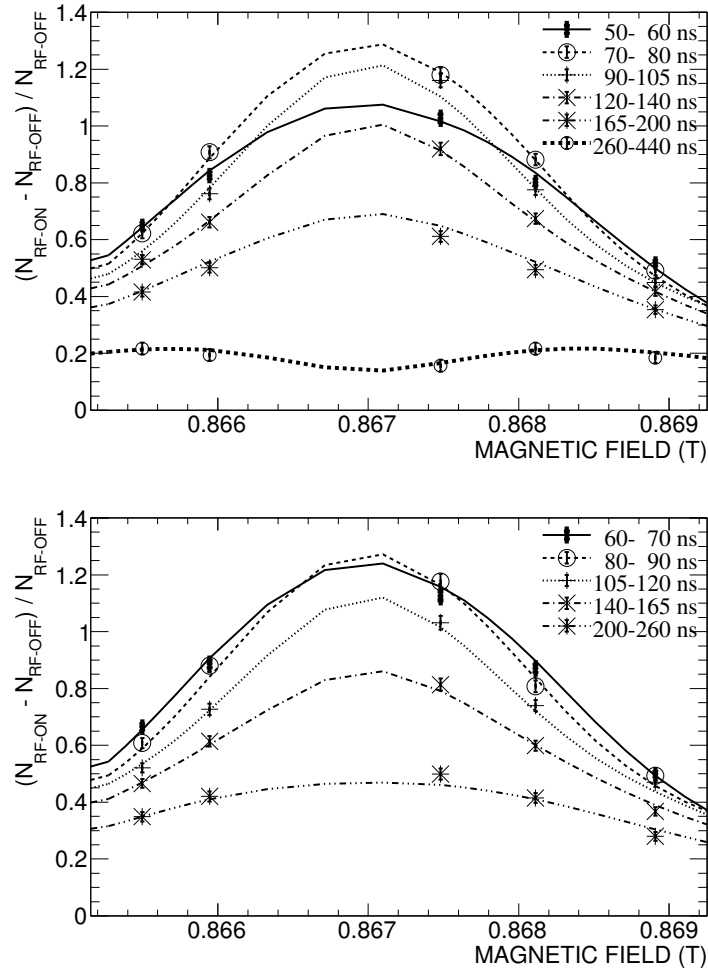


Figure 5.1: Resonance lines at a gas density of 0.129 amagat. The markers with error bars indicate obtained data, and the lines indicate the best-fit result. Eleven dataset for various time-windows are divided into two figures for improved visibility.

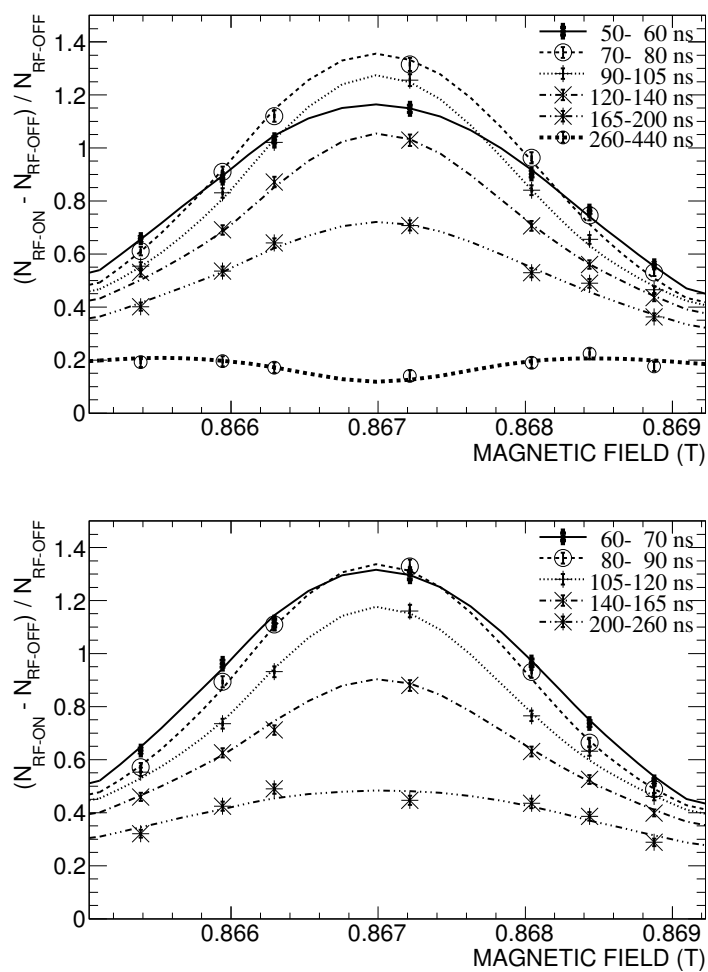


Figure 5.2: Resonance lines at a gas density of 0.133 amagat. The markers with error bars indicate obtained data, and the lines indicate the best-fit result. Eleven dataset for various time-windows are divided into two figures for improved visibility.

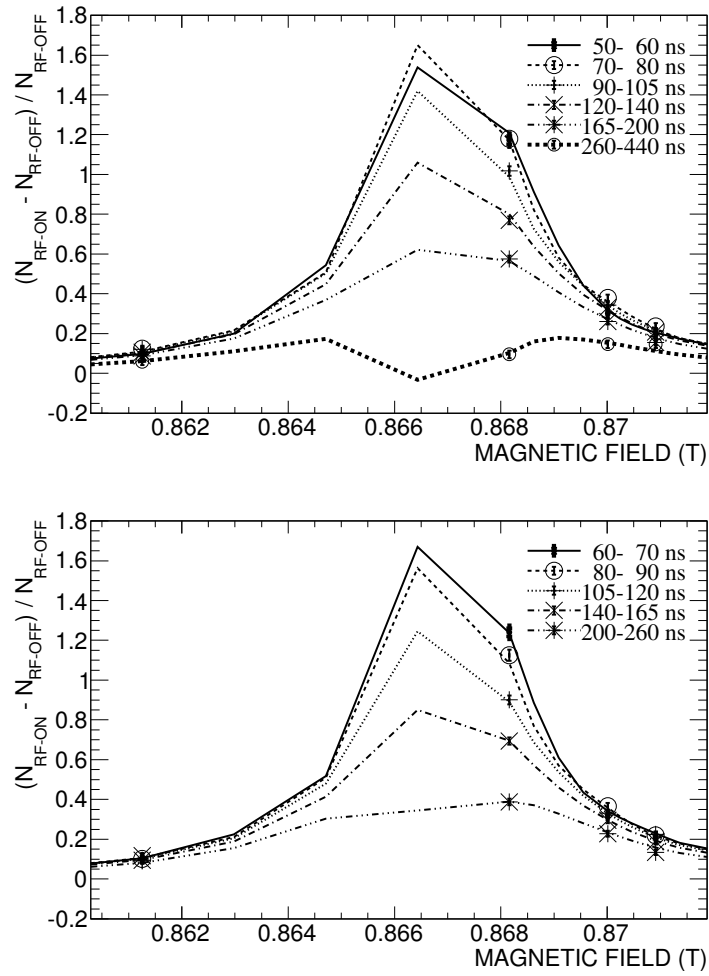


Figure 5.3: Resonance lines at a gas density of 0.167 amagat. The markers with error bars indicate obtained data, and the lines indicate the best-fit result. Eleven dataset for various time-windows are divided into two figures for improved visibility.

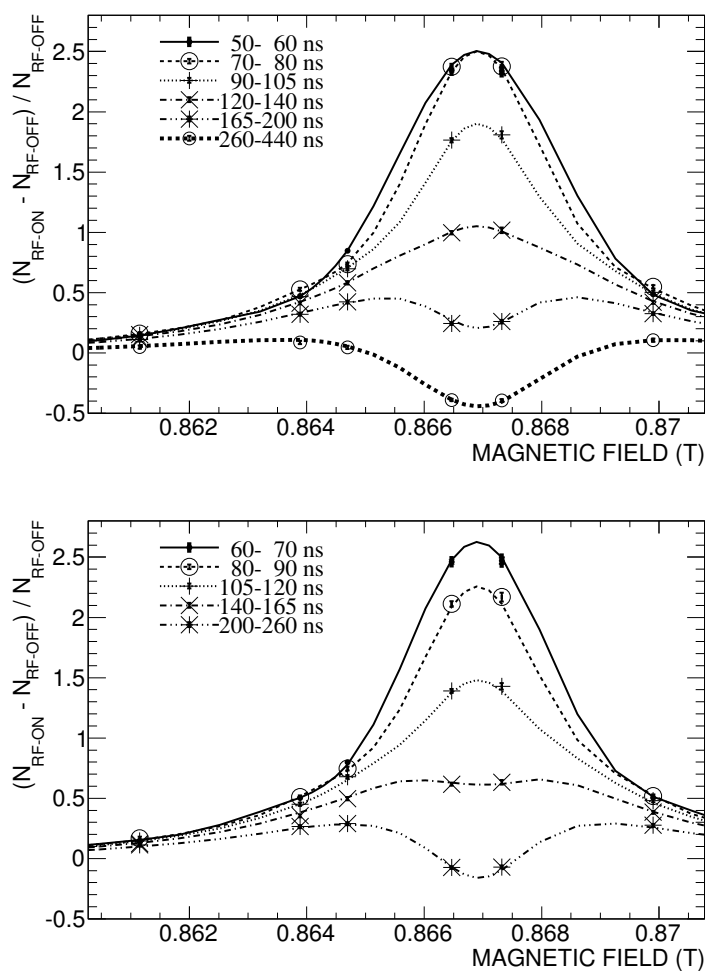


Figure 5.4: Resonance lines at a gas density of 0.232 amagat. The markers with error bars indicate obtained data, and the lines indicate the best-fit result. Eleven dataset for various time-windows are divided into two figures for improved visibility.

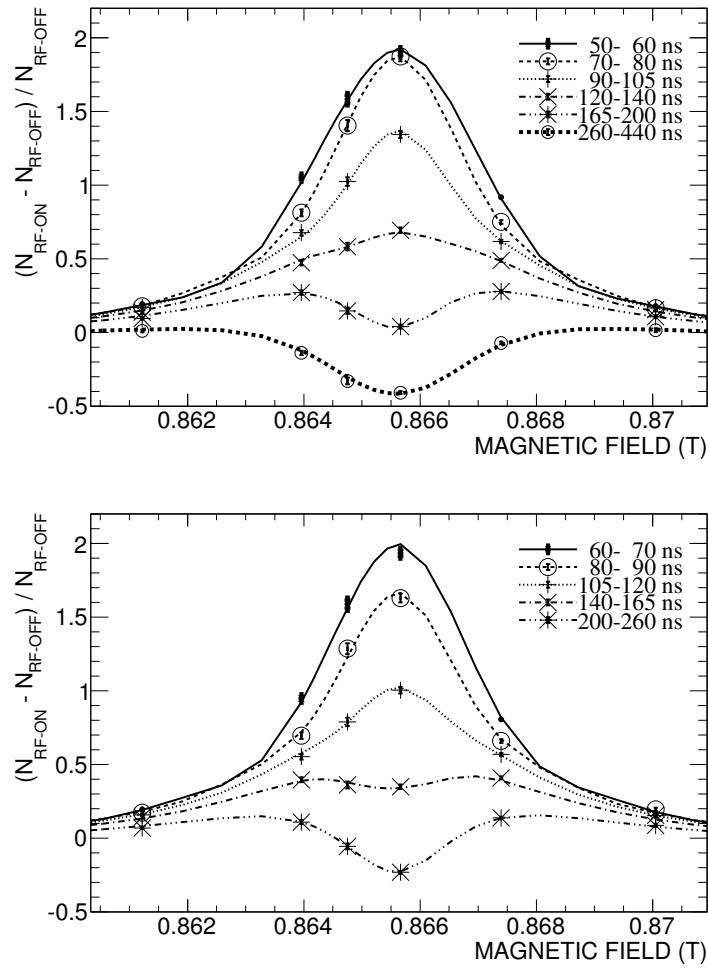


Figure 5.5: Resonance lines at a gas density of 0.660 amagat. The markers with error bars indicate obtained data, and the lines indicate the best-fit result. Eleven dataset for various time-windows are divided into two figures for improved visibility.

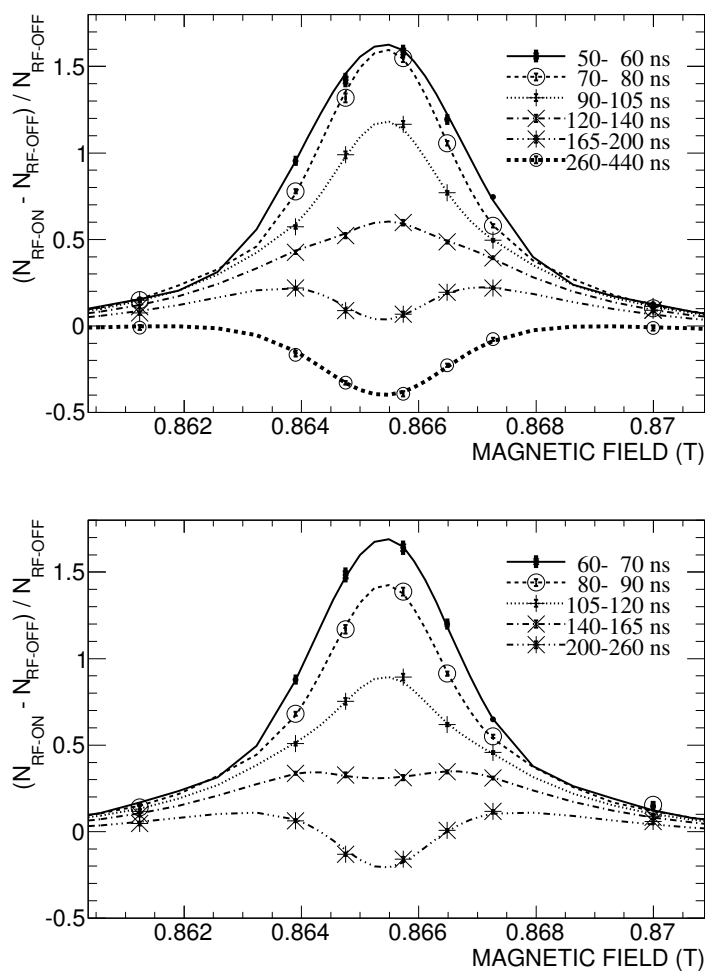


Figure 5.6: Resonance lines at a gas density of 0.881 amagat. The markers with error bars indicate obtained data, and the lines indicate the best-fit result. Eleven dataset for various time-windows are divided into two figures for improved visibility. (Reproduced from Ref. [1])

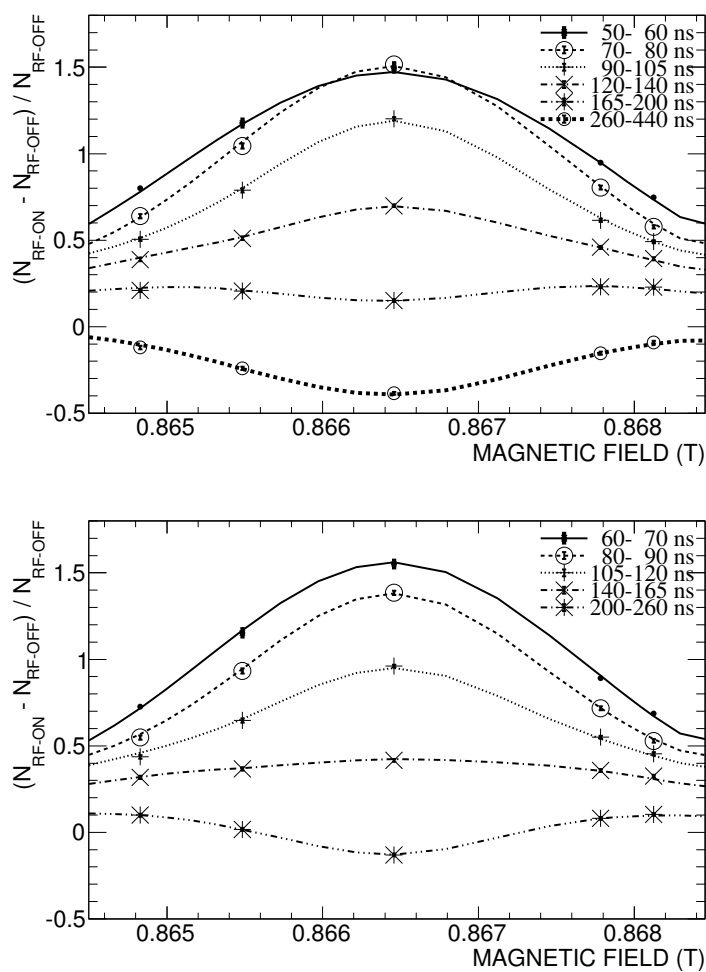


Figure 5.7: Resonance lines at a gas density of 0.969 amagat. The markers with error bars indicate obtained data, and the lines indicate the best-fit result. Eleven dataset for various time-windows are divided into two figures for improved visibility.

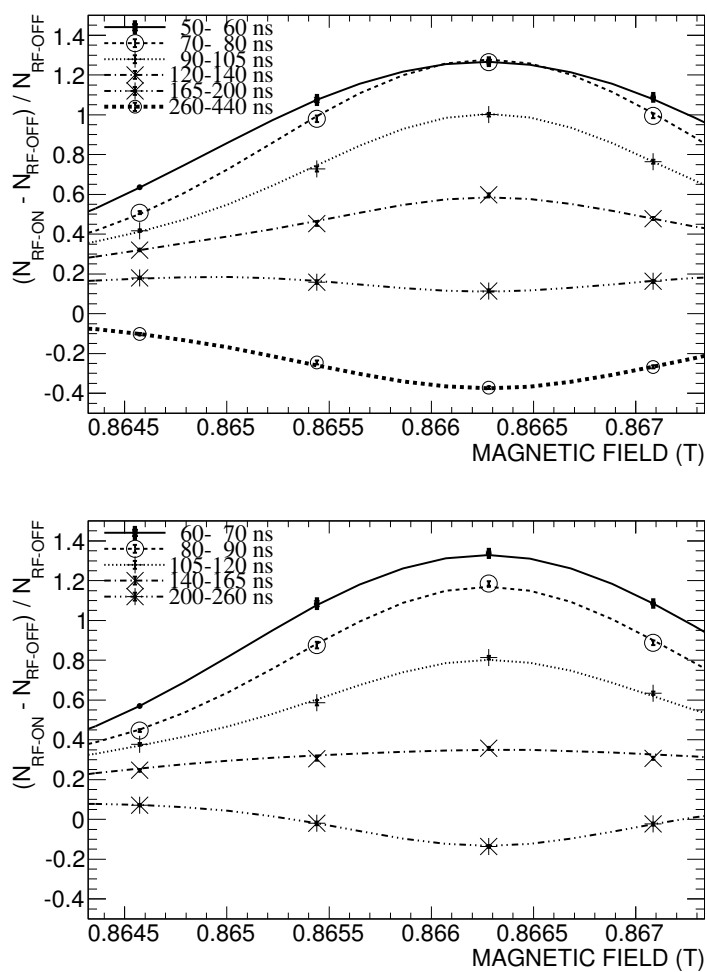


Figure 5.8: Resonance lines at a gas density of 1.193 amagat. The markers with error bars indicate obtained data, and the lines indicate the best-fit result. Eleven dataset for various time-windows are divided into two figures for improved visibility.

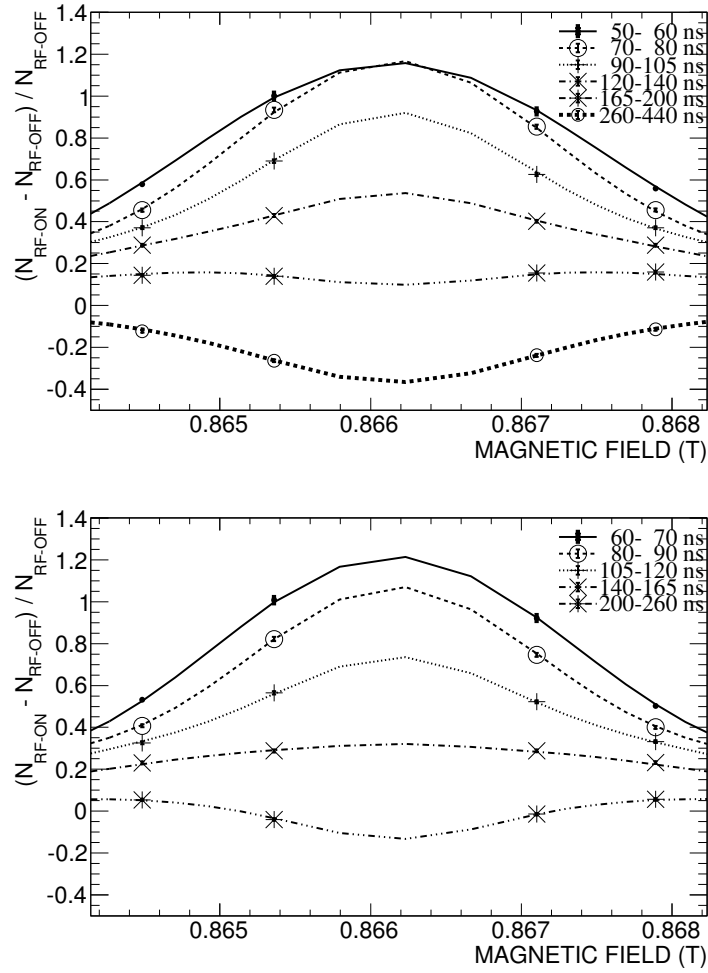


Figure 5.9: Resonance lines at a gas density of 1.353 amagat. The markers with error bars indicate obtained data, and the lines indicate the best-fit result. Eleven dataset for various time-windows are divided into two figures for improved visibility.

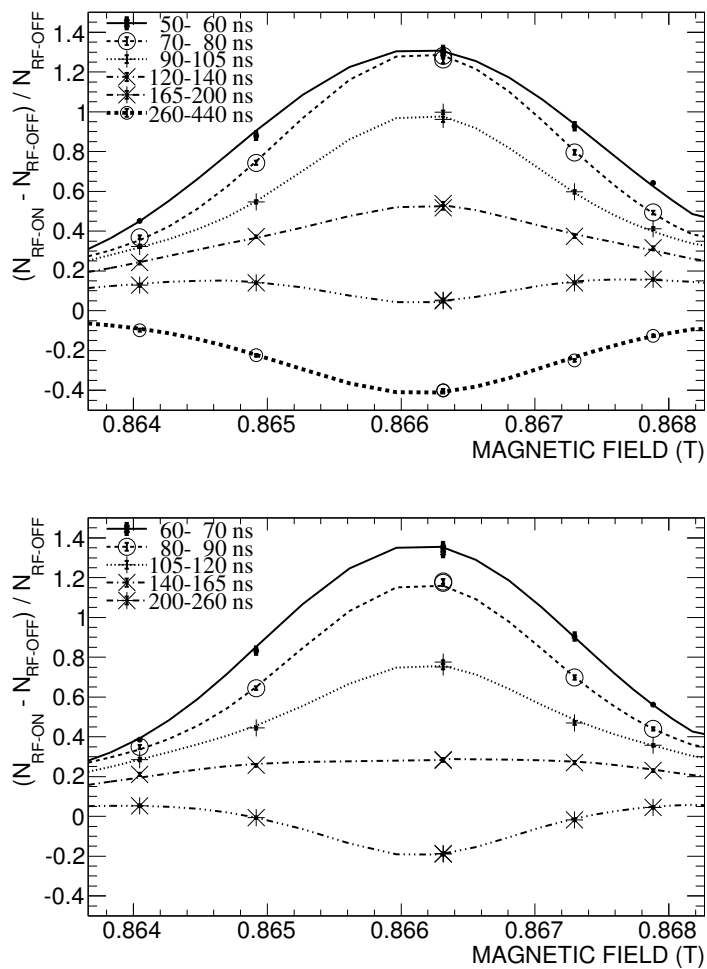


Figure 5.10: Resonance lines at a gas density of 1.358 amagat. The markers with error bars indicate obtained data, and the lines indicate the best-fit result. Eleven dataset for various time-windows are divided into two figures for improved visibility.

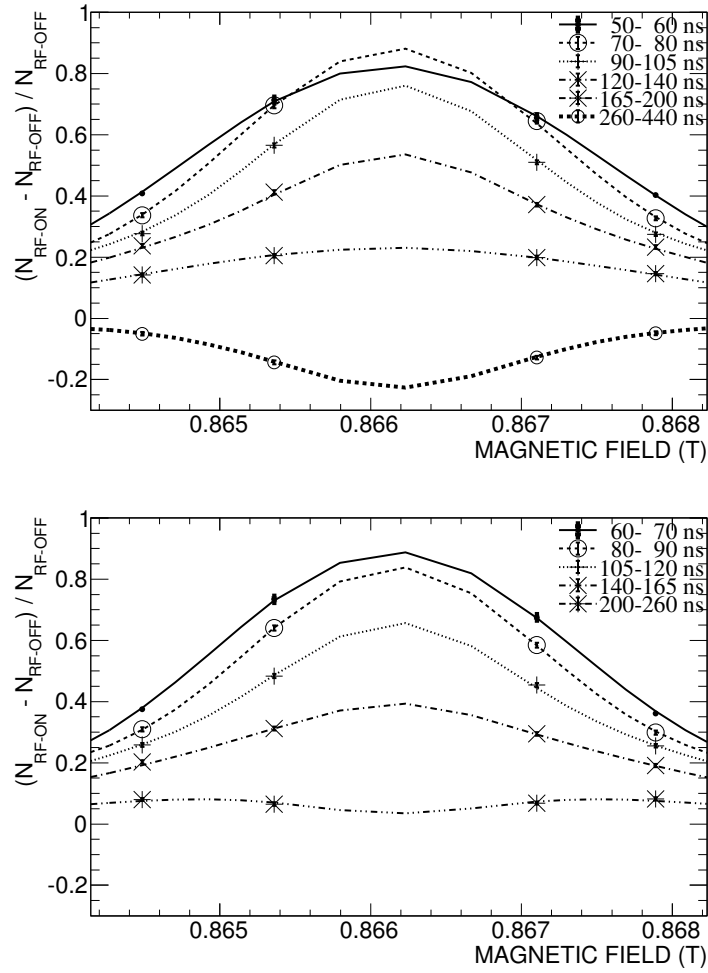


Figure 5.11: Resonance lines at a gas density of 1.366 amagat. The markers with error bars indicate obtained data, and the lines indicate the best-fit result. Eleven dataset for various time-windows are divided into two figures for improved visibility.

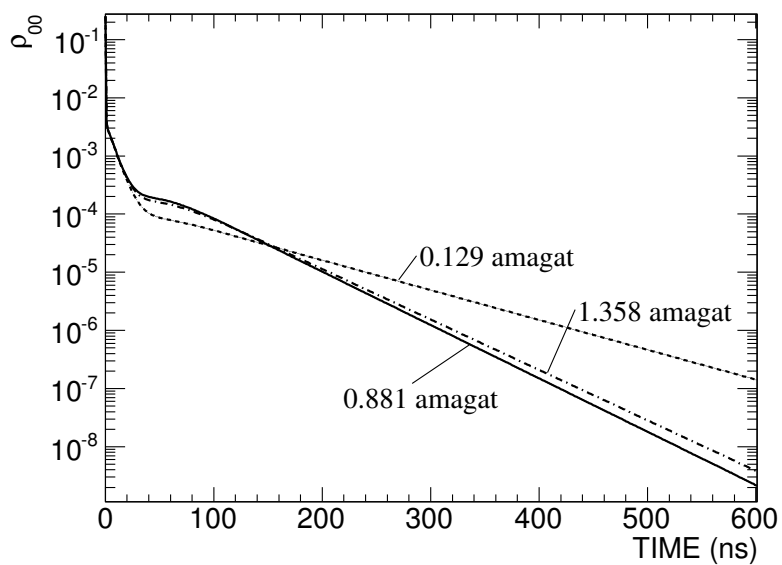


Figure 5.12: Time evolutions of  $\rho_{00}$  for various gas density. (Reproduced from Ref. [1])

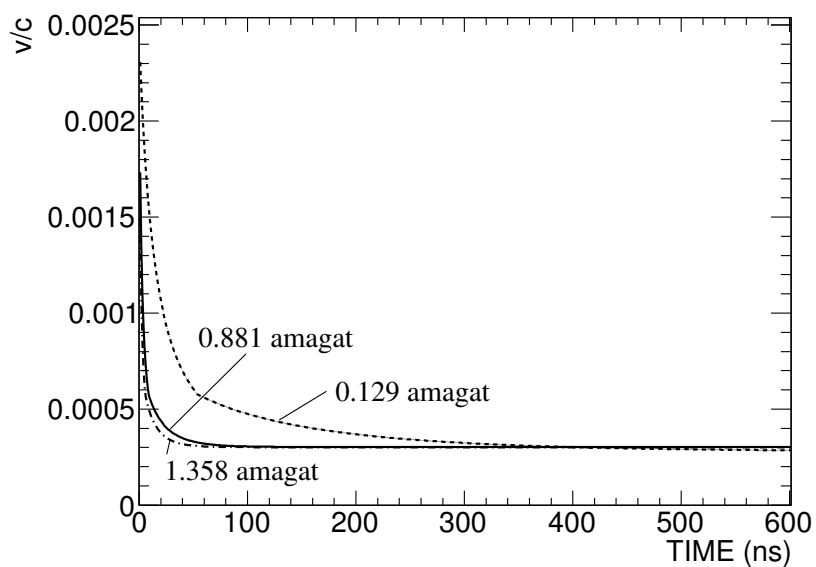


Figure 5.13: Time evolutions of mean velocity of Ps for various gas density. (Reproduced from Ref. [1])

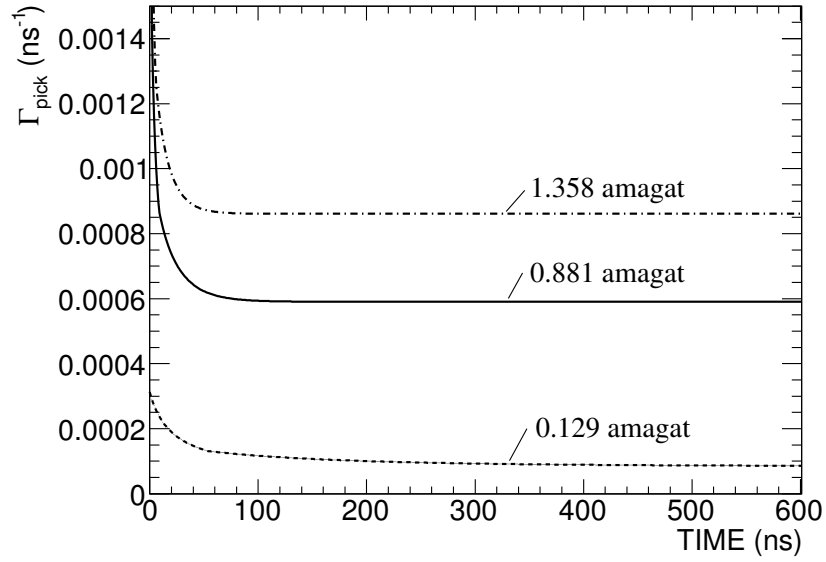


Figure 5.14: Time evolutions of pick-off annihilation rate for various gas density. (Reproduced from Ref. [1])

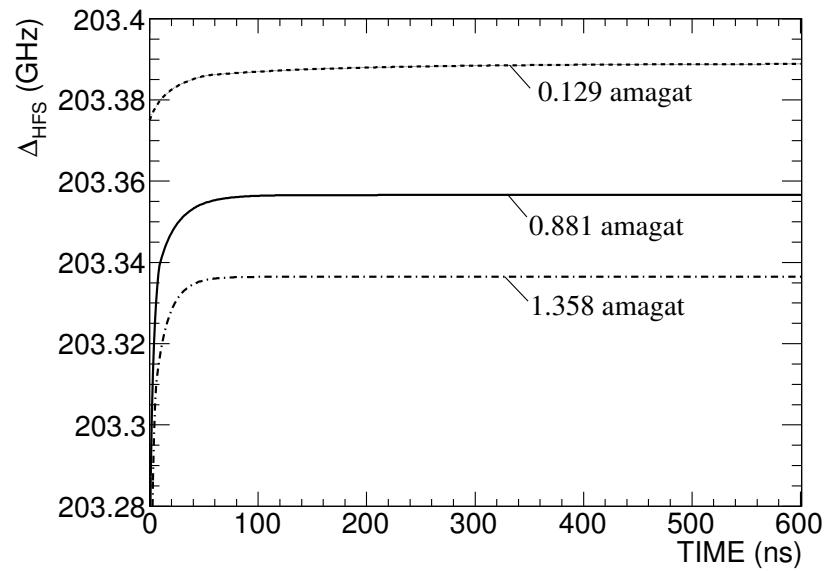


Figure 5.15: Time evolutions of  $\Delta_{\text{HFS}}$  for various gas density. (Reproduced from Ref. [1])

## 5.2 Systematic errors

Systematic errors are summarized in Table 5.1.

Table 5.1: Summary of systematic errors. (Reproduced from Ref. [1])

Source	Errors in $\Delta_{\text{HFS}}$ (ppm)
<i>Material Effect:</i>	
o-Ps pick-off	3.5
Gas density measurement	1.0
Temperature measurement	0.1
Spatial distribution of density and temperature inside the RF cavity	2.5
Thermalization of Ps:	
Initial kinetic energy $E_0$	0.2
DBS result $\sigma_m$	0.5
pick-off result $\sigma_m$	1.8
<i>Magnetic Field:</i>	
Non-uniformity	3.0
Offset and reproducibility	1.0
NMR measurement	1.0
<i>RF System:</i>	
RF power	1.2
$Q_L$ value of RF cavity	1.2
RF frequency	1.0
Power distribution in the cavity	< 0.1
<i>Others:</i>	
Choice of timing window	1.8
Choice of energy window	0.6
Polarization of $e^+$	< 0.2
Phase of microwaves	< 0.1
o-Ps lifetime	< 0.1
p-Ps lifetime	< 0.1
Quadrature sum	6.4

### 5.2.1 Material Effect

The largest contribution is an uncertainty of the material effect.

- The uncertainty of the o-Ps pick-off rate ( $\Gamma_{\text{pick}}(n, \infty)$ ) is estimated using the fitting error of the o-Ps decay curve.
- The uncertainty in the gas density is computed from the uncertainties of the gas pressure and temperature to be 0.2%, resulting in 1.0 ppm uncertainty in  $\Delta_{\text{HFS}}$ .
- The uncertainty of the gas temperature is 0.1 K, which corresponds to 0.1 ppm in  $\Delta_{\text{HFS}}$ .

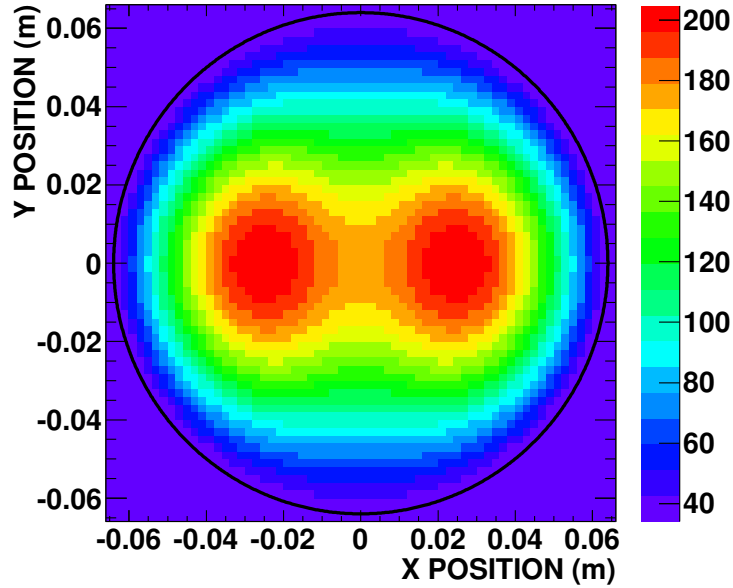


Figure 5.16: Spatial distribution of gas temperature in the RF cavity (axial view,  $n = 0.881$  amagat). The color indicates the gas temperature in  $^{\circ}\text{C}$ , and the black solid circle indicates the cavity wall.

- In estimating the systematic uncertainty due to spatial distributions of gas density and temperature in the RF cavity, distributions with the extreme condition of no gas convection were used. It is assumed that the strength of RF power absorbed by the gas is proportional to the energy density of electric field of the  $\text{TM}_{110}$  mode. As a result, a gas temperature distribution of  $\approx 170\text{ K}$  range is produced in the RF cavity, and the fitting result of  $\Delta_{\text{HFS}}$  shifts by  $+2.5$  ppm. A typical calculated temperature distribution is shown in Fig. 5.16. This shift is conservatively considered as a systematic error.
- The uncertainty in the Ps thermalization effect is estimated by the errors of the thermalization parameters: initial kinetic energy  $E_0$ , DBS result of  $\sigma_{\text{m}}$ , and pickoff-result of  $\sigma_{\text{m}}$ . These parameters are considered as independent, and effects of errors of them are 0.2 ppm, 0.5 ppm, and 1.8 ppm, respectively.

### 5.2.2 Magnetic Field

The second largest contribution is the uncertainty of the static magnetic field.

- The distribution of the static magnetic field is measured by an NMR magnetometer with the same setup as Ps-HFS measurement both before and after the Ps-HFS measurement. These two measurements are consistent with each other and the non-uniformity is weighted by the RF magnetic field strength and distribution of Ps formation positions, which results in

1.5 ppm RMS inhomogeneity.

- The strength of the static magnetic field is measured outside of the RF cavity during the run. An offset value at this point is measured during the measurement of the magnetic field distribution, and its uncertainty including reproducibility is 0.5 ppm.
- The precision of magnetic field measurement is 0.5 ppm, which comes from the polarity-dependence of the NMR probe.

These uncertainties are doubled because  $\Delta_{\text{HFS}}$  is approximately proportional to the square of the static magnetic field strength.

### 5.2.3 RF System

Uncertainties related to the RF system are estimated with all the RF parameters included in the fitting: power, cavity  $Q_L$ , and frequency.

- A long-term stability of 0.06% and a relative measurement uncertainty of 0.08% are associated with the power, which results in 0.10% total uncertainty, corresponding to 1.2 ppm error in  $\Delta_{\text{HFS}}$ .
- A long-term stability of 0.08% and a relative uncertainty of measurement of 0.06% are associated with the  $Q_L$  value, which also results in 0.10% total uncertainty, corresponding to 1.2 ppm error in  $\Delta_{\text{HFS}}$ .
- A long-term stability of 0.8 ppm and an absolute uncertainty of 0.6 ppm are associated with the frequency, which results in 1.0 ppm total uncertainty, corresponding to 1.0 ppm error in  $\Delta_{\text{HFS}}$ .
- In our final global-fitting, Eq. (1.24) is solved for a given average RF power. However, depending on their position the Ps see different power and the final results should be given by an average of several Eq. (1.24) for different power. A fitting with this method has been performed to estimate this effect. The distribution of Ps formation position is estimated using GEANT4 MC simulation. Time dependence of RF power for each Ps is ignored because the diffusion length of Ps within its lifetime is less than 1 mm and there is no large difference of RF power at this distance. A free parameter of proportionality coefficient to this distribution has been used instead of  $B_{\text{RF}}$ . The shift of  $\Delta_{\text{HFS}}$  has been less than 0.1 ppm. An estimation including spatial distribution of gas density has also been performed and the shift has also been less than 0.1 ppm. This shift is considered as a systematic error.

### 5.2.4 Others

Other systematic uncertainties are related to the analysis.

- Fittings with a starting time of 40 ns and 60 ns with a fixed fitting end time of 440 ns are performed in order to study the systematic error associated with the choice of the timing window (Fig. 5.17). Fittings with an ending time of 260 ns and 620 ns with a fixed start time of 50 ns are also performed (Fig. 5.18). There is no significant systematic dependence. The maximum shift in  $\Delta_{\text{HFS}}$  is 1.8 ppm and is considered to be a systematic error.

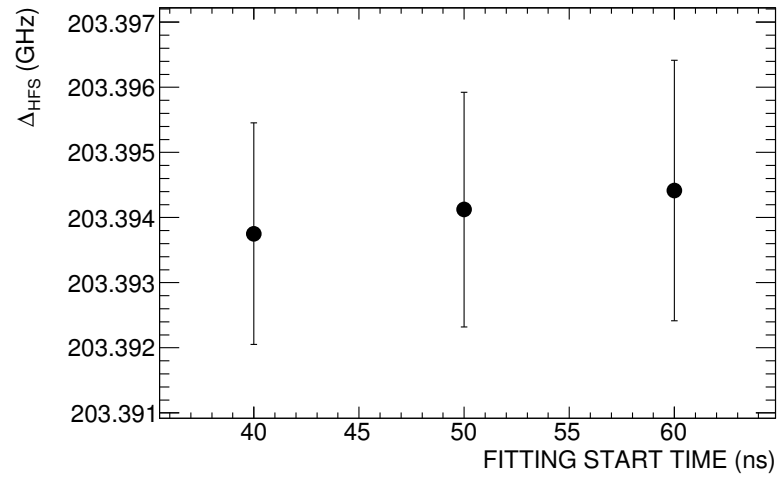


Figure 5.17: Fitting-start-time dependence of  $\Delta_{\text{HFS}}$ . The fitting ending time is fixed to 440 ns.

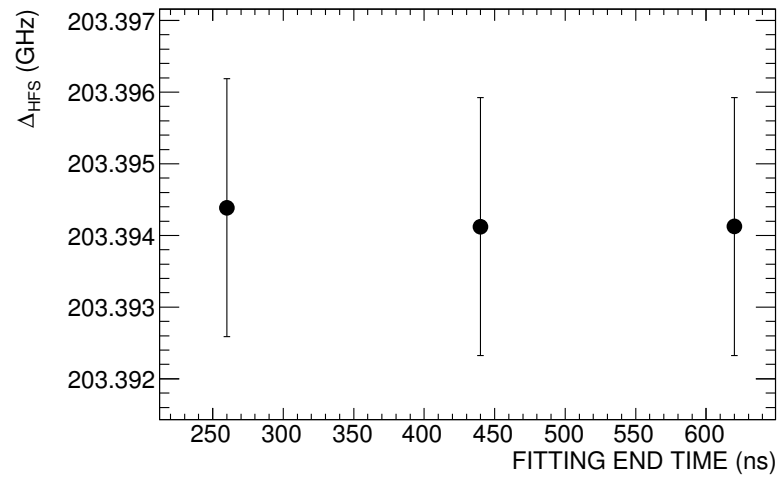


Figure 5.18: Fitting-end-time dependence of  $\Delta_{\text{HFS}}$ . The fitting starting time is fixed to 50 ns.

- The gain and offset of the detectors are calibrated every 10 minutes and these uncertainties are negligible. Analysis with energy window of  $511 \text{ keV} \pm 1.5 \text{ s.d.} (\approx 26 \text{ keV})$  has been performed, and the result shifted  $\Delta_{\text{HFS}}$  by 0.6 ppm. This shift is taken into account as a systematic error for the choice of the energy window. Other systematic errors from detectors are considered to be cancelled out by the subtraction of RF-OFF data from RF-ON data and the normalization by RF-OFF data.
- A comparison with an assumption that a positron is unpolarized has been performed, but the change in the final fitted Ps-HFS value is less than 0.2 ppm. This shows that the uncertainty of the dependence of polarization is less than 0.2 ppm.
- The uncertainty in the lifetime measurements of Ps affect  $\Delta_{\text{HFS}}$  by less than 0.1 ppm.
- The uncertainty in the MC estimation of  $\epsilon'$  is negligible because the contribution of the  $|1, 0\rangle$  state is small.
- An effect of excited states can be estimated using the Hamiltonian as shown in Ref. [79] and it is negligible.
- Other systematic errors such as the motional Zeeman and Stark effects, the spin-conversion quenching of Ps, the quadratic Zeeman effect, and smaller correction to  $g$  factor are negligible.
- Completely separate analysis which determine  $\Delta_{\text{HFS}}$  value at each gas density has been performed to provide additional insight into the complete experimental data set and confirm their quality. Figure 5.19 shows the result. It is obtained by fitting the resonance lines at each gas density without considering the time evolution of  $\Delta_{\text{HFS}}$ , *i.e.*  $\Delta_{\text{HFS}}$  is treated as a constant at each gas density instead of using Eq. (5.4). This method is similar to the method used in the previous experiments except that our data use timing information, which was not taken in the previous measurement, and 11 resonance lines within 50–440 ns timing window are simultaneously fitted at each gas density. It is impossible to include the time evolution of  $\Delta_{\text{HFS}}$  in this method. It is evident that the data fluctuations from the linear-fit function are reasonable compared to the error bars. It is important to say that determination of  $\Delta_{\text{HFS}}$  using our data needs our new global-fitting method to treat the time evolution correctly.
- Comparing Fig. 5.19 and Fig. 4.7, there is no significant correlation between vacuum quality and fluctuation of  $\Delta_{\text{HFS}}$  value. It shows that an effect of residual gas is negligible.

### 5.3 Ps-HFS value

Since the systematic errors discussed in the previous section are regarded as independent, and the total systematic error is calculated as a quadrature sum. The final result including systematic errors is:

$$\Delta_{\text{HFS}} = 203.3942 \pm 0.0016(\text{stat.}) \pm 0.0013(\text{sys.}) \text{ GHz.} \quad (5.7)$$

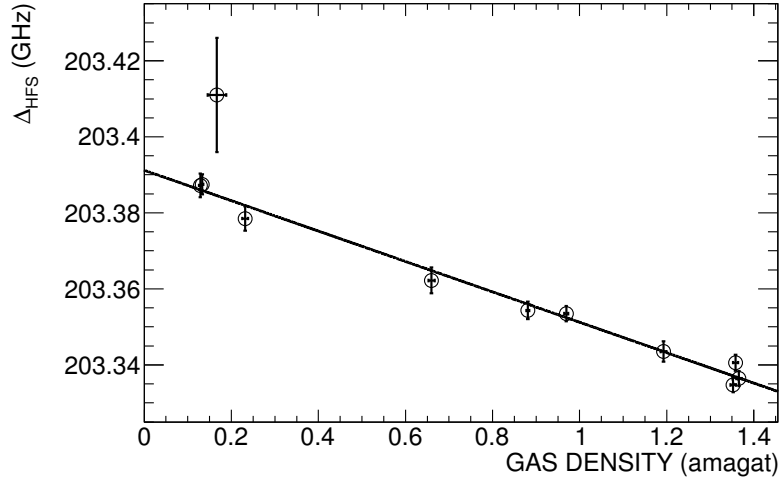


Figure 5.19:  $\Delta_{\text{HFS}}$  at each gas density. The circles with error bars are the data, and the solid line is the best-fit with a linear function. (Reproduced from Ref. [1])

Figure 5.20 is a summary plot of  $\Delta_{\text{HFS}}$  measurements. Our new result favors the QED calculation within 1.2 s.d., although it disfavors the previous experimental average by 2.6 s.d.

## 5.4 Non-thermalized Ps effect

In order to evaluate the non-thermalized Ps effect, which was not considered in previous experiments, fitting of the Zeeman transition lines without taking into account the time evolution of  $\Delta_{\text{HFS}}$  and  $\Gamma_{\text{pick}}$  is performed. The fitted Ps-HFS value with an assumption that Ps is well thermalized results in 203.3922(16) GHz ( $\chi^2/\text{ndf} = 721.1/592$ ,  $p = 2 \times 10^{-4}$ ). Comparing this with Eq. (5.6), the non-thermalized o-Ps effect is evaluated to be as large as  $10 \pm 2$  ppm in the used timing window. This effect might be larger if no timing window is applied, since it depends on the timing window used for the analysis. In the timing window of 0–50 ns, which is not used for the analysis, Ps-HFS is dramatically changing because the Ps is not well thermalized and the Ps velocity is still rapidly changing. It strongly suggests that the reason of the discrepancy in  $\Delta_{\text{HFS}}$  is the effect of non-thermalized Ps.

## 5.5 Future prospects

In our experiment, it is shown that the non-thermalized Ps effect is crucial for precise measurement of  $\Delta_{\text{HFS}}$ . To obtain further precision, it is necessary to reduce the systematic error associated with the material effect. Unfortunately, it is difficult to achieve with gas experiment because the lower the gas density, the lower the efficiencies of Ps formation and transition. Instead of using gas,

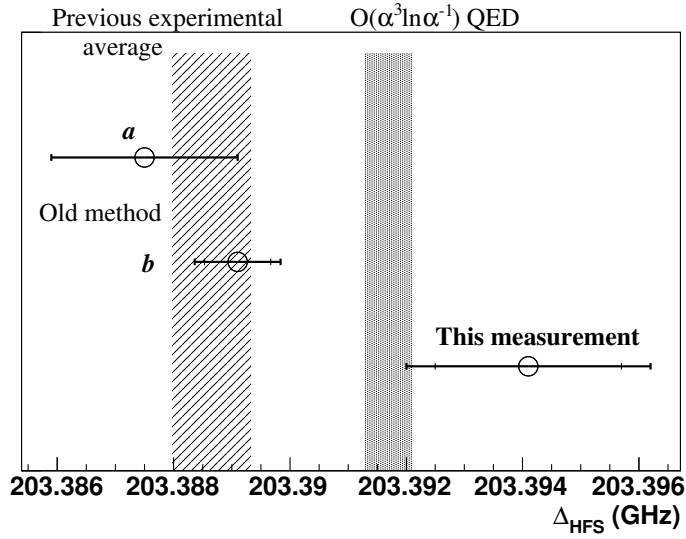


Figure 5.20: Summary of  $\Delta_{\text{HFS}}$  measurements from past experiments and this work. The circles with error bars are the experimental data ( $a$ –[43],  $b$ –[44]), the hatched band is the average of the previous experiments ( $a$  and  $b$ ), and the dotted band is the QED calculation [14, 34, 35]. (Reproduced from Ref. [1])

performing whole measurement in vacuum will be a quite efficient way. There are at least three benefits from vacuum experiment:

- High statistics can be easily obtained because measurement at only one density (vacuum) is enough.
- It is completely free from material effect, because ideally Ps does not collide with anything.
- Short measurement period gives us small systematic errors associated with instability of the system.

The key point in such an experiment is efficient Ps formation in vacuum with energy which enables easy treatment. Short (ns) pulsed slow positron beam is one of the most possible choice for positron source. Many efforts must be done for further precise measurement.

## Chapter 6

# Conclusion

A new precision measurement of Ps-HFS free from possible common uncertainties from Ps thermalization effect was performed to check the Ps-HFS discrepancy. The effect of non-thermalized o-Ps was evaluated to be as large as  $10 \pm 2$  ppm for the used timing window. This effect might be larger than 10 ppm if no timing window is applied, since it depends on the timing window. Including this effect, obtained new experimental value is  $\Delta_{\text{HFS}} = 203.3942 \pm 0.0016(\text{stat.}, 8.0 \text{ ppm}) \pm 0.0013(\text{sys.}, 6.4 \text{ ppm})$  GHz. It favors the  $O(\alpha^3 \ln \alpha^{-1})$  QED calculation within 1.2 s.d., although it disfavors the previous measurements by 2.6 s.d. Our new result shows that the material effect is crucial for the measurement.

# Appendix A

## Run Summary

This appendix describes summary of the runs.

### A.1 Temperature control

Temperature information is obtained using platinum resistance thermometer sensors (Pt100). Temperatures are measured by four-terminal method using the data logger (HIOKI 8420-50) at the precision of 0.01 K and recorded to the Linux PC.

The following temperatures are measured:

- Surface of the RF cavity at the center
- Positron source-end surface of the RF cavity
- Directional Coupler at the microwave waveguide
- Microwave feedthrough at the cavity
- NMR probe
- Air around the RF circuit
- Air around the DAQ electronics
- Intake air of the RF amplifier
- Exhaust air of the RF amplifier
- Air of the experimental hall of the Cryogenics Science Center at KEK
- Air in the bore of the superconducting magnet
- Inside wall of the superconducting magnet
- Flange of the superconducting magnet

The temperature information is used for correction of parameters of the RF system and the interlock system. Air temperature is carefully controlled by air conditioners, heat insulators, and the constant temperature water controlled by the chiller. The water temperature is controlled within  $\pm 0.1$  K (RMS is 0.02 K), and the air temperature is controlled within  $\pm 2$  K (RMS is 0.7 K). The air temperature around the RF circuit ( $T_{\text{RFcirc}}$ ) is used for correcting RF power measurements as follows: (1) RF amplifier output power measured by a power meter is corrected by  $+1.0 \times 10^{-3} \times (T_{\text{RFcirc}} - 20^\circ\text{C})$  dBm. (2) RF cavity-transmitted power measured by another power meter is corrected by  $+2.5 \times 10^{-3} \times (T_{\text{RFcirc}} - 20^\circ\text{C})$  dBm.

## A.2 Run table

All runs only used in analysis are summarized in Table A.1. If there were accidental power cuts or earthquakes during runs, pairs of event-taking and pedestal-taking data (about 30 minutes per each pair) which contained them were removed from analysis. RF-unstable data, *i.e.* in which sudden jumps of parameters occurred, were also removed. When there was a sudden jump in RF parameters, data only before or after the jump were used. There existed magnetic-field-scan data at 0.1323 amagat and 0.1361 amagat, but they were also removed because of their overall bad data quality.

Table A.1: Run table.

Magnetic field (T)	RF state (ON/OFF)	RUN start date (yyyy/mm/dd)	RUN finish date (yyyy/mm/dd)
<b>SCAN I: 0.880 9 amagat, 423.68 W, 2.852 445 1 GHz, <math>Q_L = 10302.7</math></b>			
0.865 733 64	OFF	2010/07/02	2010/07/05
	ON	2010/07/02	2010/07/02
0.867 265 02	ON	2010/07/05	2010/07/07
	OFF	2010/07/07	2010/07/15
0.863 900 5	ON	2010/07/15	2010/07/16
	OFF	2010/07/16	2010/07/20
0.869 994 2	ON	2010/07/20	2010/07/21
	OFF	2010/07/21	2010/07/22
0.861 243 5	ON	2010/07/22	2010/07/23
	OFF	2010/07/23	2010/07/25
0.864 752 7	OFF	2010/07/26	2010/07/27
	ON	2010/07/27	2010/07/29
0.866 485 84	ON	2010/07/29	2010/07/30
	OFF	2010/07/30	2010/08/02
<b>SCAN II: 0.659 7 amagat, 445.52 W, 2.853 538 5 GHz, <math>Q_L = 10993.3</math></b>			
0.865 662 42	ON	2010/08/02	2010/08/04
	OFF	2010/08/04	2010/08/05
0.867 394 57	ON	2010/08/05	2010/08/06
	OFF	2010/08/06	2010/08/09
0.863 959 22	OFF	2010/08/09	2010/08/11
	ON	2010/08/09	2010/08/11
0.870 053 48	OFF	2010/08/23	2010/08/24

Table A.1: Run table.

Magnetic field (T)	RF state (ON/OFF)	RUN start date (yyyy/mm/dd)	RUN finish date (yyyy/mm/dd)
	ON	2010/08/24	2010/08/26
0.861 219 99	ON	2010/08/26	2010/08/27
	OFF	2010/08/27	2010/08/30
0.864 751 07	OFF	2010/08/30	2010/08/30
	ON	2010/08/30	2010/08/31
<b>SCAN III: 0.231 7 amagat, 438.60 W, 2.861 905 0 GHz, <math>Q_L = 13667.2</math></b>			
0.866 465 30	ON	2010/10/04	2010/10/08
	OFF	2010/10/08	2010/10/12
0.863 882 99	ON	2010/10/12	2010/10/15
	OFF	2010/10/15	2010/10/18
0.867 319 00	ON	2010/10/19	2010/10/22
	OFF	2010/10/22	2010/10/23
0.861 153 64	ON	2010/10/25	2010/10/29
	OFF	2010/10/29	2010/11/01
0.869 899 85	ON	2010/11/01	2010/11/05
	OFF	2010/11/02	2010/11/08
0.864 693 10	ON	2010/11/08	2010/11/12
	OFF	2010/11/12	2010/11/15
0.864 693 97	ON	2010/11/15	2010/11/19
	OFF	2010/11/19	2010/11/22
0.865 705 1	ON	2010/11/24	2010/11/26
	OFF	2010/11/26	2010/11/29
<b>SCAN IV: 0.167 amagat, 220.36 W, 2.862 400 4 GHz, <math>Q_L = 14096.5</math></b>			
0.870 010 3	ON	2011/01/18	2011/01/21
	OFF	2011/01/21	2011/01/24
0.861 255 81	ON	2011/01/24	2011/01/28
	OFF	2011/01/28	2011/01/31
0.868 159 75	ON	2011/01/31	2011/02/04
	OFF	2011/02/04	2011/02/07
0.870 912 22	ON	2011/02/07	2011/02/10
	OFF	2011/02/10	2011/02/14
<b>SCAN V: 1.358 1 amagat, 469.48 W, 2.857 588 5 GHz, <math>Q_L = 11060.0</math></b>			
0.867 884 00	ON	2011/07/05	2011/07/07
	OFF	2011/07/07	2011/07/11
0.864 046 11	OFF	2011/07/11	2011/07/12
	ON	2011/07/12	2011/07/14
0.867 296 47	ON	2011/07/14	2011/07/15
	OFF	2011/07/15	2011/07/17
0.864 916 02	ON	2011/07/19	2011/07/20
	OFF	2011/07/22	2011/07/25
0.866 313 94	ON	2011/07/25	2011/07/27
	OFF	2011/07/27	2011/07/28
0.866 314 37	ON	2011/07/28	2011/07/29
	OFF	2011/07/29	2011/08/03
<b>SCAN VI: 0.969 2 amagat, 485.25 W, 2.859 258 4 GHz, <math>Q_L = 12268.4</math></b>			

Table A.1: Run table.

Magnetic field (T)	RF state (ON/OFF)	RUN start date (yyyy/mm/dd)	RUN finish date (yyyy/mm/dd)
0.865 485 28	ON	2011/11/07	2011/11/09
	OFF	2011/11/09	2011/11/10
0.868 125 57	ON	2011/11/10	2011/11/11
	OFF	2011/11/11	2011/11/14
0.864 828 73	ON	2011/11/14	2011/11/16
	OFF	2011/11/16	2011/11/17
0.867 784 54	ON	2011/11/17	2011/11/18
	OFF	2011/11/18	2011/11/21
0.866 458 68	ON	2011/11/21	2011/11/22
	OFF	2011/11/22	2011/12/05
<b>SCAN VII: 1.352 5 amagat, 493.65 W, 2.857 666 6 GHz, <math>Q_L = 11368.4</math></b>			
0.866 460 79	ON	2011/12/20	2011/12/21
	OFF	2011/12/22	2012/01/10
0.865 359 53	ON	2012/01/10	2012/01/11
	OFF	2012/01/13	2012/01/16
0.867 101 34	ON	2012/01/16	2012/01/18
	OFF	2012/01/20	2012/01/23
0.864 485 19	ON	2012/01/23	2012/01/25
	OFF	2012/01/27	2012/01/30
0.867 890 8	ON	2012/01/30	2012/02/01
	OFF	2012/02/03	2012/02/06
<b>SCAN VIII: 1.365 8 amagat, 319.51 W, 2.857 677 6 GHz, <math>Q_L = 11368.5</math></b>			
0.866 460 24	ON	2011/12/21	2011/12/22
	OFF	2011/12/22	2012/01/10
0.865 360 52	ON	2012/01/11	2012/01/13
	OFF	2012/01/13	2012/01/16
0.867 101 71	ON	2012/01/18	2012/01/20
	OFF	2012/01/20	2012/01/23
0.864 485 48	ON	2012/01/25	2012/01/27
	OFF	2012/01/27	2012/01/30
0.867 890 24	ON	2012/02/01	2012/02/03
	OFF	2012/02/03	2012/02/06
<b>SCAN IX: 1.192 5 amagat, 466.39 W, 2.858 301 9 GHz, <math>Q_L = 11582.9</math></b>			
0.864 573 50	ON	2012/02/15	2012/02/17
	OFF	2012/02/17	2012/02/23
0.867 085 29	ON	2012/02/23	2012/02/24
	OFF	2012/02/24	2012/02/27
0.865 440 03	ON	2012/02/27	2012/02/28
	OFF	2012/02/28	2012/02/29
0.866 281 08	ON	2012/02/29	2012/03/02
	OFF	2012/03/02	2012/03/05
<b>SCAN X: 0.128 7 amagat, 117.91 W, 2.862 585 0 GHz, <math>Q_L = 15355.2</math></b>			
0.867 481 3	ON	2012/05/15	2012/05/18
	OFF	2012/05/18	2012/05/21
0.868 909 4	ON	2012/05/21	2012/05/25

Table A.1: Run table.

Magnetic field (T)	RF state (ON/OFF)	RUN start date (yyyy/mm/dd)	RUN finish date (yyyy/mm/dd)
	OFF	2012/05/25	2012/05/28
0.865 497 14	ON	2012/05/28	2012/06/01
	OFF	2012/06/01	2012/06/04
0.868 112 72	ON	2012/06/04	2012/06/08
	OFF	2012/06/08	2012/06/11
0.865 944 34	ON	2012/06/11	2012/06/15
	OFF	2012/06/15	2012/06/18
<b>SCAN XI: 0.133 3 amagat, 126.48 W, 2.862 513 8 GHz, <math>Q_L = 15310.3</math></b>			
0.865 942 42	ON	2012/06/18	2012/06/22
	OFF	2012/06/22	2012/06/25
0.868 043 11	ON	2012/06/25	2012/06/29
	OFF	2012/06/29	2012/07/02
0.865 385 04	ON	2012/07/02	2012/07/05
	OFF	2012/07/06	2012/07/09
0.868 876 92	ON	2012/07/09	2012/07/13
	OFF	2012/07/13	2012/07/17
0.867 215 37	ON	2012/07/17	2012/07/20
	OFF	2012/07/20	2012/07/23
0.866 294 41	ON	2012/07/23	2012/07/27
	OFF	2012/07/27	2012/07/30
0.868 436 81	ON	2012/07/30	2012/08/03
	OFF	2012/08/03	2012/08/06

## Appendix B

# Ps Thermalization Measurement

In this appendix, an experimental apparatus and results of our Ps thermalization measurement using ‘pick-off technique’ are described. They are only roughly explained here because this measurement is quite similar to the older ‘pick-off technique’ thermalization measurements used in o-Ps lifetime measurement [80, 81, 82].

### B.1 Experimental setup

#### B.1.1 Overview of the apparatus

Figures B.1 and B.2 show the overview of the experimental setup. The gas chamber which is similar to the cavity used in Ps-HFS measurement was used. The chamber was filled with the same  $i\text{-C}_4\text{H}_{10}$  gas as the Ps-HFS measurement, and Ps were formed inside the chamber. Two separate measurement with and without aerogel were performed. With aerogel setup, most of positrons emitted to aerogel were stopped so that Ps were formed very efficiently. Without aerogel, only some fraction of positrons could be stopped with gas so that the Ps formation efficiency was worse than with-aerogel setup. Without-aerogel setup was used to understand whether or not aerogel did affect the result of thermalization parameters of  $i\text{-C}_4\text{H}_{10}$ . A  $\beta$ -tagging system similar to that used in Ps-HFS measurement was used to measure timing information. For  $\gamma$ -ray detection, a Ge detector (ORTEC PopTop GEM40P-PLUS-S, Serial No.=45-TP22020A) was used.

#### B.1.2 Electronics circuit

Electronics circuit used for data acquisition (DAQ) is shown in Figs. B.3–B.10. Detail explanation is not given here because it is essentially the same as the setup of the previous o-Ps lifetime measurement [82].

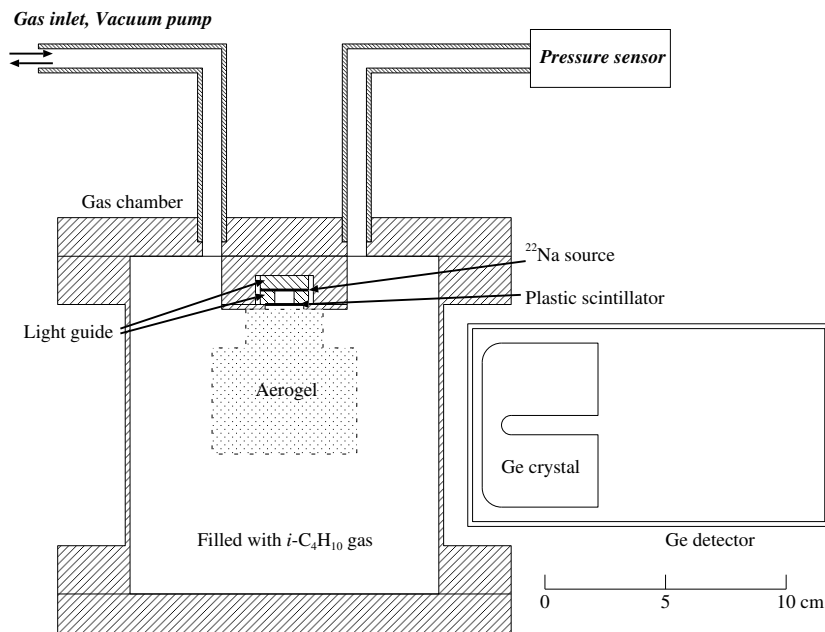


Figure B.1: Side view of the setup of  $\text{Ps}$  thermalization measurement.

### B.1.3 Monte Carlo simulation

Monte Carlo simulations were used to estimate the energy spectra of  $3\gamma$  decay of  $\text{Ps}$ . The same Geant4 package as used in  $\text{Ps}$ -HFS measurement was used. Most of the experimental setup (materials and geometry) are carefully input. Figures B.11 and B.12 show the geometry input in the simulation.

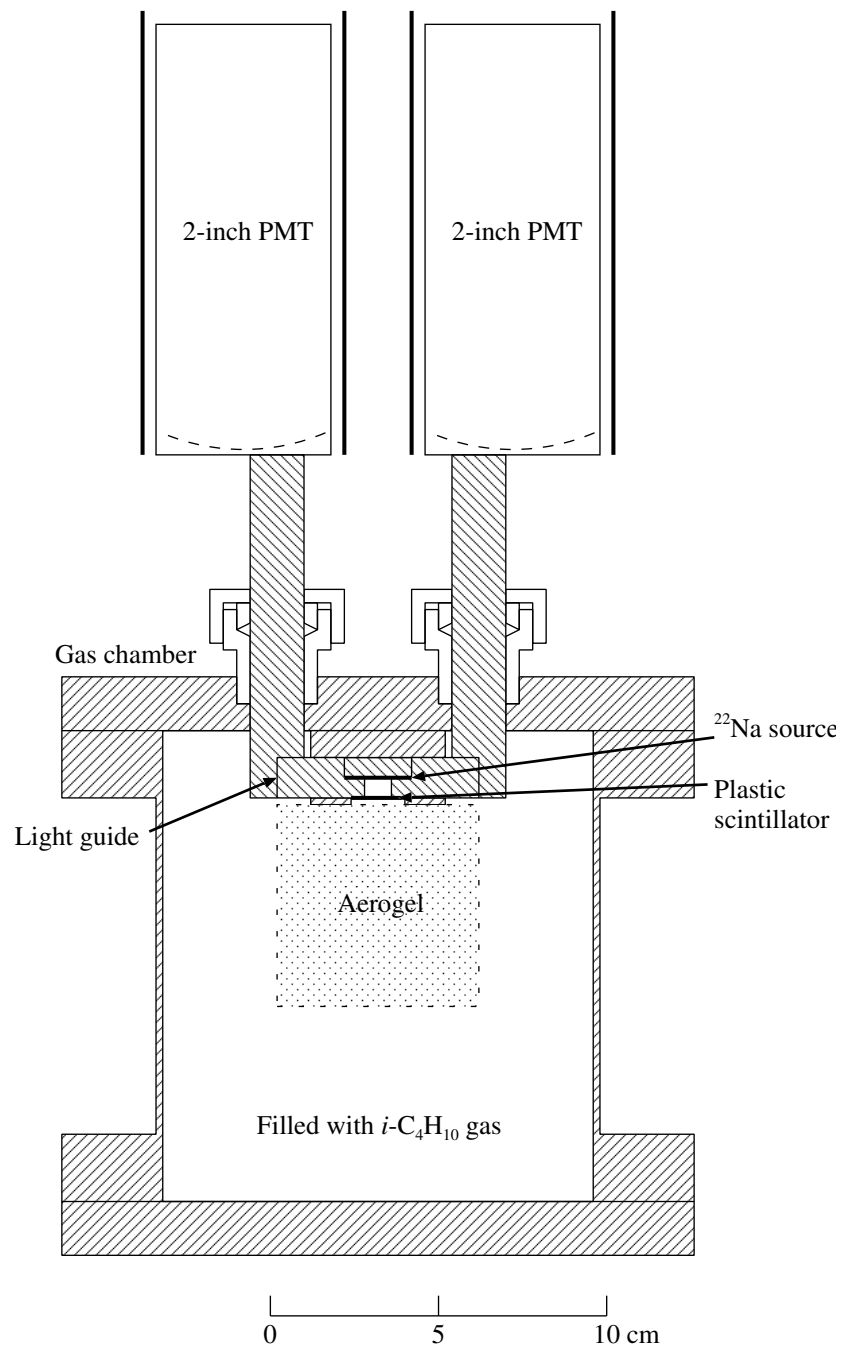


Figure B.2: Front view of the setup of Ps thermalization measurement.

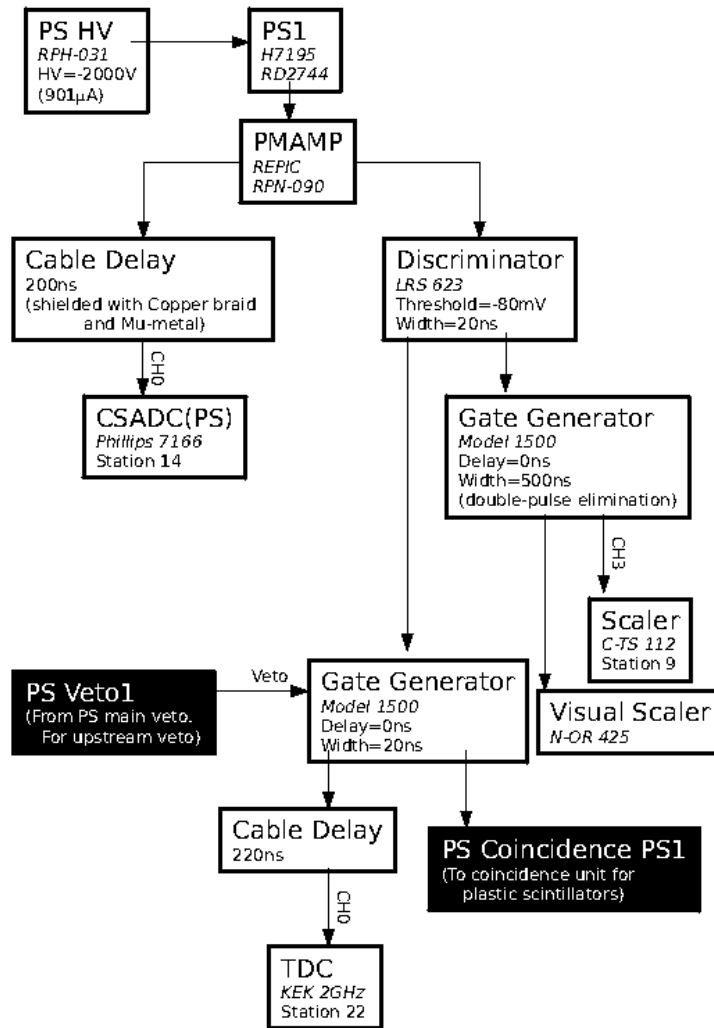
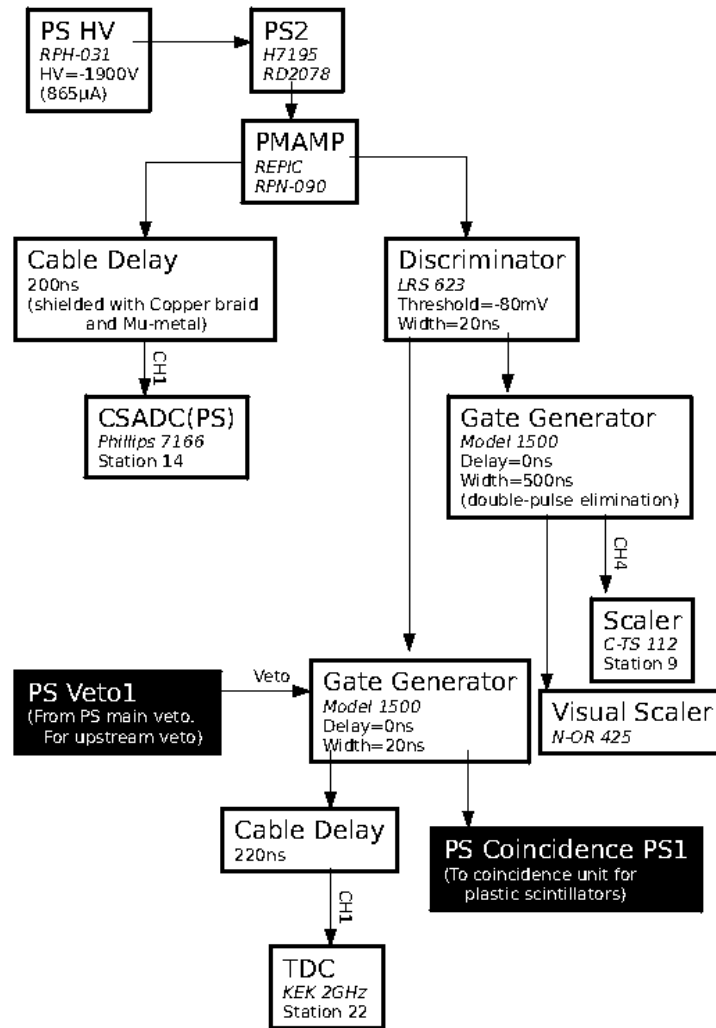


Figure B.3: DAQ of Ps thermalization (Plastic scintillator 1).

Figure B.4: DAQ of  $P_s$  thermalization (Plastic scintillator 2).

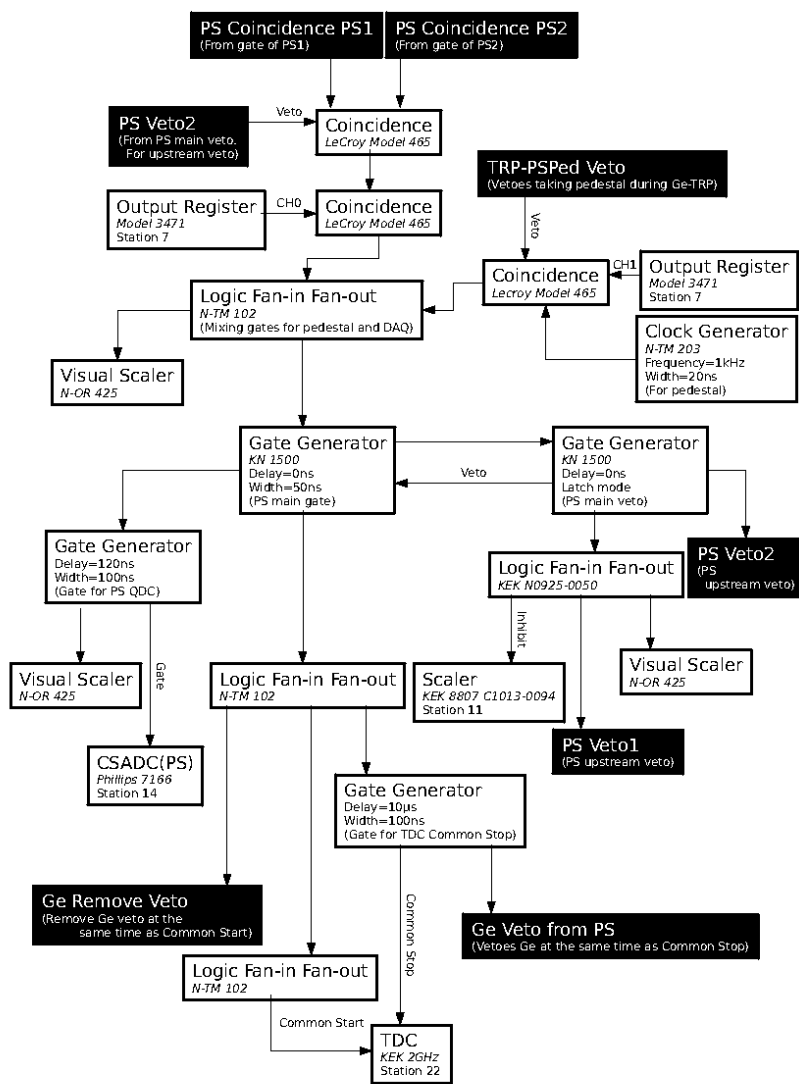
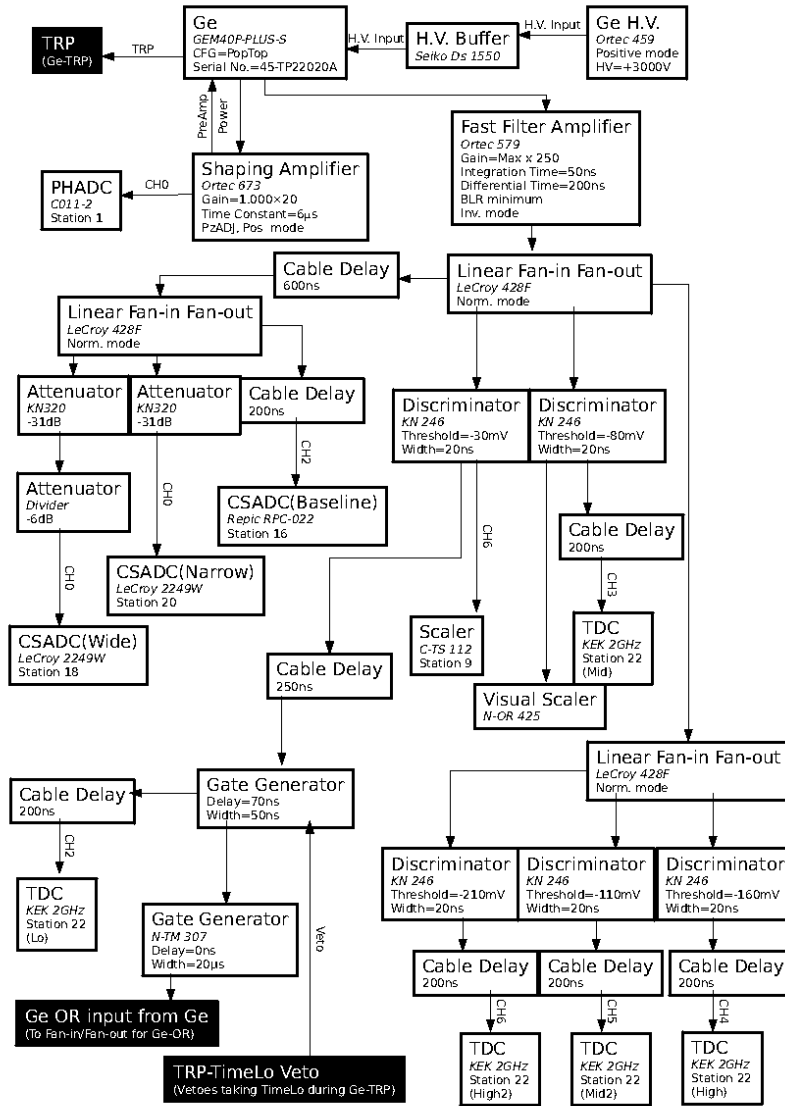


Figure B.5: DAQ of Ps thermalization (Trigger).

Figure B.6: DAQ of P<sub>s</sub> thermalization (Ge detector).

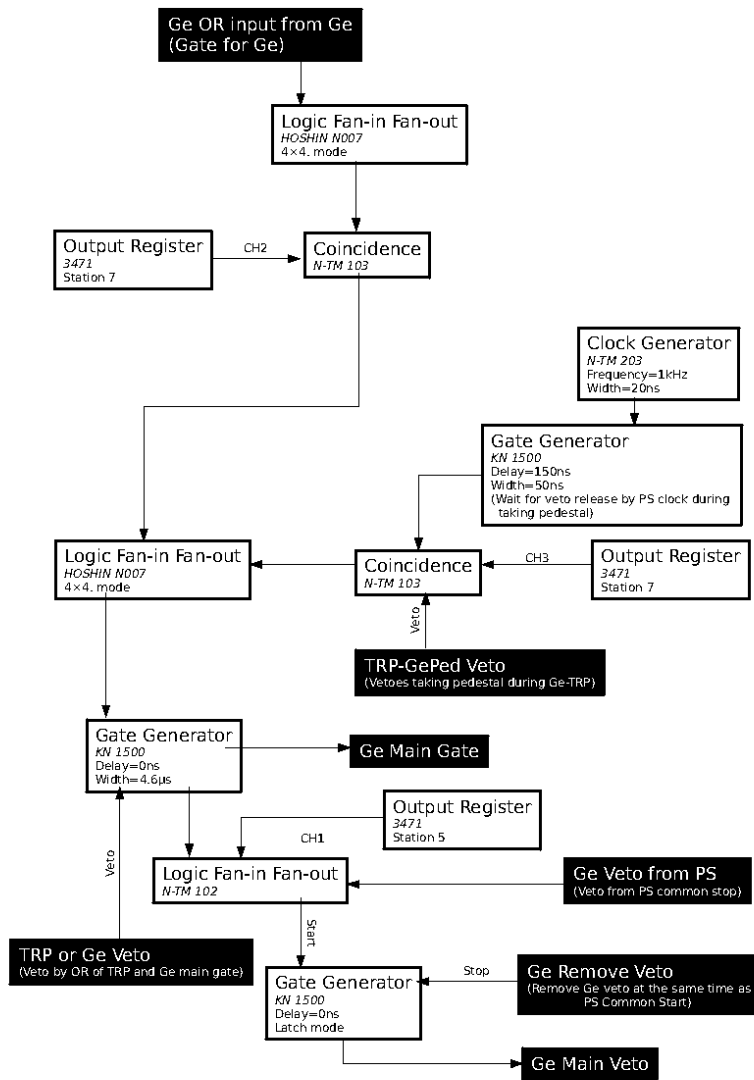


Figure B.7: DAQ of Ps thermalization (Ge Main Gate).

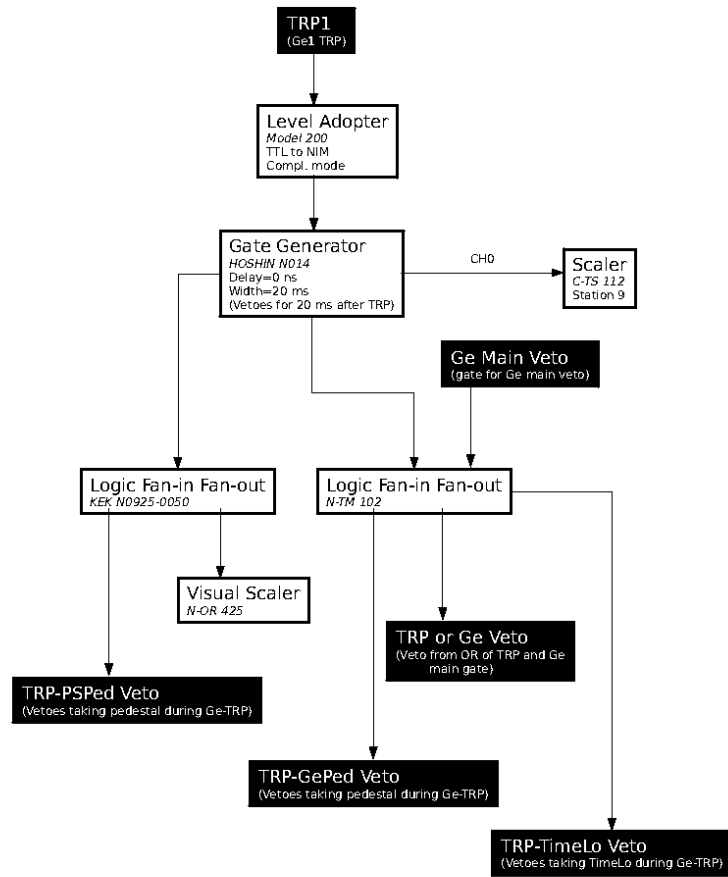
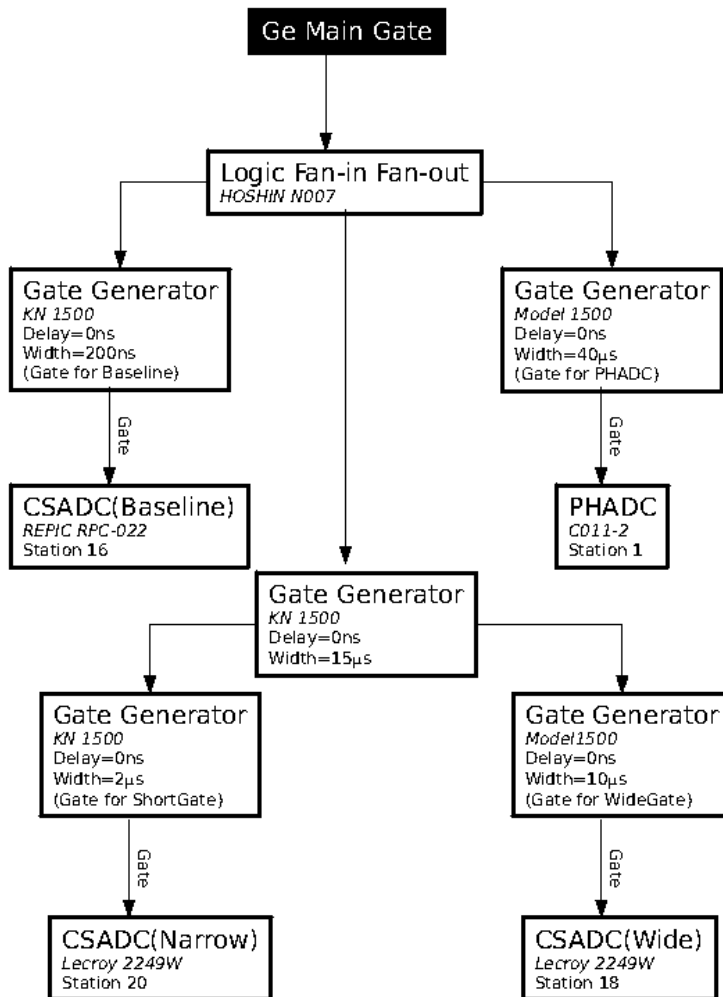
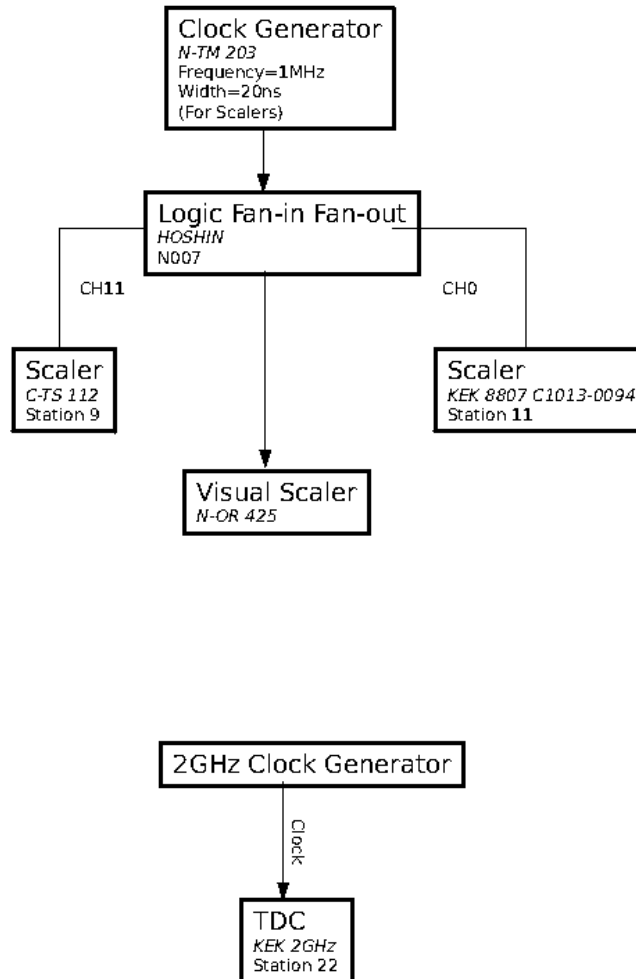


Figure B.8: DAQ of Ps thermalization (Ge Transistor-Reset-Pulse (TRP) veto).

Figure B.9: DAQ of P<sub>s</sub> thermalization (Ge ADCs' gates).

Figure B.10: DAQ of P<sub>s</sub> thermalization (Clock system).

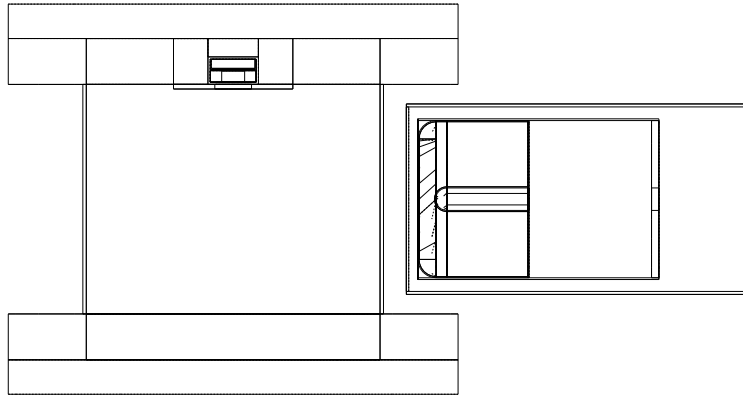


Figure B.11: Side view of the geometry in the MC simulation (thermalization measurement)

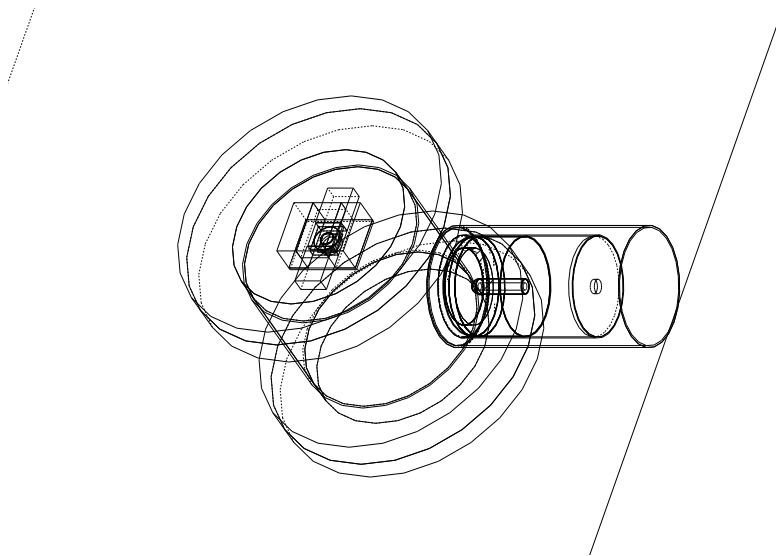


Figure B.12: Bird's-eye view of the geometry in the MC simulation (thermalization measurement)

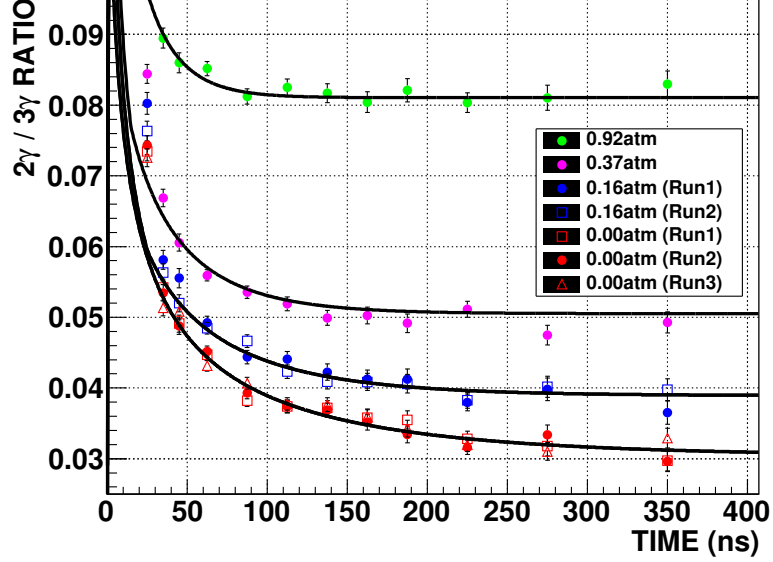


Figure B.13: Pick-off ratio as a function of time (with aerogel). The dots with error bars are the data, and the solid lines indicate the best-fit function.

## B.2 Results

Proceeding an analysis similar to that of Ref. [82],

$\Gamma_{\text{pick}}(t)/\Gamma_{\text{o-Ps}} = (2\gamma \text{ annihilation rate})/(3\gamma \text{ annihilation rate})$  as a function of time is obtained using  $\gamma$ -ray energy spectra. Figures B.13 and B.14 show the pick-off ratio of with- and without-aerogel measurement, respectively, as a function of time. The data are fitted by the following function:

$$\frac{\Gamma_{\text{pick}}(t)}{\Gamma_{\text{o-Ps}}} = (C_{\text{aero}} + C_{\text{iso}}n) [v(t)]^{0.6}, \quad (\text{B.1})$$

where  $C_{\text{aero}}$  is a constant associated with the pick-off annihilation with aerogel,  $C_{\text{iso}}$  is a constant associated with the pick-off annihilation with  $i\text{-C}_4\text{H}_{10}$  gas, and  $n$  is the gas density.  $v(t)$  is determined using the following differential equation similar to Eq. (2.1):

$$\frac{dE_{\text{av}}(t)}{dt} = -\sqrt{2m_{\text{Ps}}E_{\text{av}}(t)} \left( E_{\text{av}}(t) - \frac{3}{2}k_{\text{B}}T \right) \left[ \frac{8}{3} \sqrt{\frac{2}{3\pi}} \frac{2\sigma_{\text{m}}n}{M} + \alpha \left( \frac{E_{\text{av}}(t)}{k_{\text{B}}T} \right)^{\beta} \right], \quad (\text{B.2})$$

where  $\alpha$  and  $\beta$  are constants associated with Ps thermalization in aerogel.  $C_{\text{aero}}$  and  $\alpha$  are zero if there is no aerogel. In our analysis, the thermalization parameters from DBS measurement ( $E_0 = 3.1^{+1.0}_{-0.7}$  eV,  $\sigma_{\text{m}} = 146 \pm 11 \text{ \AA}^2$ ) are used from  $t = 0$  to the time at which the kinetic energy of o-Ps reaches 0.17 eV, and then the  $\sigma_{\text{m}}$  is changed to free parameter.

The data are well-fitted by Eq. (B.1).  $\sigma_{\text{m}} = 46.0 \pm 4.5 \text{ \AA}^2$  for with-aerogel measurement and  $\sigma_{\text{m}} = 50.7^{+8.8}_{-7.9} \text{ \AA}^2$  for without-aerogel measurement are ob-

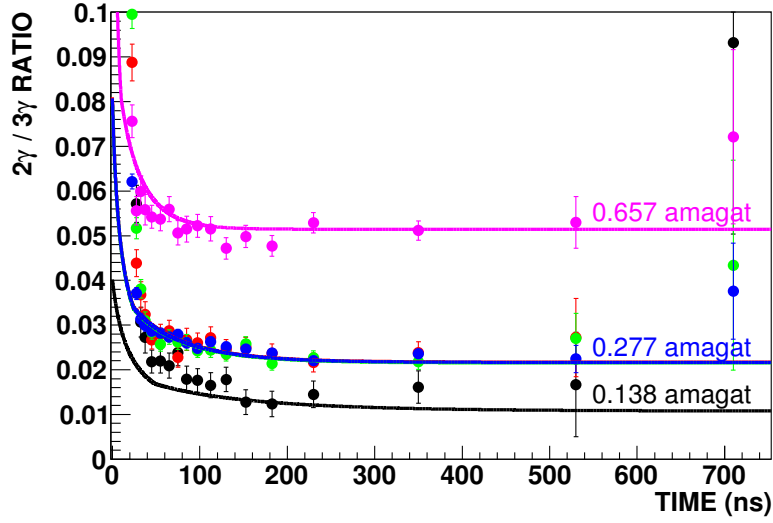


Figure B.14: Pick-off ratio as a function of time (without aerogel). The dots with error bars are the data, and the solid lines indicate the best-fit function.

tained. These results are consistent with each other, and the combined result of  $\sigma_m = 47.2 \pm 3.9 \text{ \AA}^2$  is obtained for o-Ps below 0.17 eV.

In Eq. (B.1), it is assumed that the pick-off annihilation rate with aerogel is also proportional to  $[v(t)]^{0.6}$ . However, there is no evidence for this assumption. To estimate a systematic error of this assumption, a fitting in which the pick-off annihilation rate with aerogel is assumed to be proportional to  $v(t)$  was performed. The result was changed by  $+5.4 \text{ \AA}^2$ , which is considered as a systematic error. The final result of the P<sub>s</sub> thermalization measurement is obtained as

$$\sigma_m = 47.2 \pm 6.7 \text{ \AA}^2, \quad (\text{B.3})$$

which is used in the analysis of the  $\Delta_{\text{HFS}}$  measurement.

## Appendix C

# Final Fitting Parameters

In this appendix, the final fitting parameters of Eq. 5.1 and associated equations:  $D_1(n)$ ,  $D_2(n)$ ,  $\epsilon(n)$ , and  $B_{\text{RF}}$  are shown as a function of gas density in Figs. C.1, C.2, C.3, and C.4, respectively.

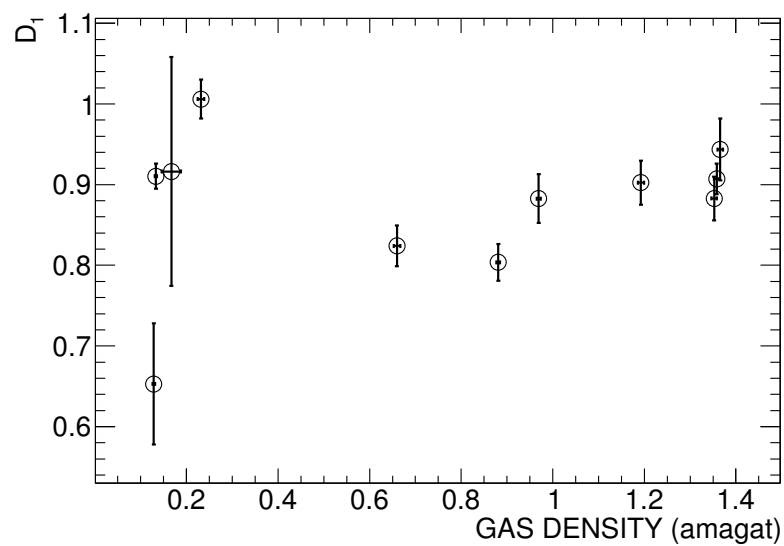
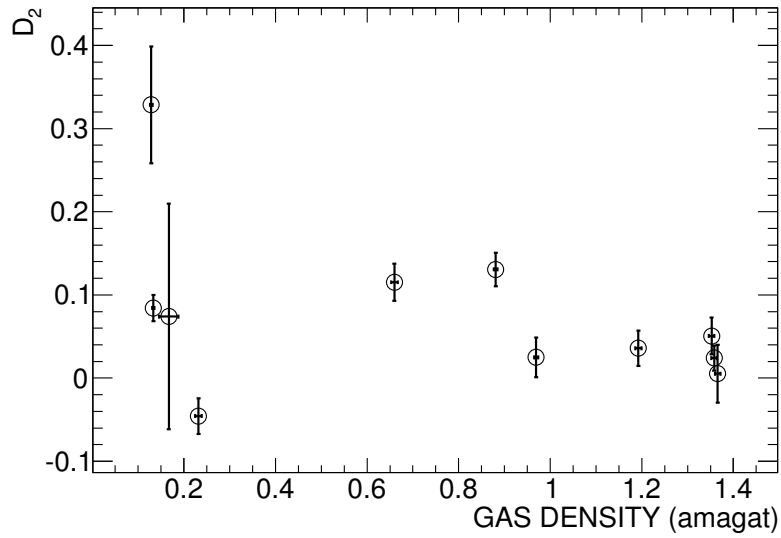
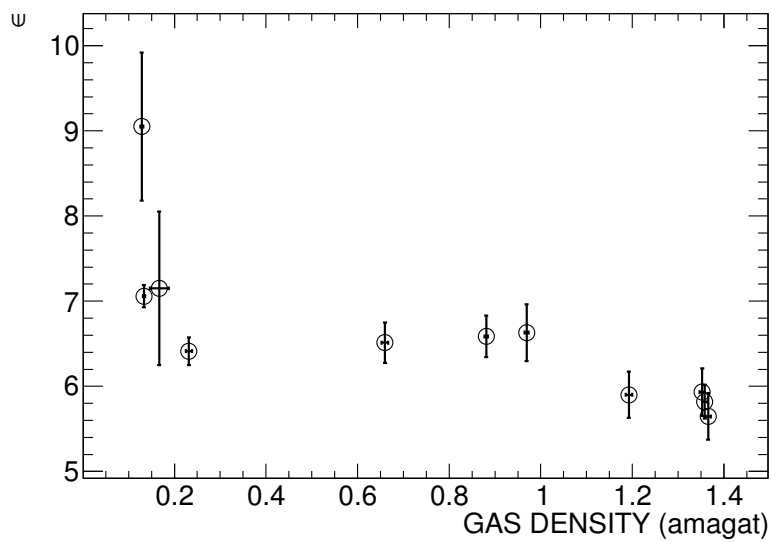
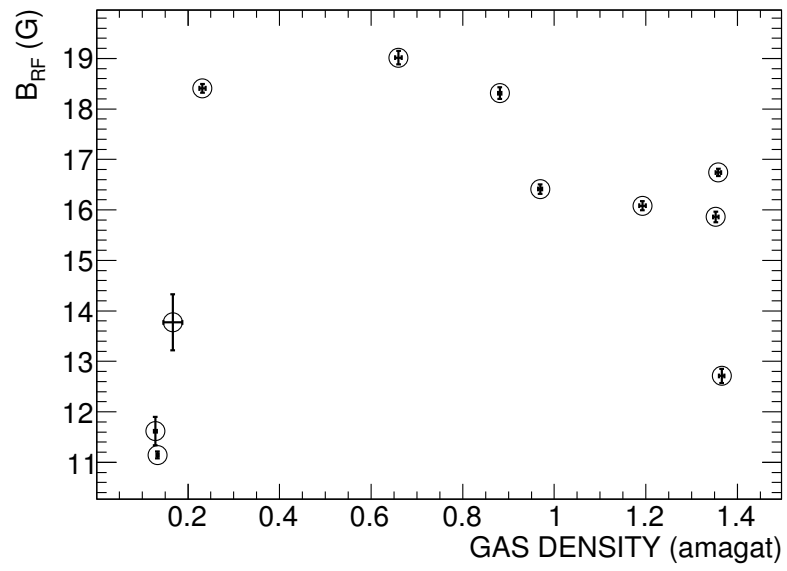


Figure C.1:  $D_1(n)$

Figure C.2:  $D_2(n)$ Figure C.3:  $\epsilon(n)$

Figure C.4:  $B_{RF}(n)$

# References

- [1] A. Ishida et al., Phys. Lett. B **734**, 338 (2014).
- [2] A. H. Al-Ramadhan and D. W. Gidley, Phys. Rev. Lett. **72**, 1632 (1994).
- [3] Y. Kataoka, S. Asai, and T. Kobayashi, Phys. Lett. B **671**, 219 (2009).
- [4] S. Adachi et al., Phys. Rev. Lett. **65**, 2634 (1990).
- [5] H. von Busch et al., Phys. Lett. B **325**, 300 (1994).
- [6] S. Adachi et al., Phys. Rev. A **49**, 3201 (1994).
- [7] J. Yang et al., Phys. Rev. A **54**, 1952 (1996).
- [8] P. A. Vetter and S. J. Freedman, Phys. Rev. A **66**, 052505 (2002).
- [9] T. Matsumoto et al., Phys. Rev. A **54**, 1947 (1996), Erratum A **56** and 1060 (1997).
- [10] G. Atoyán, S. Gninenko, V. Razin, and Y. Ryabov, Phys. Lett. B **220**, 317 (1989).
- [11] T. Mitsui et al., Phys. Rev. Lett. **70**, 2265 (1993).
- [12] A. Badertscher et al., Phys. Rev. D **75**, 032004 (2007).
- [13] S. G. Karshenboim, Phys. Rep. **422**, 1 (2005).
- [14] B. A. Kniehl and A. A. Penin, Phys. Rev. Lett. **85**, 5094 (2000).
- [15] J. Pirenne, Arch. Sci. Phys. Nat. **29**, 265 (1947).
- [16] V. B. Berestetski and L. D. Landau, Zh. Eksp. Teor. Fiz. **19**, 673 (1949).
- [17] R. A. Ferrell, Phys. Rev. **84**, 858 (1951).
- [18] R. Karplus and A. Klein, Phys. Rev. **87**, 848 (1952).
- [19] G. T. Bodwin and D. R. Yennie, Phys. Rep. **43**, 267 (1978).
- [20] W. E. Caswell and G. P. Lepage, Phys. Rev. A **20**, 36 (1979).
- [21] S. J. Brodsky and G. W. Erickson, Phys. Rev. **148**, 26 (1966).
- [22] R. Barbieri, J. A. Mignaco, and E. Remiddi, Nuovo Cimento Soc. Ital. Fis. **11A**, 824 (1972).

- 
- [23] G. S. Adkins, M. H. T. Bui, and D. Zhu, *Phys. Rev. A* **37**, 4071 (1988).
- [24] G. S. Adkins, Y. M. Aksu, and M. H. T. Bui, *Phys. Rev. A* **47**, 2640 (1993).
- [25] G. S. Adkins, R. N. Fell, and P. M. Mitrikov, *Phys. Rev. Lett.* **79**, 3383 (1997).
- [26] A. H. Hoang, P. Labelle, and S. M. Zebarjad, *Phys. Rev. Lett.* **79**, 3387 (1997).
- [27] J. R. Sapirstein, E. A. Terray, and D. R. Yennie, *Phys. Rev. D* **29**, 2290 (1984).
- [28] K. Pachucki and S. G. Karshenboim, *Phys. Rev. Lett.* **80**, 2101 (1998).
- [29] K. Pachucki, *Phys. Rev. A* **56**, 297 (1997).
- [30] G. S. Adkins and J. Sapirstein, *Phys. Rev. A* **58**, 3552 (1998), **61** and 069902(E) (2000).
- [31] A. P. Burichenko, hep-ph/0004063 (2000).
- [32] A. Czarnecki, K. Melnikov, and A. Yelkhovsky, *Phys. Rev. Lett.* **82**, 311 (1999), *Phys. Rev. A* **59**, 4316 (1999).
- [33] S. G. Karshenboim, *Zh. Eksp. Teor. Fiz.* **103**, 1105 (1993), [*Sov. Phys. JETP* **76**, 541 (1993)].
- [34] K. Melnikov and A. Yelkhovsky, *Phys. Rev. Lett.* **86**, 1498 (2001).
- [35] R. J. Hill, *Phys. Rev. Lett.* **86**, 3280 (2001).
- [36] M. Baker, P. Marquard, A. A. Penin, J. Piclum, and M. Steinhauser, *Phys. Rev. Lett.* **112**, 120407 (2014).
- [37] G. S. Adkins and R. N. Fell, *Phys. Rev. A* **89**, 052518 (2014).
- [38] M. Deutsch and S. C. Brown, *Phys. Rev.* **85**, 1047 (1952).
- [39] H. Grotch and R. A. Hegstorm, *Phys. Rev. A* **4**, 59 (1971).
- [40] E. R. Carlson, V. W. Hughes, M. L. Lewis, and I. Lindgren, *Phys. Rev. Lett.* **29**, 1059 (1972).
- [41] H. Grotch and R. Kashuba, *Phys. Rev. A* **7**, 78 (1973).
- [42] M. L. Lewis and V. W. Hughes, *Phys. Rev. A* **8**, 625 (1973).
- [43] A. P. Mills, Jr., *Phys. Rev. A* **27**, 262 (1983).
- [44] M. W. Ritter, P. O. Egan, V. W. Hughes, and K. A. Woodle, *Phys. Rev. A* **30**, 1331 (1984).
- [45] V. G. Baryshevsky, O. N. Metelitsa, and V. V. Tikhomirov, *J. Phys. B* **22**, 2835 (1989).
- [46] W. Bernreuther and O. Nachtmann, *Z. Phys. C* **11**, 235 (1981).

- 
- [47] R. Weinstein, M. Deutsch, and S. Brown, Phys. Rev. **94**, 758 (1954), **98** and 223 (1955).
- [48] V. W. Hughes, S. Marder, and C. S. Wu, Phys. Rev. **106**, 934 (1957).
- [49] E. D. Theriot, Jr., R. H. Beers, V. W. Hughes, and K. O. H. Ziock, Phys. Rev. A **2**, 707 (1970).
- [50] E. R. Carlson, V. W. Hughes, M. L. Lewis, and I. Lindgren, Phys. Rev. Lett. **29**, 1059 (1972).
- [51] A. P. Mills, Jr. and G. H. Bearman, Phys. Rev. Lett. **34**, 246 (1975).
- [52] E. R. Carlson, V. W. Hughes, and I. Lindgren, Phys. Rev. A **15**, 241 (1977).
- [53] P. O. Egan, V. W. Hughes, and M. H. Yam, Phys. Rev. A **15**, 251 (1977).
- [54] N. Allard and J. Kielkopf, Rev. Mod. Phys. **54**, 1103 (1982).
- [55] S. Asai, S. Orito, and N. Shinohara, Phys. Lett. B **357**, 475 (1995).
- [56] O. Jinnouchi, S. Asai, and T. Kobayashi, Phys. Lett. B **572**, 117 (2003).
- [57] R. S. Vallery, P. W. Zitzewitz, and D. W. Gidley, Phys. Rev. Lett. **90**, 203402 (2003).
- [58] Y. Nagashima, M. Kakimoto, T. Hyodo, and K. Fujiwara, Phys. Rev. A **52**, 258 (1995).
- [59] F. Saito, Y. Nagashima, and T. Hyodo, J. Phys. B **36**, 4191 (2003).
- [60] M. Skalsey, J. J. Engbrecht, C. M. Nakamura, R. S. Vallery, and D. W. Gidley, Phys. Rev. A **67**, 022504 (2003).
- [61] M. Skalsey, J. J. Engbrecht, R. K. Bithell, R. S. Vallery, and D. W. Gidley, Phys. Rev. Lett. **80**, 3727 (1998).
- [62] R. B. Firestone, Nucl. Data Sheets **106**, 1 (2005), Data extracted from the ENSDF database, version Dec. 11, 2009, from the NNDC WorldWideWeb site.
- [63] K. Iwata, R. G. Greaves, T. J. Murphy, M. D. Tinkle, and C. M. Surko, Phys. Rev. A **51**, 473 (1995).
- [64] D. A. L. Paul and L. Saint-Pierre, Phys. Rev. Lett. **11**, 493 (1963).
- [65] M. Charlton, Rep. Prog. Phys. **48**, 737 (1985).
- [66] SAINT-GOBAIN CRYSTALS, Scintillation Products Technical Note: BrillanCe<sup>TM</sup> Scintillators Performance Summary (Revision: January, 2009).
- [67] S. Agostinelli *et al.*, Nucl. Instrum. Methods Phys. Res. Sect. A **506**, 250 (2003).
- [68] J. Allison *et al.*, IEEE Trans. Nucl. Sci. **53**, 270 (2006).

- 
- [69] A. A. Sonzogni, Nucl. Data Sheets **98**, 515 (2003), Data extracted from the ENSDF database, version Dec. 11, 2009, from the NNDC WorldWideWeb site.
- [70] A. Öre and J. L. Powell, Phys. Rev. **75**, 1696 (1949).
- [71] W. E. Caswell, G. P. Lepage, and J. Sapirstein, Phys. Rev. Lett. **38**, 488 (1977).
- [72] G. S. Adkins, Ann. Phys. (NY) **146**, 78 (1983).
- [73] G. S. Adkins, Phys. Rev. Lett. **76**, 4903 (1996).
- [74] B. Brun and F. Rademakers, ROOT - An Object Oriented Data Analysis Framework, Proceedings AIHENP'96 Workshop, Lausanne, Sep. 1996, Nucl. Inst. & Meth. in Phys. Res. A **389**, 81 (1997), See also <http://root.cern.ch/>.
- [75] IT/ASD CERN, *MINUIT Function Minimization and Error Analysis, version 94.1* (1998), D506 CERN Program Library.
- [76] P. G. Coleman, T. C. Griffith, and G. R. Heyland, Appl. Phys. **5**, 223 (1974).
- [77] R. S. Vallery, A. E. Leanhardt, M. Skalsey, and D. W. Gidley, J. Phys. B **33**, 1047 (2000).
- [78] B. N. Miller, T. L. Reese, and G. A. Worrell, Can. J. Phys. **74**, 548 (1996).
- [79] C. D. Dermer and J. C. Weisheit, Phys. Rev. A **40**, 5526 (1989).
- [80] S. Asai, PhD thesis, The University of Tokyo, 1995.
- [81] O. Jinnouchi, PhD thesis, The University of Tokyo, 2001.
- [82] Y. Kataoka, PhD thesis, The University of Tokyo, 2007.